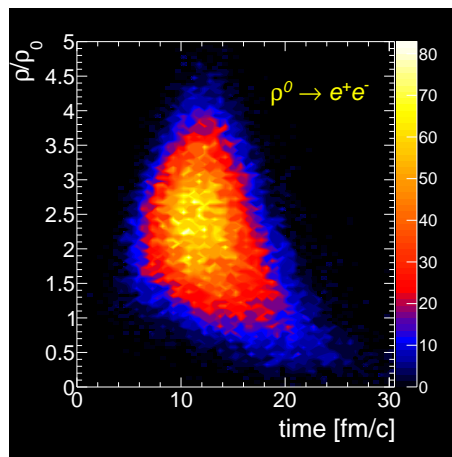


Goethe-Universität Frankfurt am Main
Institut für Kernphysik

Development of an event generator for dilepton production
in heavy ion collisions in the SIS energy regime

Masterthesis



Examiner: Prof. Dr. J. Stroth
Supervisor: Dr. T. Galatyuk

from
Claudia Behnke
Matrikelnr.: 3352098
Frankfurt am Main
September 28, 2011

Abstract

Photons (γ) and lepton pairs (e^+e^- , $\mu^+\mu^-$) emerging from the decay of virtual photons are the most promising probes of the dense hadronic matter. Direct photons and leptons contain information about the properties of dense matter in the initial moments of the collision.

An enhanced e^+e^- yield of lepton pairs above the trivial hadronic cocktail was measured with the DLS spectrometer. This enhancement could not be explained by transport calculations and is known as the "DLS puzzle".

After confirmation of the DLS data by the HADES collaboration, the experimental issues of the "DLS puzzle" were solved. Recent HADES results on e^+e^- production in $^{40}\text{Ar}+KCl$ collisions show at intermediate e^+e^- invariant masses ($0.15 < M_{e^+e^-} < 0.55 \text{ GeV}/c^2$) a strong enhancement of the dilepton yield over a reference spectrum reconstructed from elementary nucleon-nucleon reactions, suggesting the onset of non-trivial effects of the nuclear medium.

The main aim of this work is to develop an event generator which allow to separate in a transparent way the generation of the event background from the emission pattern of a physics observable under consideration. This approach will combine the advantages of the UrQMD microscopic transport model and a thermal model. The evolution of the has been investigated when moving to larger reaction systems and higher kinetic beam energies to be measured by HADES at SIS18 and SIS100.

Contents

I	Introduction and Motivation	1
1	Studying heavy ion collisions with dileptons	1
1.1	Physics motivation	1
1.2	Vector mesons from hot and dense phase	3
1.2.1	Elementary reactions	4
1.2.2	Heavy ion collisions and in medium modifications	5
1.2.3	Dileptons - experimental issues	6
1.2.4	The pioneering experiments	8
1.2.5	The HADES spectrometer	10
1.3	Theoretical models	11
1.3.1	Ultra-relativistic quantum molecular dynamics model (UrQMD)	11
1.3.2	The thermal model	13
II	Comparison of the HADES data with the UrQMD transport model calculations	15
2	e^+e^- pairs from heavy ion collisions simulated with UrQMD	16
3	e^+e^- pairs from heavy ion collisions measured with HADES	18
4	Vector meson production in UrQMD	22
5	Excess e^+e^- pair yield systematics in UrQMD	23
5.1	Intermediate mass excess in $^{12}C+^{12}C$ and $^{40}Ar+KCl$ collisions . .	23
5.2	Behavior of the excess pair yield as function of beam energy and system size	25
5.2.1	Nuclear overlap calculation	25
5.2.2	Scaling of the e^+e^- pair yield with the beam energy	27
5.2.3	Scaling of the e^+e^- pair yield with the system size	28
5.3	Trigger considerations	30
III	Modeling of the dense phase in $^{197}Au+^{197}Au$ collisions	33
6	Invariant mass spectra	33
7	Determination of the inverse-slope parameter (T_{eff})	38

8	Inverse-slope parameters at different rapidity bins	40
8.1	Inverse-slope parameters from $^{40}\text{Ar}+^{35}\text{KCl}$ at $1.756\text{ GeV}/u$	40
8.2	Inverse-slope parameters from $^{197}\text{Au}+^{197}\text{Au}$ at $1.25\text{ GeV}/u$	42
9	Inverse-slope parameters for different time steps of the heavy ion collision	43
IV	Summary and Outlook	49
A	Parameters of simulated systems with UrQMD	XI
B	Inverse-slope parameters at different rapidity bins	XII
C	Inverse-slope parameters for different time steps bins of the heavy ion collision	XVII

List of Figures

1.1	The phase diagram of strongly interacting matter	2
1.2	Heavy ion collision simulated with UrQMD	3
1.3	Vector Meson Dominance Model	4
1.4	Invariant e^+e^- mass distribution measured by HADES in pp and np collisions at a beam energy of 1.25 GeV/u compared with UrQMD transport model calculations	5
1.5	Additional contributions to the ρ -meson self-energy in the medium	6
1.6	Dalitz decays of baryonic resonances	6
1.7	Spectral distribution of lepton pairs measured with CMS at LHC	8
1.8	Left panel: The top view of the DLS spectrometer. Right panel: e^+e^- invariant mass spectrum from $^{40}Ca+^{40}Ca$ collisions at 1.0 GeV/u measured with DLS and compared to Hadron String Dynamic transport model calculations	9
1.9	Left panel: Schematic view of HADES spectrometer at SIS18, GSI. Right panel: e^+e^- invariant mass spectrum from $^{40}Ar+KCl$ collisions at a beam energy of 1.756 GeV/u measured by HADES compared to Ultra-relativistic Quantum Molecular Dynamic transport model	10
1.10	Schematic illustration of ρ meson propagation within "shining" approach.	12
1.11	Schematic illustration of ρ meson propagation within "shining" approach.	12
2.1	Schematic overview of the simulation steps	15
2.2	UrQMD model calculations for dilepton invariant mass spectra from $^{12}C+^{12}C$ and $^{40}Ar+KCl$ collisions at beam energies of 1.0, 2.0 and 1.76 GeV/u	17
2.3	Ratio of invariant mass spectra simulated with UrQMD using an impact parameter cut ($b \leq 4fm$) to the one simulated in minimum bias.	19
2.4	UrQMD model calculations for dilepton invariant mass spectra from $^{12}C+^{12}C$ (a),(b) and $^{40}Ar+KCl$ (c) collisions at beam energies of 1.0 GeV/u , 2.0 GeV/u and 1.76 GeV/u . The calculations were performed with the shining method. The simulated data passed the respective HADES acceptance filter.	21
2.5	UrQMD model calculations for dilepton invariant mass spectra from $^{12}C+^{12}C$ (a),(b) and $^{40}Ar+KCl$ (c) collisions at beam energies of 1.0 GeV/u , 2.0 GeV/u and 1.76 GeV/u . The calculations were performed with the shining method and the contribution of the ρ meson was scaled down by a factor of 5.	22

2.6	Multiplicity of the pair yield above the η Dalitz in the mass range $0.15 < M_{e^+e^-} < 0.55 \text{ GeV}/c^2$ as observed by DLS and HADES as function of beam energy and system size.	24
2.7	Same as Fig. 2.6 but here each point is normalized to the corresponding π^0 multiplicity.	25
2.8	Number of participants A_{part} versus the impact parameter b for different systems.	26
2.9	e^+e^- multiplicities extracted from $^{197}\text{Au}+^{197}\text{Au}$ collisions at different energies simulated with UrQMD.	27
2.10	e^+e^- multiplicities extracted from $^{12}\text{C}+^{12}\text{C}$, $^{40}\text{Ar}+KCl$, $^{107}\text{Ag}+^{107}\text{Ag}$ and $^{197}\text{Au}+^{197}\text{Au}$ collisions at the same beam energy simulated with UrQMD	29
2.11	e^+e^- invariant mass spectra of different particles. Different impact parameter regions from $^{197}\text{Au}+^{197}\text{Au}$ (lines) in comparison to central $^{40}\text{Ar}+KCl$ with $b \leq 3.44 \text{ fm}$ (points) Upper Left: π^0 Dalitz, upper right: $\Delta(1232)$ Dalitz decays, lower left: η Dalitz decays, lower right: $\rho \rightarrow e^+e^-$ decay.	31
3.1	Invariant e^+e^- mass spectrum from the $^{197}\text{Au}+^{197}\text{Au}$ collisions at $1.25 \text{ GeV}/u$ simulated UrQMD cocktail	34
3.2	Invariant e^+e^- mass spectra from the $^{197}\text{Au}+^{197}\text{Au}$ collisions at $1.25 \text{ GeV}/u$ at various regions of the emission density	35
3.3	Emission time of dileptons versus emission density for different systems at $1.25 \text{ GeV}/u$	36
3.4	Invariant mass spectra of the ρ meson extracted from various collision systems and for the different values of the emission density.	37
3.5	Problem and solution of a fit with gradient descent.	39
3.6	Example of an effective slope parameters extraction with the χ^2 minimization method. The rapidity distribution (red curve) is shown in (a). The $m_t - m_{inv}$ spectrum (b) is depicted together with all fits of with a $\chi^2 < 10$ (yellow band) and the fits with the final parameters (red curve). Panel (d) shows the T_1 versus T_2 versus χ^2 distribution, and in (c) the extracted temperatures	41
3.7	Rapidity distribution and extracted temperatures of an UrQMD simulation of $^{197}\text{Au}+^{197}\text{Au}$ collisions at $1.25 \text{ GeV}/u$	42
3.8	Time and density were dileptons from different sources of $^{197}\text{Au}+^{197}\text{Au}$ collisions at $1.25 \text{ GeV}/u$ are produced.	43
3.9	Example of the effective slope parameter extraction with the χ^2 minimization method. The emission density (a) is given by the maximum bin and the RMS of the distribution. The $m_t - m_{inv}$ spectrum is depicted together with all fits with a $\chi^2 < 10$ (yellow bend) and the fit with the final parameters (red curve). The other figures show the χ^2 minimization for two (c) and for one (d) temperature.	44

3.10	Emission temperature and emission density versus time from dilepton sources from $^{197}\text{Au}+^{197}\text{Au}$ 1.25 GeV/u.	47
3.11	Emission temperature of dileptons versus emission density of hadrons from $^{197}\text{Au}+^{197}\text{Au}$ 1.25 GeV/u.	48
4.1	Multiplicity of the pair yield above the η Dalitz in the mass range $0.15 < M_{e^+e^-} < 0.55$ GeV/ c^2 as observed by DLS (open triangles) and HADES (full triangles) as function of beam energy and system size, normalized to the corresponding π^0 multiplicity.	49
4.2	Time and density were dileptons from different sources of $^{197}\text{Au}+^{197}\text{Au}$ collisions at 1.25 GeV/u are produced.	50
4.3	Invariant e^+e^- mass spectra from $^{197}\text{Au}+^{197}\text{Au}$ collisions at 1.25 GeV/u at two regions of the emission density	51
4.4	Emission temperature and emission density versus time from π^0 Dalitz decay from $^{197}\text{Au}+^{197}\text{Au}$ collisions at 1.25 GeV/u.	51
A 5	m_t distribution for each rapidity bin of the $\pi^0 \rightarrow \gamma e^+e^-$ decay from $^{40}\text{Ar}+KCl$ collisions at 1.756 GeV/u	XII
A 6	T_1 versus T_2 versus χ^2 for each rapidity bin of the $\pi^0 \rightarrow \gamma e^+e^-$ decay from $^{40}\text{Ar}+KCl$ collisions at 1.756 GeV/u	XIV
A 7	T_1 versus T_2 versus χ^2 for each rapidity bin of the $\pi^0 \rightarrow \gamma e^+e^-$ decay from $^{197}\text{Au}+^{197}\text{Au}$ collisions at 1.25 GeV/u	XV
A 8	m_t distribution for each rapidity bin of the $\pi^0 \rightarrow \gamma e^+e^-$ decay from $^{197}\text{Au}+^{197}\text{Au}$ at 1.25 GeV/u	XVI
A 9	Density profile of $\pi^0 \rightarrow \gamma e^+e^-$ decay for time bins of $^{197}\text{Au}+^{197}\text{Au}$ at 1.25 GeV/u.	XVII
A 10	$m_t - m_{inv}$ spectra of $\pi^0 \rightarrow \gamma e^+e^-$ decay with the best fits and the fit with T_1^* and T_2^* as start parameter for time bins of $^{197}\text{Au}+^{197}\text{Au}$ at 1.25 GeV/u.	XVIII
A 11	T_1 versus T_2 versus χ^2 of $\pi^0 \rightarrow \gamma e^+e^-$ decay for each time bin of $^{197}\text{Au}+^{197}\text{Au}$ at 1.25 GeV/u	XIX
A 12	Density profile of $\eta \rightarrow e^+e^-$ decay for each time bin of $^{197}\text{Au}+^{197}\text{Au}$ at 1.25 GeV/u	XX
A 13	$m_t - m_{inv}$ spectra of $\eta \rightarrow e^+e^-$ decay with the best fits and the fit with T_1^* and as start parameter for each time bin of $^{197}\text{Au}+^{197}\text{Au}$ at 1.25 GeV/u	XXI
A 14	T versus χ^2 of $\eta \rightarrow e^+e^-$ decay for each time bin of $^{197}\text{Au}+^{197}\text{Au}$ at 1.25 GeV/u	XXII
A 15	Density profile of $\Delta_{1232} \rightarrow e^+e^-$ decay for each time bin of $^{197}\text{Au}+^{197}\text{Au}$ at 1.25 GeV/u.	XXIII
A 16	$m_t - m_{inv}$ spectra of $\Delta_{1232} \rightarrow \gamma e^+e^-$ decay with the best fits (yellow, $\chi^2 < 10$) and the fit with T_1^* as start parameter (red)	XXIV
A 17	T_1 versus χ^2 of $\Delta_{1232} \rightarrow \gamma e^+e^-$ decay for each time bin of $^{197}\text{Au}+^{197}\text{Au}$ at 1.25 GeV/u	XXV
A 18	Density profile of $\rho \rightarrow e^+e^-$ decay of $^{197}\text{Au}+^{197}\text{Au}$ at 1.25 GeV/u	XXVI

A 19	$m_t - m_{inv}$ spectra of $\rho \rightarrow e^+e^-$ decay with the best fits and the fit with T_1^* and as start parameter of $^{197}\text{Au}+^{197}\text{Au}$ at $1.25 \text{ GeV}/u$. .	XXVII
A 20	T_1 versus χ^2 for $\rho \rightarrow e^+e^-$ decay at each time bin of $^{197}\text{Au}+^{197}\text{Au}$ at $1.25 \text{ GeV}/u$	XXVIII

List of Tables

1.1	Quantities of light vector mesons	4
2.1	Multiplicities of resonances from simulation of $^{12}\text{C}+^{12}\text{C}$ collisions at 1.0 GeV/u and at 2.0 GeV/u and $^{40}\text{Ar}+^{36}\text{Ar}$ collisions at 1.756 GeV/u	18
2.2	π^0 and η multiplicities of TAPS compared with UrQMD in minimum bias [mb] and impact parameter cut [b_{cut}]	19
2.3	The maximum impact parameters and the corresponding number of participants in different simulated collision systems.	26
2.4	Multiplicities of resonances from $^{197}\text{Au}+^{197}\text{Au}$ collisions at different beam energies.	28
2.5	Meson multiplicities extracted from $^{12}\text{C}+^{12}\text{C}$, $^{40}\text{Ar}+^{36}\text{Ar}$, $^{107}\text{Ag}+^{107}\text{Ag}$ and $^{197}\text{Au}+^{197}\text{Au}$ collisions at $E_{beam} = 1.25 \text{ GeV}/u$	30
2.6	Mean number of participants in $^{197}\text{Au}+^{197}\text{Au}$ collisions in different impact parameter regions.	31
3.1	Decay multiplicities of resonances in $^{197}\text{Au}+^{197}\text{Au}$ collisions in dense and diluted phases	34
3.2	The selected fit regions and start values of T_1 and T_2	45
A 1	Parameters of simulated systems	XI
A 2	Temperatures and densities of the $\pi^0 \rightarrow \gamma e^+ e^-$ decay for different Y bins in $^{40}\text{Ar}+^{36}\text{Ar}$ collisions	XIII
A 3	Temperatures and densities of the $\pi^0 \rightarrow \gamma e^+ e^-$ decay for different Y bins in $^{197}\text{Au}+^{197}\text{Au}$ collisions	XIII
A 4	Temperatures and densities of dileptons from π^0 Dalitz decay for different time bins in $^{197}\text{Au}+^{197}\text{Au}$ collisions at 1.25 GeV/u	XXIX
A 5	Temperatures and densities of dileptons from $\eta \rightarrow e^+ e^-$ for different time bins in $^{197}\text{Au}+^{197}\text{Au}$ collisions at 1.25 GeV/u	XXIX
A 6	Temperatures and densities of dileptons from $\Delta(1232)$ Dalitz decay for different time bins in $^{197}\text{Au}+^{197}\text{Au}$ collisions at 1.25 GeV/u	XXX
A 7	Temperatures and densities of dileptons from ρ decay for different time bins in $^{197}\text{Au}+^{197}\text{Au}$ collisions at 1.25 GeV/u	XXX

Part I

Introduction and Motivation

*Any intelligent fool can make things bigger,
more complex, and more violent.
It takes a touch of genius
- and a lot of courage -
to move in the opposite direction.*

Albert Einstein

1 Studying heavy ion collisions with dileptons

1.1 Physics motivation

Approximately 13.7 billion years ago, the entirety of our universe was compressed into the confines of atomic nucleons. With the help of their astronomy colleagues, cosmology theorists have been successful in reconstructing the primordial chronology of events known as the big bang. Circa 10^{-6} seconds after the big bang elementary particles were formed. Today these particles are described with the standard model [N⁺10], containing 12 leptons and 4 bosons. The standard model also describes the interaction between the particles. Free quarks have not been isolated, and therefore can not be directly observed. This is known as confinement. Quarks are forming together in groups of two (mesons) or three (baryons). It is interesting to understand how the properties (mass, width) of mesons and baryons change once they are embedded inside hot and dense matter.

The exploration of the phase diagram of strongly interacting matter is one of the main topics in the modern nuclear physics. Heavy ion collisions provide a possibility to study the matter under extreme conditions in the laboratory. Experiments deal with various types of beams ranging from photons and leptons to relativistic heavy ions. The abundantly observed particles are hadrons (pions, kaons, protons, etc.), but the most promising tool to probe the in-medium properties is electromagnetic radiation. Short lived mesons and baryons are produced and decay inside a nucleus or inside a fireball of strongly interacting constituents.

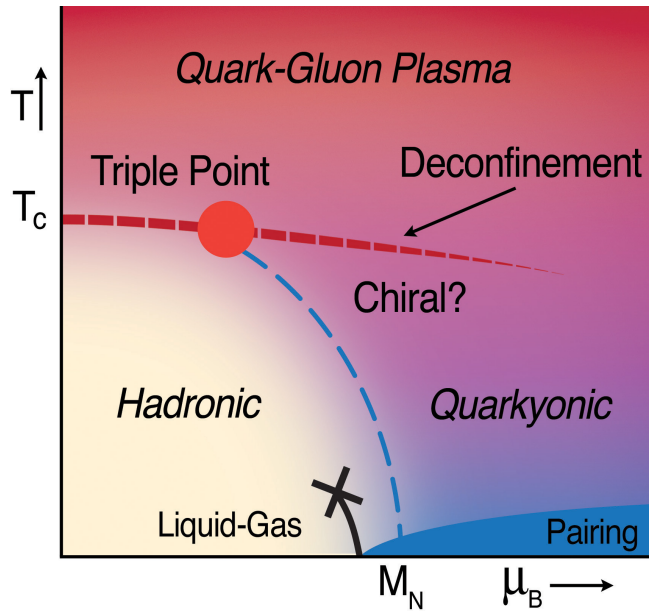


Figure 1.1: The phase diagram of strongly interacting matter. [ABBM⁺10]

Depending on temperature and density, nuclear matter exists in the form of hadron gas, quark-gluon plasma or more exotic forms. A phase diagram displays the regions of temperature and density where the different phases are realized, as shown in Fig. 1.1. The matter which is formed during the big bang has high temperatures and zero μ_B (equal amount of matter and anti-matter), it cools down until it reaches nearly zero temperature and a density of $\rho_0 = 0.17 fm^{-3}$. In this regime quarks are bound in hadrons. When the temperature of a system increases, the hadrons occupy more and more of the available space and start to overlap. The initially confined quarks and gluons separate and create new degrees of freedom, differed from the hadronic one. This deconfined phase is called quark-gluon plasma (QGP) [MP07].

At higher baryon chemical potentials and higher temperatures a first order phase transition is expected [ABBM⁺10]. Pieces of deconfined matter embedded in a gas of hadrons are expected in a coexisting phase there. Going to lower chemical potentials a tri-critical point is predicted, in which the coexistence phase should terminate [K⁺04]. At even smaller baryochemical potentials a smooth cross-over between the two phases is predicted by Lattice QCD [FK04].

Yet another state of nuclear matter was recently predicted called quarkyonic matter. It is reached at moderate temperatures and high net-baryon densities. In this phase, nuclear matter is still confined. It is not fully understood if chiral symmetry is restored in this phase. The number of degrees of freedom is significantly larger compared to the number of degrees of freedom of hadronic matter [ABBM⁺10]. At asymptotically high net-baryon densities and low temperatures a color superconducting phase is predicted [ASRS08].

1.2 Vector mesons from hot and dense phase

In order to transfer nuclear matter into the deconfined phase one has to heat the system up or increase the baryon chemical potential. Heavy ion collisions are the only way to reach these conditions in the laboratory.

In general a heavy ion collision can be separated into three stages. In the first stage the first chance collisions take place. Then a hot and/or dense stage (so called "fireball") occurs. The fireball expands rapidly and cools down. Finally, the system can be found in chemical and thermal equilibrium signaling the end of the heavy ion collision. In the last stage (freeze-out stage) the quarks are confined back to hadrons.

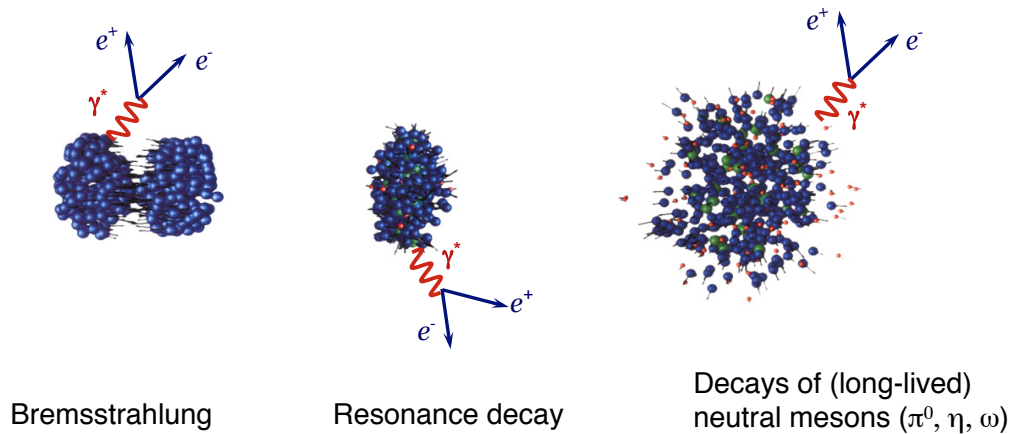


Figure 1.2: Heavy ion collision simulated with UrQMD. Three stages of the heavy ion collision are shown. Sources of the lepton pairs from each stage are indicated.

Unfortunately, strongly interacting particles can not leave the hot and dense stage without distortion of their primary information. Photons (γ) and leptons, on the other hand, are penetrating the dense phase without strong interactions. By the decay of virtual photons (γ^*) lepton pairs are emitted during the whole evolution of the heavy ion collision (see Fig. 1.2). In the first chance collision stage at beam energies of a few GeV/u , the main source of lepton pairs is NN Bremsstrahlung. In the freeze out stage long lived sources which decay into lepton pairs directly or through Dalitz decays are the dominant contributions. These are mainly π^0 , η and ω mesons. The short lived sources, i.e. ρ vector mesons and baryonic resonances like $\Delta(1232)$ and N^* , are the best tool to access the dense stage of the heavy ion collision.

I Introduction and Motivation

In-medium modifications of vector mesons are signatures for possible phase transitions. The neutral vector mesons have the same quantum numbers as the virtual photon, meaning electric neutral charge, negative parity ($J^P = 1^-$) and a spin 1.

Meson	Mass [MeV/c ²]	Decay width [MeV/c ²]	Life time [fm/c]	Branching ratio e^+e^-
ρ	775	149	1.3	$4.72 \cdot 10^{-5}$
ω	783	8.49	23.4	$7.28 \cdot 10^{-5}$
ϕ	1020	4.26	44.4	$295 \cdot 10^{-4}$

Table 1.1: Quantities of light vector mesons [N⁺10]

J.J Sakurai introduced the Vector Meson Dominance Model which describes photon-hadron interactions [Sak60]. It describes how energetic photons get a hadronic character. This is illustrated in Fig. 1.3 showing $\pi\pi$ annihilation proceeding via an intermediate ρ meson, which couples to a virtual photon decaying into a lepton pair. In accordance with a model of Gell-Mann and Zweig the photon should behave as if it was composed of 75% ρ -meson, 8% ω -meson and 17% ϕ -meson, [Gal09].

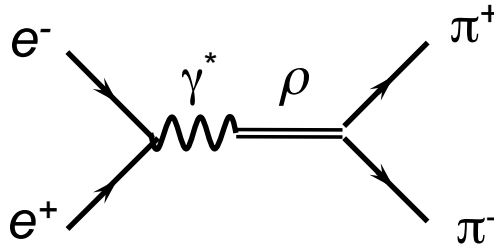


Figure 1.3: The Vector Meson Dominance Model. $\pi\pi$ annihilation proceeding via an intermediate ρ meson, which couples to a γ^*

1.2.1 Elementary reactions

Elementary reactions are proton-proton and proton-neutron collisions. In elementary collisions no dense and hot phase occurs, which makes them a good reference for comparison with heavy ion collisions. In general each particle can only be produced if the center of mass energy (\sqrt{s}) is equal to or larger than the pole mass of that particle. This is related to energy and momentum conservation. However, keeping in mind the Vector Meson Dominance model, a sub-threshold production of broad resonances can be realized. For invariant masses larger than $0.45 \text{ GeV}/c^2$ a noticeable contribution from $\rho \rightarrow e^+e^-$ decay is visible. In models this effect is observed when an explicit treatment of meson production via resonant mechanism is included, like shown in Fig. 1.4.

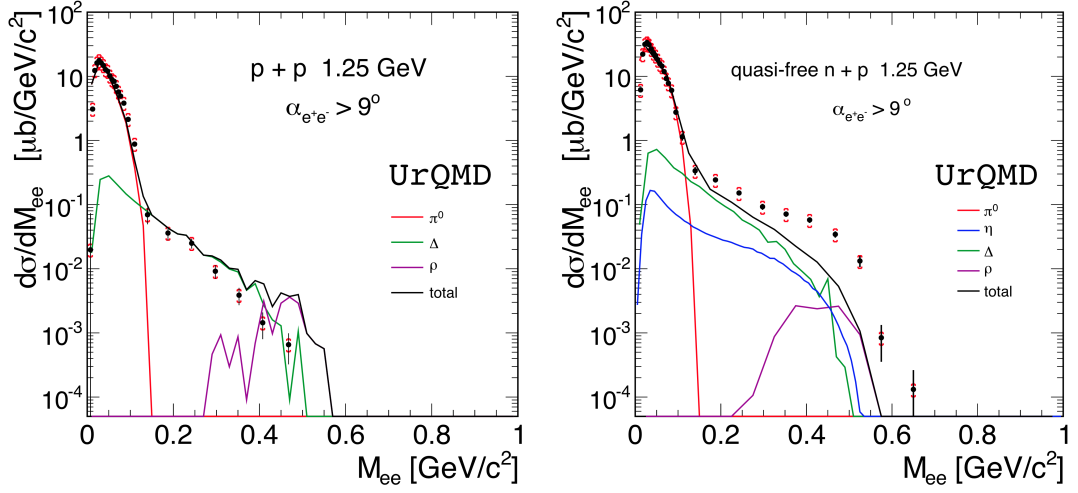


Figure 1.4: Invariant e^+e^- mass distribution measured by HADES in pp (left) and np (right) collisions at a beam energy of $1.25 \text{ GeV}/u$ [$A+10$] compared with UrQMD transport model calculations. Note, a contribution from ρ decays is visible at this low beam energies

1.2.2 Heavy ion collisions and in medium modifications

It is predicted that the hadrons, which are embedded inside nuclei, change their properties. In heavy ion collisions nucleons are excited into baryonic resonance states (Δ , N^*). They decay by emitting mesons, which couple to a γ^* . The presence of baryons influences the vector meson spectral function in the medium. The ρ meson couples strongly to the 2π channel. Thus it can be seen as a broad $\pi + \pi$ resonance. Therefore, modifications of the ρ meson properties in hadronic matter can be linked to medium-dependent π propagation properties. Analog to the vacuum polarization of a photon [LKH⁺97] the ρ meson can create virtual π^+ and π^- pairs while propagating in the vacuum.

With the presence of a medium the ρ meson self-energy becomes much more complex. Significant modifications of the ρ meson width are expected, since π couple strongly to δ -hole states in the medium. The direct coupling of the ρ meson to the baryonic resonances is also possible. These two scenarios are illustrated in Fig. 1.5. The right loop shows the direct appearance of a resonance-hole pair. This process becomes much more prominent at lower beam energies. It is explained in [FP97] where a strong coupling of the ρ meson to the baryonic resonances plays a major role in modifications of the ρ .

To summarize, additional contributions to the ρ meson self-energy changes the width of the ρ . Therefore the broadening of the ρ meson is a hint to existence of the medium.

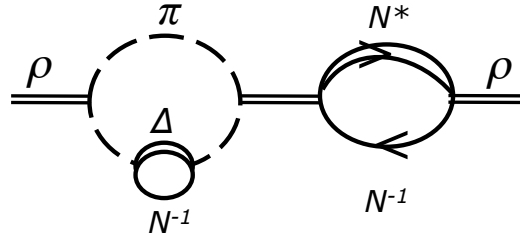


Figure 1.5: Additional contributions to the ρ -meson self-energy in the medium

At SIS energy regime excitation of nucleons to resonances is a dominant process. Here the virtual photon couples strongly to the baryonic resonances via the intermediate ρ meson. This process is shown in Fig. 1.6, where, because of the VMD, the ρ meson couples to a virtual photon and its decay into a dilepton pair.

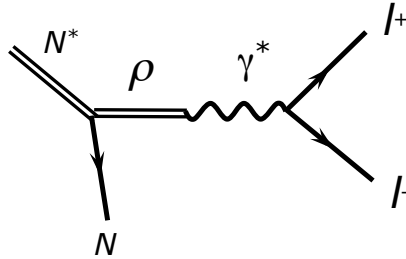


Figure 1.6: Dalitz decays of baryonic resonances. The dominant source of e^+e^- pairs with masses larger than M_π at low beam energies

The VMD is a good tool to understand the nature of in medium effects, and, moreover it connects between high and low beam energy regimes.

1.2.3 Dileptons - experimental issues

For measuring dileptons the invariant mass ($M_{l^+l^-}$, $l = e, \mu$) is an imported kinematic observable. The lepton pair mass is equal to the transferred energy which is given by the Lorentz invariant mass of the virtual photon:

$$M_{l^+l^-} \cdot c^2 = \sqrt{(E_{l^+} + E_{l^-})^2 + (\vec{p}_{l^+} \cdot c + \vec{p}_{l^-} \cdot c)^2}, \quad (1)$$

where E_{l^\pm} is the total energy, p_{l^\pm} is the momentum in the laboratory system and c is the speed of light. If the rest mass of the lepton is small compared to the

energies involved and the relativistic limit $E_{l\pm} \approx |p|$ is reached, the equation (1) can be simplified to:

$$M_{l+l-} \cdot c^2 = 2 \sin \frac{\theta_{l+l-}}{2} \cdot \sqrt{\vec{p}_{l+} \cdot \vec{p}_{l-}}. \quad (2)$$

This allows for a definition of the invariant mass as a function of the opening angle (θ_{l+l-}) between the emitted leptons, and the three momentum of the lepton pair.

Another important kinematic observable is the transverse momentum p_t of the lepton pair, which is invariant under a boost in beam (z) direction. It can be calculated with

$$p_t = \sqrt{(p_{l+x} + p_{l-x})^2 + (p_{l+y} + p_{l-y})^2}. \quad (3)$$

Rapidity, which describes the parallel component of the momentum, is Lorentz invariant, too. It is also constant under a boost in the beam direction. It can be calculated in the following way:

$$y = \frac{1}{2} \ln \frac{(E) + (p_{l+z} + p_{l-z})}{(E) - (p_{l+z} + p_{l-z})}. \quad (4)$$

Figure 1.7 shows a spectral distribution of lepton pairs, emitted in ultra-relativistic proton-proton collisions as measured with the CMS spectrometer at LHC, CERN. Up to $0.15 \text{ GeV}/c^2$ the spectrum is dominated by π^0 Dalitz decay (not seen in the spectrum because of the limited acceptance). The peak at $0.55 \text{ GeV}/c^2$ belongs to the direct decays of the η meson ($\eta \rightarrow e^+e^-$). In the so called vector meson region from 0.55 to $1.2 \text{ GeV}/c^2$ the ω and ρ decays are prominent. The ω peak is clearly visible, but the ρ spectra which has a width of $0.15 \text{ GeV}/c^2$, can not be separated clearly. The peak at $1.020 \text{ GeV}/c^2$ belongs to the ϕ meson decay, which is the lightest meson that contains $s\bar{s}$ pairs as valence quarks. Around $3 \text{ GeV}/c^2$ one can see the peak of the J/ψ resonance and its first excited state ψ' . It is the lightest quark which contains $c\bar{c}$ pairs. At around $10 \text{ GeV}/c^2$ the $b\bar{b}$ -resonance and its three excited states are visible. The unexcited state, Υ , has a pole mass about $9.46 \text{ GeV}/c^2$. Even the Z boson is nicely visible at an invariant mass of $100 \text{ GeV}/c^2$.

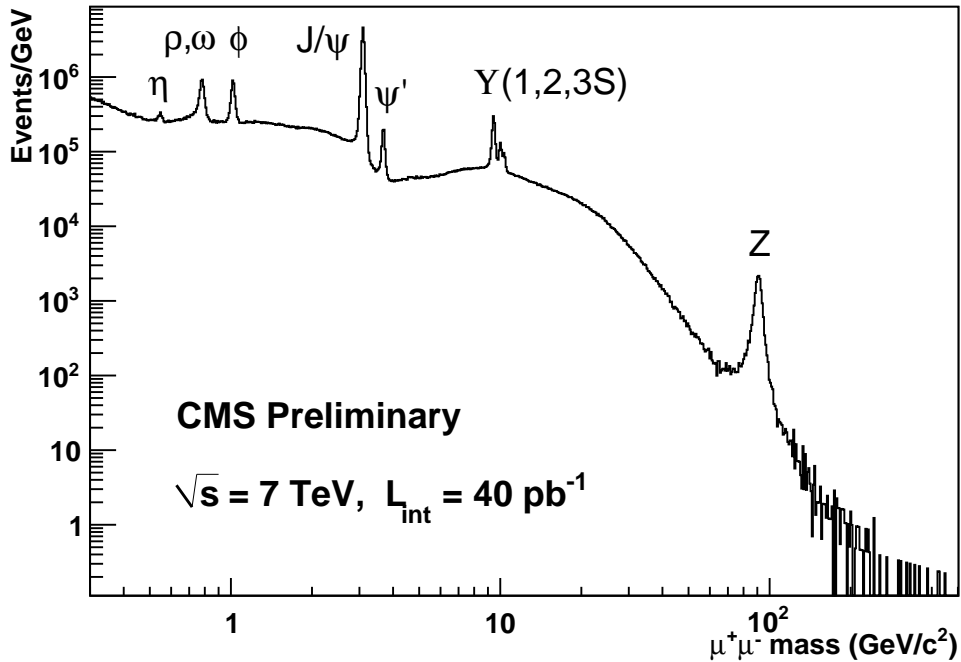


Figure 1.7: Spectral distribution of lepton pairs emitted in ultra-relativistic heavy ion collisions, measured with CMS at LHC, CERN [CMS]

1.2.4 The pioneering experiments

Different experimental set-ups have been build to investigate modifications of the hadron properties due to the interaction with hot and dense matter. The ChErenkov Ring Electron Spectrometer (CERES) and NA60 experiments at CERN (SPS) have measured dilepton production at beam energies from 40 to 158 GeV/u . These experiments demonstrate a significant additional yield (excess pair yield) of lepton pairs above the trivial hadronic cocktail in the invariant mass region below the ρ meson pole mass. This can be interpreted as a broadening of the ρ -meson due to the in-medium changes of its spectral function. It has been established that baryon-driven medium effects are the key in describing the low-mass CERES and NA60 data. As it has been discussed before, medium effects at moderate energies are closely linked to the effects at high beam energies through VMD. However, for a long time the excess e^+e^- pair yield measured at beam energies of a few GeV per nucleon could not be explained by any theoretical model.

1 Studying heavy ion collisions with dileptons

One of the first experiments in the low energy regime was the DiLepton Spectrometer (DLS), which was installed at the Bevalac accelerator (Lawrence Berkeley National Laboratory, Berkeley) and operated from 1988 until 1993. The main aim of the DLS collaboration was to study the behavior of low mass electron pairs in elementary and heavy ion collisions.

A schematic top view of the DLS spectrometer is shown in Fig. 1.8 (left panel). The DLS spectrometer consists of two identical arms. Each one contains three drift chambers, two Cherenkov counters, two scintillator counters and a large dipole magnet. The minimum opening angle between e^+e^- was around 40° . A mass resolution of 15% at the ω pole mass was achieved. Systematical errors of measurements were at the level of 30-40%. A more detailed description can be found in [R⁺88]. The DLS spectrometer measured p+p, d+p, $^{12}\text{C}+^{12}\text{C}$ and

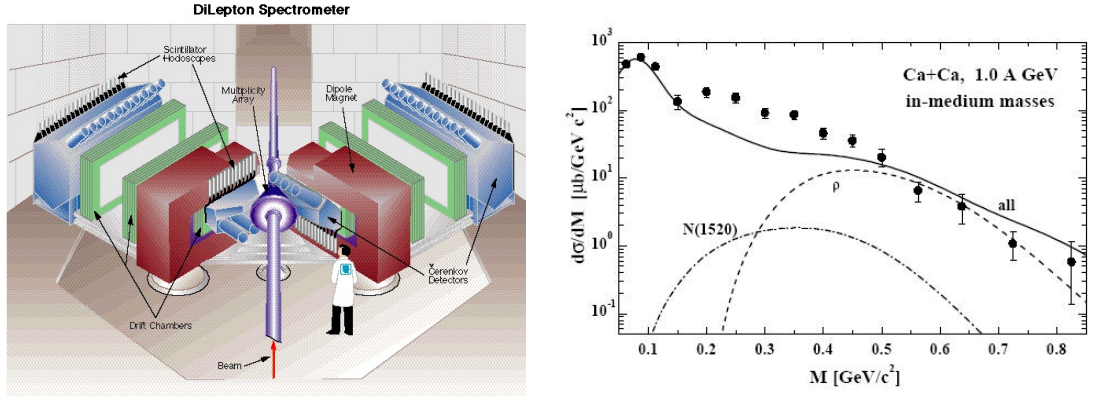


Figure 1.8: Left panel: The top view of the DLS spectrometer. Right panel: e^+e^- invariant mass spectrum from $^{40}\text{Ca}+^{40}\text{Ca}$ collisions at 1.0 GeV/u measured with DLS and compared to Hadron String Dynamic transport model calculations

$^{40}\text{Ca}+^{40}\text{Ca}$ collisions at different beam energies. The p+p data (beam energies: 1.04 GeV/u , 1.27 GeV/u , 1.61 GeV/u , 1.85 GeV/u , 2.09 GeV/u , 4.88 GeV/u) are in fair agreement with theory [WBB⁺98].

The interpretation of the $d+p$ data turned out to be non-trivial. The theoretical descriptions of the heavy ion measurements failed. Fig. 1.8 (right panel) shows the $^{40}\text{Ca}+^{40}\text{Ca}$ measurements and contributions of different resonances simulated with Hadron String Dynamic transport model calculations [BK99]. This discrepancy raised up the question of the correctness of the DLS data or of important missing sources of low mass lepton pairs in models. This was worth the title "DLS puzzle".

1.2.5 The HADES spectrometer

To study e^+e^- pairs in cold nuclear matter, in heavy ion collisions as well as in elementary collisions, the High Acceptance DiElectron Spectrometer (HADES) is installed at the SIS 18 (GSI Helmholtzzentrum für Schwerionenforschung, Darmstadt). One of the goals was to validate the DLS pair excess and to solve the "DLS puzzle".

It is build of 6 identical sectors, that covers a full azimuthal angle and polar angles from 18° to 85° . It consists of 24 multi-wire drift chambers, which, together with the superconducting toroidal magnet, are responsible for the tracking. The magnet provides a momentum kick, which is necessary to obtain charged particle momentum with a resolution of about 1% in a wide momentum range. The separation between leptons and hadrons is realized with a Ring Imaging Cherenkov detector. To further suppress hadrons the time-of-flight information is used. Time-of-flight measurements are accomplished by the TOF detector at high polar angles and TOFinno (now replaced by RPC) at small polar angles. Moreover information on electromagnetic shower helps to remove remaining hadron contamination.

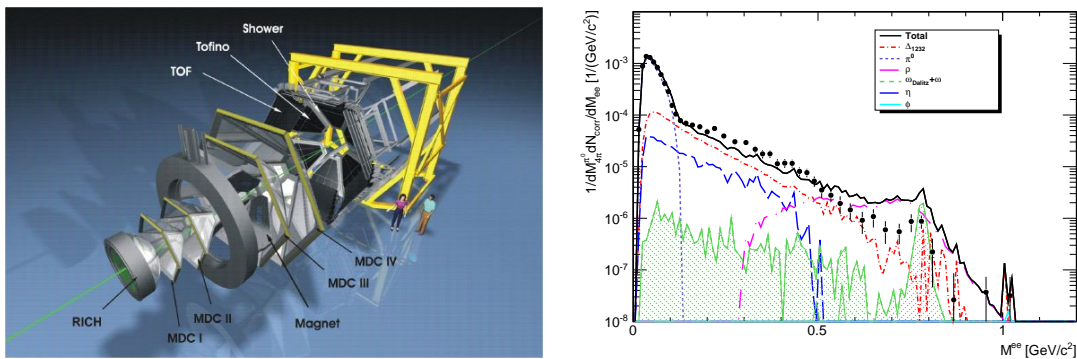


Figure 1.9: Left panel: Schematic view of HADES spectrometer at SIS18, GSI. Right panel: e^+e^- invariant mass spectrum from $^{40}\text{Ar}+KCl$ collisions at a beam energy of $1.756 \text{ GeV}/u$ measured by HADES compared to Ultra-relativistic Quantum Molecular Dynamic transport model

The HADES detector setup is shown in Fig. 1.9 (left panel). More details can be found in [A⁺09]. The heavy ion measurements show the same behavior like the former DLS data. The excess pair yield in the low mass region is studied intensively with the HADES spectrometer. The latest results can be found in [A⁺11] and [A⁺10]. After confirmation of the DLS data by the HADES collaboration, the experimental issues of the "DLS puzzle" were solved. Recent HADES results on e^+e^- production in $^{40}\text{Ar}+KCl$ collisions show at intermediate e^+e^- invariant masses, a strong enhancement of the dilepton yield over a reference spectrum reconstructed from elementary nucleon-nucleon reactions, suggesting the onset of non-trivial effects of the nuclear medium. This will be discussed in section 4.

1.3 Theoretical models

A large effort has been made by theoretical groups to investigate the in-medium properties of the vector mesons based on microscopic transport models and using the thermal description of e^+e^- radiation. In this section the ultra relativistic quantum molecular dynamics model and thermal model will be discussed.

1.3.1 Ultra-relativistic quantum molecular dynamics model (UrQMD)

To describe elementary and heavy ion collisions in a wide range of bombarding energies ($E_{kin} = 3 - 200 \text{ GeV}/u$) the UrQMD microscopic transport model was developed. It explicitly follows the trajectories of all hadrons, thus providing full information about the dynamical evolution of the system. Particle production is realized via creation and decay of resonances, which are included in the model. At each time step the collision criterion $b < \sqrt{\frac{\sigma_{tot}}{\pi}}$, where b is the impact parameter and σ_{tot} is the total cross section, is checked. If the collision criterion is applicable the collision is done. The probability to produce particles is defined by the particle cross section.

The decay of light vector mesons into dileptons is included in the UrQMD transport model as well. The suppression of the production with the squared electromagnetic coupling constant makes dileptons from vector meson decays a rare probe. The branching ratio of $7 \cdot 10^{-5}$ ($\rho \rightarrow e^+e^-$) means that just 1 out of $2 \cdot 10^4$ ρ mesons decays electromagnetically.

To overcome this problem the UrQMD model uses the time integration method which is described in details in [HL92]. The time integration method (also called "shining") assumes that a resonance can continuously emit dileptons over its whole lifetime. The dilepton yield is obtained by integration of the dilepton emission rate over time, taking the collisional broadening of each individual parent resonance into account.

In Fig. 1.10 a schematic view of a ρ meson propagation is shown. During its life time (τ) it moves a distance ($c \cdot \tau$) and emits ("shines") virtual photons (γ^* , wavy red lines). Each of these virtual photons decays into an e^+e^- pair. Finally the ρ meson decays into π^+ and π^- .

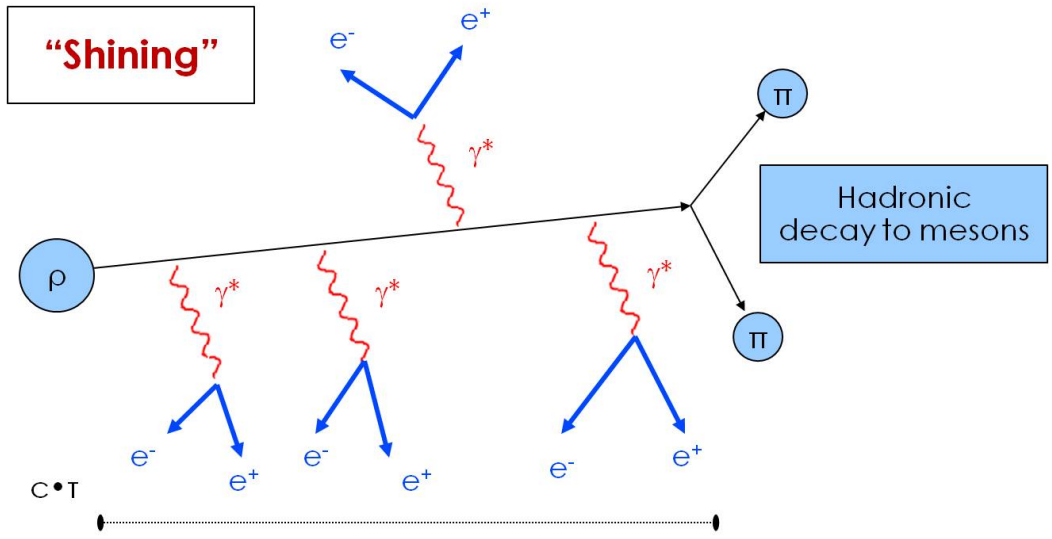


Figure 1.10: Schematic illustration of ρ meson propagation within "shining" approach.

Another scenario is such that a given resonance collides with another resonance before it has the chance to decay. In Fig. 1.11 such a scenario is shown schematically. The ρ meson collides with a nucleon and creates an excited N^* resonance. Before this collision happens the ρ meson emits virtual photons. If the resonance decays back to a ρ and a nucleon, the ρ meson emits γ^* again. Both scenarios are included in the "shining" method of the UrQMD transport model.

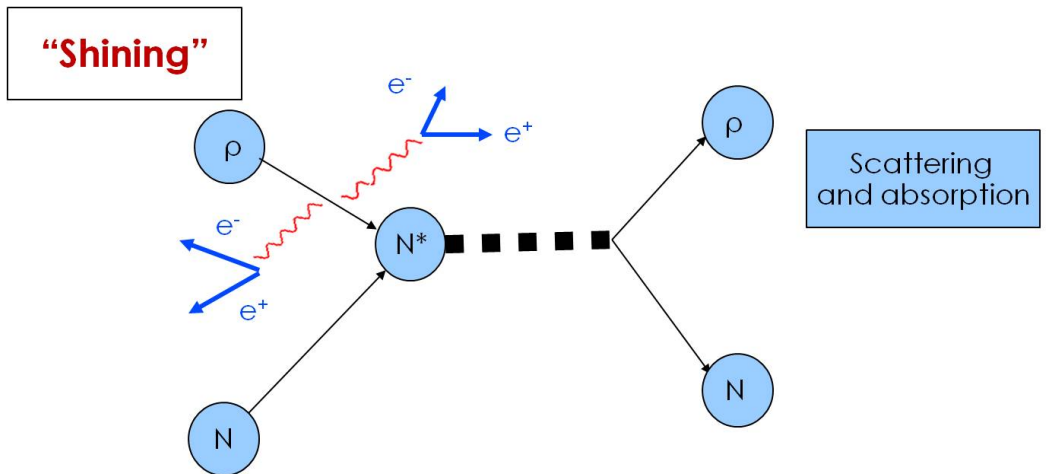


Figure 1.11: Schematic illustration of ρ meson propagation within "shining" approach. Here the ρ meson is absorbed by a hadronic resonance.

1.3.2 The thermal model

In contrast to the microscopic transport approach the thermal model reduces the theoretical problem to a tractable form. The "fireball" model for heavy ion collisions was originally proposed by Westfall [WGJ⁺76]. The collision is approximated in terms of two uniform spheres (one for the target, one for the projectile) whose participants sweep out cylindrical cuts from each other. Then a single "fireball" is formed, which is at rest in the center-of-mass system.

The collision energy is assumed to be completely thermalized in the fireball system. The fireball expands isotropically with momentum distributions of the participants described by Maxwell-Boltzmann distributions. The time scale of the volume expansion is taken from experiment [Sta96]. The geometries determine the relative numbers of participants and spectators and the effective temperature of the fireball.

Under the condition of an evolving thermalized system, equation 5 describes the emitted spectrum of dileptons:

$$\frac{d^M}{dM dP_t dy} = \text{fireball evolution} \cdot \frac{dN}{d^4x d^4q} \cdot \text{acceptance}. \quad (5)$$

The emission rate of virtual photons $\frac{dN}{d^4x d^4q}$ can be delivered from the individual spectral function of the resonances $R(q, T, \rho_B)$.

$$\frac{dN}{d^4x d^4q} = \frac{\alpha^2}{12\pi^4} \frac{R(q, T, \rho_B)}{e^{\beta q^0} - 1} \quad (6)$$

T is the temperature of the emitting volume element, q is the 4-momentum of the emitted lepton pair, and ρ_B its baryon density.

The fireball evolution encodes information on the radiating volume, the baryon chemical potential ρ_B , the transverse flow velocity ν_T , the rapidity y , the temperature T and chemical non-equilibrium properties such as π chemical potential ρ_π [RR06].

The in-medium spectral function $R(q, T, \rho_B)$ can be deduced from the measured spectral distribution, if the evolution of the fireball is known.

I Introduction and Motivation

Part II

Comparison of the HADES data with the UrQMD transport model calculations

*Dans la vie, rien n'est à craindre,
tout est à comprendre.*

Marie Curie

In this section I will compare of the HADES data with the UrQMD transport model calculations. Fig. 2.1 shows the simulation scheme, which I have used in this work. First, nucleon-nucleon or heavy ion collisions are simulated. The standard output files (i.e. file13 and file14) contain the phase space of the event at a given time step of a collision (e.g. final output after last time step). File13 contains the same information as file14, but additionally lists the freeze-out coordinates in configuration and momentum space for all particles. The collision history file (file15) contains information on all collisions/decays of a given event. It contains each binary interaction, resonance decay and string excitation which occurred in the course of the heavy ion collision. It can be used to reconstruct the entire space time evolution of the event. As next step the time integration method is performed. It uses file14 and file15 files from UrQMD output. In the last step the out coming ASCII files were converted into NTuples, which can be analyzed by ROOT analyses macros. In addition the HADES acceptance filter might be applied.

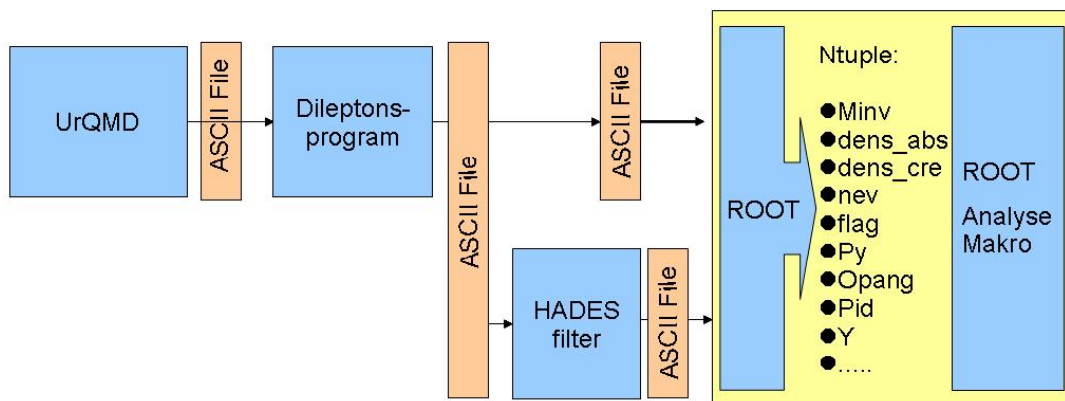


Figure 2.1: Schematic overview of the simulation steps

II Comparison of the HADES data with the UrQMD transport model calculations

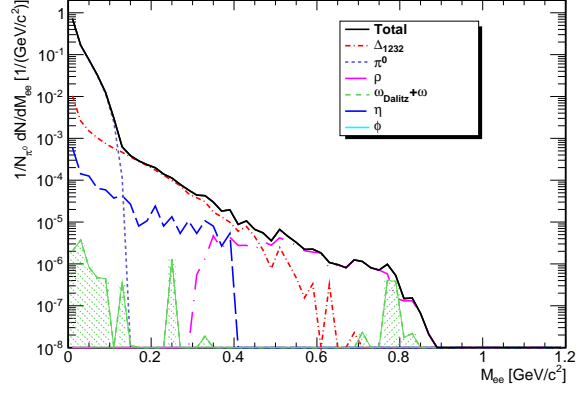
To study in a systematic way the origin of the e^+e^- pair yield and its dependence on the beam energy and system size a large amount of simulated data is needed. We have simulated $^{12}\text{C}+^{12}\text{C}$ and $^{40}\text{Ar}+^{136}\text{Xe}$ at beam energies already measured by the HADES. In order to complete the systematics, HADES propose to continue the investigations with larger collision systems and at the highest possible beam energies achievable at SIS18, as for example with the $^{107}\text{Ag}+^{107}\text{Ag}$ system at $1.65\text{ GeV}/u$ and $^{197}\text{Au}+^{197}\text{Au}$ system at $1.25\text{ GeV}/u$. These systems have been simulated as well. We have also extended our simulations up to the beam energies of $8\text{ GeV}/u$ which will be provided for HADES by SIS100 at the future FAIR facility.

2 e^+e^- pairs from heavy ion collisions simulated with UrQMD

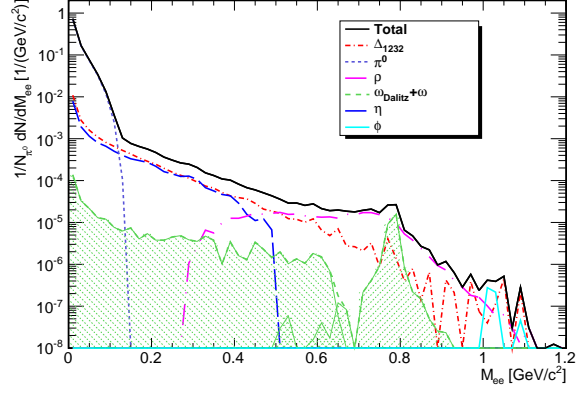
HADES started to investigate di-electron production in nucleus-nucleus collisions with the $^{12}\text{C}+^{12}\text{C}$ measurements at $1\text{ GeV}/u$ and at $2\text{ GeV}/u$. Later the $^{40}\text{Ar}+^{136}\text{Xe}$ collision system at $1.756\text{ GeV}/u$ has been measured. In this section, I will compare the experimental results with UrQMD transport model calculations. We would like to learn how different collision energy, eventually different system size, influences the distribution of invariant e^+e^- masses.

The simulated invariant e^+e^- mass spectra are shown in Fig. 2.2. The characteristic peak at $M_{e^+e^-} < 0.15\text{ GeV}/c^2$ is dominated by Dalitz decays of neutral π^0 . In $^{12}\text{C}+^{12}\text{C}$ collisions at $1.0\text{ GeV}/u$ the e^+e^- pairs from $\Delta(1232)$ Dalitz decays are the main contributions at invariant masses from $0.15 - 0.55\text{ GeV}/c^2$. The e^+e^- pairs from the η Dalitz decay, which is here produced at its threshold, contributes to the spectrum on the level of 30%. The ρ meson decay is also visible from at $M_{e^+e^-}$ from 0.25 to $0.9\text{ GeV}/c^2$. This is a broad resonance since its life time is $1.3\text{ fm}/c$. Due to the coupling of the ρ to the baryonic resonances, it contributes to the dilepton spectrum at the lowest energies, although reduced, is still visible and distinguishable. Even a small contribution of dileptons from the $\omega \rightarrow e^+e^-$ decay can be seen around $0.8\text{ GeV}/c^2$. In $^{12}\text{C}+^{12}\text{C}$ collisions at $2.0\text{ GeV}/u$ one observes a dramatic difference to the spectrum. Here intermediate mass range (from $0.15 - 0.55\text{ GeV}/c^2$) is populated by $\Delta(1232)$ and η Dalitz decays. Also the ω Dalitz and ω direct decays become visible. In $^{40}\text{Ar}+^{136}\text{Xe}$ collisions at $1.756\text{ GeV}/u$ in the mass region from 0.15 to $0.55\text{ GeV}/c^2$ the $\Delta(1232)$ contribution becomes dominant. At $0.8\text{ GeV}/c^2$ the clear $\omega \rightarrow e^+e^-$ peak is visible. Even a small contribution of dileptons from ϕ decays can be seen around $1.0\text{ GeV}/c^2$. The integrated meson multiplicities are summarized in Table 2.1.

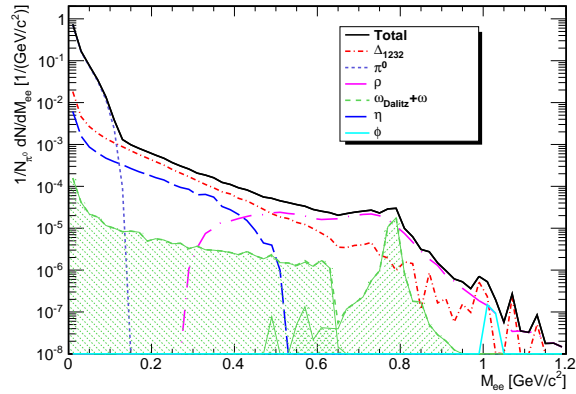
2 e^+e^- pairs from heavy ion collisions simulated with UrQMD



(a) invariant e^+e^- mass spectrum from $^{12}\text{C}+^{12}\text{C}$ collisions at $1.0 \text{ GeV}/u$



(b) invariant e^+e^- mass spectrum from $^{12}\text{C}+^{12}\text{C}$ collisions at $2.0 \text{ GeV}/u$



(c) invariant e^+e^- mass spectrum from $^{40}\text{Ar}+KCl$ collisions at $1.756 \text{ GeV}/u$

Figure 2.2: UrQMD model calculations for dilepton invariant mass spectra from $^{12}\text{C}+^{12}\text{C}$ (a),(b) and $^{40}\text{Ar}+KCl$ (c) collisions at beam energies of $1.0 \text{ GeV}/u$, $2.0 \text{ GeV}/u$ and $1.76 \text{ GeV}/u$. The calculations were performed with the shining method.

II Comparison of the HADES data with the UrQMD transport model calculations

Resonance	$^{12}C+^{12}C$ 1.0 GeV/u	$^{12}C+^{12}C$ 2.0 GeV/u	$^{40}Ar+KCl$ 1.756 GeV/u
π^0	0.57	1.36	2.44
$\Delta(1232)$	0.011	0.028	0.085
η	$6.85 \cdot 10^{-4}$	0.021	0.029
ρ	$2.87 \cdot 10^{-5}$	$4.752 \cdot 10^{-4}$	$1.117 \cdot 10^{-3}$
ω	$5.65 \cdot 10^{-6}$	$4.503 \cdot 10^{-4}$	$9.358 \cdot 10^{-4}$
ϕ	0	$7.323 \cdot 10^{-7}$	$5.941 \cdot 10^{-7}$

Table 2.1: Multiplicities of resonances from simulation of $^{12}C+^{12}C$ collisions at 1.0 GeV/u and at 2.0 GeV/u and $^{40}Ar+KCl$ collisions at 1.756 GeV/u.

3 e^+e^- pairs from heavy ion collisions measured with HADES

In this section we present calculations for dilepton spectra in $^{12}C+^{12}C$ collisions at 1 GeV/u and 2 GeV/u and compare them to the data resulting from the measurements performed by HADES. In order to make the comparison with the experimental data, a filter function provided by HADES has been implemented. Simulated data are treated in the same way as experimental one, i.e. dilepton events with opening angle smaller than 9 degree have been rejected and the spectra have been normalized to the mean π^0 multiplicity.

During the experiment different event classes are selected using the 1st level trigger. The 1st level trigger selects on the charged particle multiplicity of the reaction. We have simulated events including an impact parameter selection. Obviously impact parameter cuts have an impact on multiplicities of the hadrons. The $^{12}C+^{12}C$ simulations with impact parameter cut are compared to those in minimum bias. The result is shown in Fig. 2.3 for $^{12}C+^{12}C$ collisions at 2.0 GeV/u. The multiplicity of the produced particles in minimum bias are by 40% suppressed compared to those with an impact parameter cut. In comparison with the TAPS¹ data the minimum bias simulations seems to agree much better with the measured π^0 and η multiplicities (see Table 2.2).

For comparison of the experimental data to the transport model calculations we have simulated events with the corresponding impact parameter cuts. The heavy ion systems measured by HADES passed the respective acceptance filter. The HADES data, measured in collisions of $^{12}C+^{12}C$ 1.0 GeV/u and 2.0 GeV/u, can be found in [P⁺08] and [S⁺09]. The $^{40}Ar+KCl$ system was measured in 40% most central collisions, which corresponds to an impact parameter of $b_{ev} < 3.44$ fm.

¹Two Arm Photon Spectrometer. The π^0 and η multiplicities have been measured by two γ decay channel.

3 e^+e^- pairs from heavy ion collisions measured with HADES

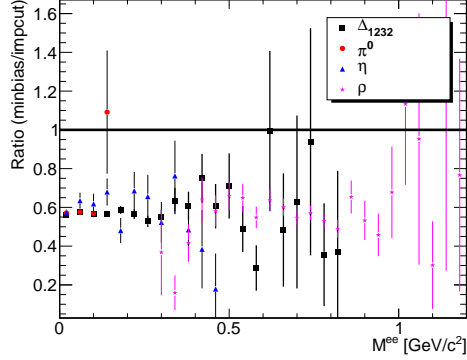


Figure 2.3: Ratio of invariant mass spectra simulated with UrQMD using an impact parameter cut ($b \leq 4\text{fm}$) to the one simulated in minimum bias.

System	Meson	TAPS [mb]	UrQMD [mb]	UrQMD [b_{cut}]
$^{12}\text{C}+^{12}\text{C}$ 1 GeV/u	π^0	0.33	0.38	0.56
	η	0.0018	0.0004	0.0007
$^{12}\text{C}+^{12}\text{C}$ 2 GeV/u	π^0	0.87	0.77	1.35
	η	0.028	0.012	0.021

Table 2.2: π^0 and η multiplicities of TAPS compared with UrQMD in minimum bias [mb] and impact parameter cut [b_{cut}]

Detail information about $^{40}\text{Ar}+KCl$ measurements can be found in [A⁺11].

Figure 2.4 shows the invariant mass spectra of the measured $^{12}\text{C}+^{12}\text{C}$ collisions at 1.0 GeV/u (Fig. 2.4, a) and 2 GeV/u (Fig. 2.4, b) as well as $^{40}\text{Ar}+KCl$ collisions at 1.756 GeV/u (Fig. 2.4, c) compared to the simulated UrQMD cocktail. The invariant mass spectra are normalized by the number of π^0 in full phase space (see Table 2.2). Normalization to the events without collisions (so called "empty" events) are taken in to account as well.

All measured spectra are dominated by the π^0 Dalitz decay for invariant masses smaller than 0.15 GeV/c^2 and agree very well with the simulated data. In $^{12}\text{C}+^{12}\text{C}$ collisions at 1.0 GeV/c^2 a systematic underestimation of the data is observed in the mass region $0.2 < M_{e^+e^-} < 0.4 \text{GeV}/c^2$. It can be attributed to the NN Bremsstrahlung which plays an important role at this beam energy and is not included in this model.

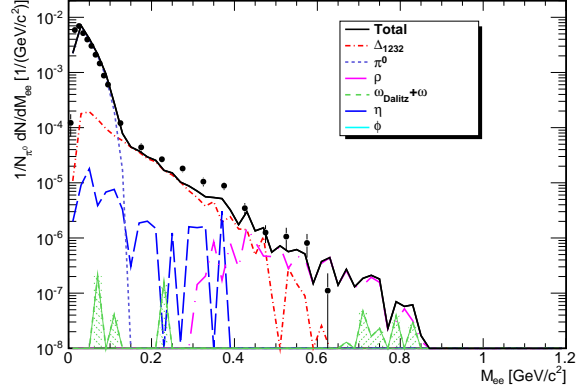
In the case of $^{12}\text{C}+^{12}\text{C}$ at 2.0 GeV/u the $\Delta(1232)$ and η Dalitz decays contribute to the mass region $0.15 < M_{e^+e^-} < 0.55 \text{GeV}/c^2$ with comparable magnitude. However, an overestimation of the data is observed at higher masses. The difference is found in the contribution originating from the direct ρ and ω meson decay, suggesting a probably different value of ρ and ω meson multiplicity.

A similar situation is observed when comparing the $^{40}\text{Ar}+KCl$ data and UrQMD.

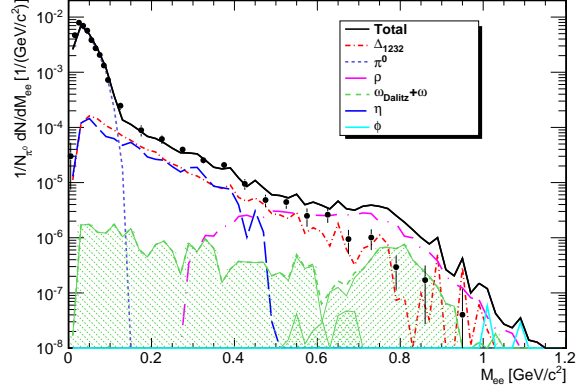
II Comparison of the HADES data with the UrQMD transport model calculations

The $^{40}\text{Ar}+KCl$ simulations show a huge bump around vector meson region which overshoot the HADES data dramatically. On the other hand, the missing e^+e^- yield in the intermediate mass region is clearly visible. It is important to mention here that HADES results demonstrate that the di-electron yield in $^{12}\text{C}+^{12}\text{C}$ collisions can be explained as a superposition of independent NN collisions. On the other hand, a direct comparison of the NN reference spectrum with the e^+e^- invariant mass distribution measured in the heavier system $^{40}\text{Ar}+KCl$ at $1.756\text{ GeV}/u$ shows an excess yield above the reference, which we attribute to radiation from resonance matter. In the next section we would like to investigate this excess e^+e^- pair yield in UrQMD.

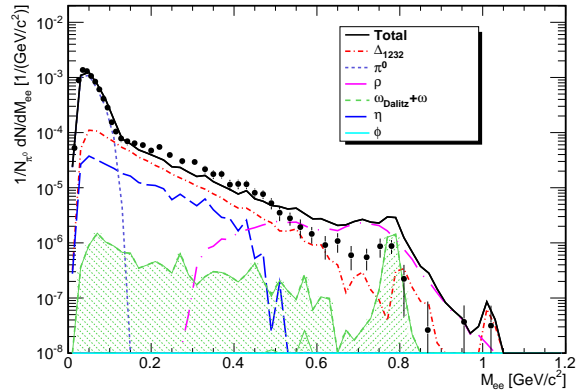
3 e^+e^- pairs from heavy ion collisions measured with HADES



(a) invariant e^+e^- mass spectrum from $^{12}\text{C}+^{12}\text{C}$ collisions at $1.0 \text{ GeV}/u$



(b) invariant e^+e^- mass spectrum from $^{12}\text{C}+^{12}\text{C}$ collisions at $2.0 \text{ GeV}/u$



(c) invariant e^+e^- mass spectrum from $^{40}\text{Ar}+KCl$ collisions at $1.756 \text{ GeV}/u$

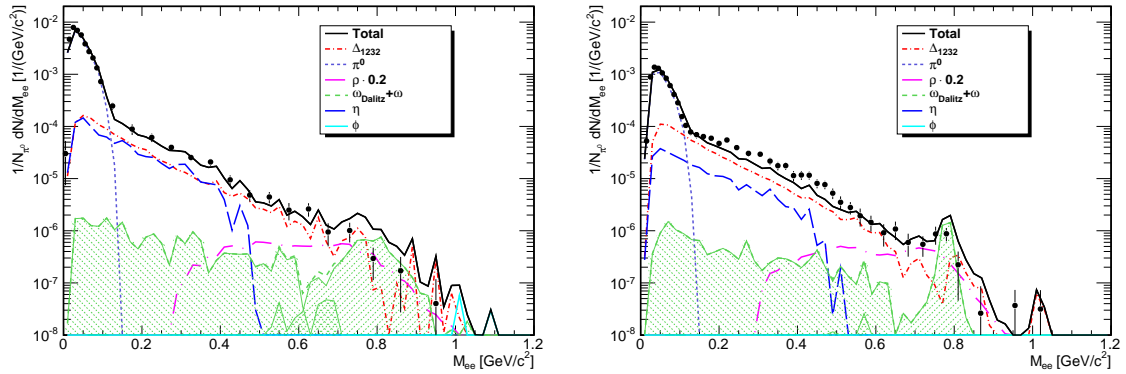
Figure 2.4: UrQMD model calculations for dilepton invariant mass spectra from $^{12}\text{C}+^{12}\text{C}$ (a),(b) and $^{40}\text{Ar}+KCl$ (c) collisions at beam energies of $1.0 \text{ GeV}/u$, $2.0 \text{ GeV}/u$ and $1.76 \text{ GeV}/u$. The calculations were performed with the shining method. The simulated data passed the respective HADES acceptance filter.

4 Vector meson production in UrQMD

In $^{12}\text{C}+^{12}\text{C}$ system at $2.0 \text{ GeV}/u$ and $^{40}\text{Ar}+KCl$ system at $1.756 \text{ GeV}/u$ the contribution of the vector mesons is too large. It is not trivial to model vector meson cross sections in UrQMD. In collisions at beam energies of up to $2.0 \text{ GeV}/u$ the meson production is determined by the excitation of Δ and N^* resonances in reactions $p + p \rightarrow p + N^*$ and $p + p \rightarrow p + \Delta$. However, only poor experimental information is available on the production cross sections of N^* and Δ resonances.

We have tried to scale down the cross section of the ρ meson by a factor of 5. This is a dirty procedure, but it provides a rough idea on how much the ρ meson cross section is overestimated in UrQMD. The result of this scaling is shown in Fig. 2.5 for $^{12}\text{C}+^{12}\text{C}$ $2.0 \text{ GeV}/u$ (left panel) and for $^{40}\text{Ar}+KCl$ $1.756 \text{ GeV}/u$ (right panel). This scaling improves the agreement with the measured data. There are 12 N^* and 7 Δ^* non strange resonances included in UrQMD with non-zero decay branching ratio into the $N\rho$ decay channel. One has to investigate for how much the cross sections of various resonances must be reduced in order to reproduce the experimental data.

For our further analysis it is important to understand on how much such a scaling will influence the mass range $0.15 < M_{e^+e^-} < 0.55 \text{ GeV}/c^2$. This change is never larger than 6%, which shows that a variation of the ρ -meson contribution does not influence the intermediate mass range.



(a) invariant e^+e^- mass spectrum from $^{12}\text{C}+^{12}\text{C}$ collisions at $2.0 \text{ GeV}/u$ (b) invariant e^+e^- mass spectrum from $^{40}\text{Ar}+KCl$ collisions at $1.756 \text{ GeV}/u$

Figure 2.5: UrQMD model calculations for dilepton invariant mass spectra from $^{12}\text{C}+^{12}\text{C}$ (a),(b) and $^{40}\text{Ar}+KCl$ (c) collisions at beam energies of $1.0 \text{ GeV}/u$, $2.0 \text{ GeV}/u$ and $1.76 \text{ GeV}/u$. The calculations were performed with the shining method and the contribution of the ρ meson was scaled down by a factor of 5.

5 Excess e^+e^- pair yield systematics in UrQMD

5.1 Intermediate mass excess in $^{12}C+^{12}C$ and $^{40}Ar+KCl$ collisions

The excess of electron pairs in $^{12}C+^{12}C$ and $^{40}Ar+KCl$ collisions was investigated by the HADES experiment for beam energies of 1.0 and 2.0 GeV/u and 1.756 GeV/u [A⁺11]. Also DLS the experiment has measured $^{12}C+^{12}C$ and $^{40}Ca+^{40}Ca$ collisions at beam energies of 1.0 GeV/u and 2.0 GeV/u . Notice that $^{40}Ar+KCl$ and $^{40}Ca+^{40}Ca$ reaction systems are of a comparable size. Each of the mentioned nuclei contains about 40 nucleons. Figure 2.6 (a) shows the dependence of the integrated excess pair yield above the η in the invariant mass range $0.15 < M_{e^+e^-} < 0.55 GeV/c^2$ on the beam energy and on the system size. The results obtained from DLS and HADES are shown by red and black triangles (connected by dotted lines representing arbitrary down-scaled pion excitation functions) for the medium and light collision systems, respectively. The dilepton data are shown together with the π^0 and η multiplicities obtained with the TAPS photon calorimeter [HAA⁺97a, HAA⁺97b, AHMS03].

Figure 2.6 (b) shows the excess systematic in UrQMD. The excess pair yield I have defined here as a sum of all contributions (mainly $\Delta(1232)$ and ρ) besides the η contribution in the mass range $0.15 < M_{e^+e^-} < 0.55 GeV/c^2$. Please, note that the π^0 multiplicity obtained within the UrQMD model is consistent with the values measured by the TAPS collaboration.

The HADES collaboration shows that the HADES and DLS excess pair yield from $^{12}C+^{12}C$ collisions follow a remarkably similar trend with the increasing beam energy as the mean π^0 multiplicity measured by TAPS. This is also the case for the UrQMD simulations. However, this is not longer true when going to the $^{40}Ar+KCl$ system. At a given bombarding energy the excess pair yield scales with the number of participating nuclei stronger than the π^0 production. The multiplicity of the excess pair measured in $^{12}C+^{12}C$ and $^{40}Ar+KCl$ differs by a factor of 5, while only by factor of 2.7 for the π^0 multiplicities (see Fig. 2.6, a). A similar scaling is found in UrQMD, however the dependence of the excess yield on the system size is found to be not as strong as measured by HADES, i.e. just a factor of 3 (see Fig. 2.6, b). This might be interpreted as a fingerprint of in-medium effects related to multi-step collisions, with baryonic resonances playing an important role.

II Comparison of the HADES data with the UrQMD transport model calculations

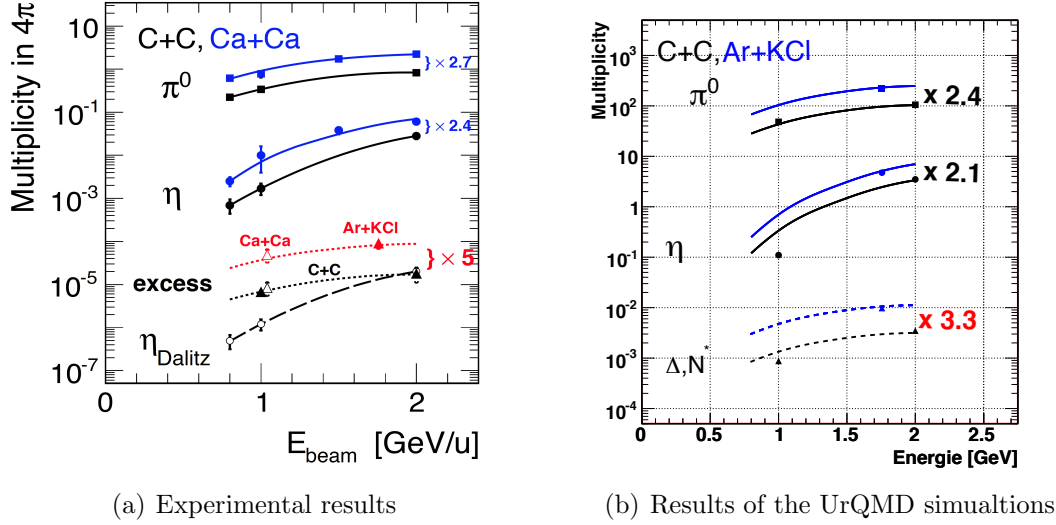


Figure 2.6: Multiplicity of the pair yield above the η Dalitz in the mass range $0.15 < M_{e^+e^-} < 0.55 \text{ GeV}/c^2$ as observed by DLS (open triangles) and HADES (full triangles) as function of beam energy and system size. Dotted lines respect the arbitrarily scaled down π^0 multiplicities from $^{12}\text{C}+^{12}\text{C}$ and $^{40}\text{Ca}+^{40}\text{Ca}$ collisions, respectively. They are meant to illustrate the pion-like beam energy scaling of the dilepton yields. The dashed line is the corresponding η meson contribution in the mass region $0.15 < M_{e^+e^-} < 0.55 \text{ GeV}/c^2$ for the $^{12}\text{C}+^{12}\text{C}$ system. It shows a different energy scale of the production.

Another representation of this result is shown in Fig. 2.7. Here I have normalized each point to the corresponding π^0 multiplicity, just the same as I did with the invariant mass spectra. By doing that I remove to some extent the dependence on the number of participating nuclei. As expected the π^0 multiplicity falls on the same line. Note a different beam energy scaling for the η meson (shown by the dashed line).

The presence of the excess yield is clearly visible here. As it has been mentioned before, it seems that in this energy regime, the excess yield grows with the beam energy like π^0 multiplicity also in case of medium size collision systems. But it scales non-linear with the system size. In the experimental case the e^+e^- enhancement in the mass range $0.15 < M_{e^+e^-} < 0.55 \text{ GeV}/c^2$ was found to be a factor of 2.7, while the enhancement determined from the UrQMD simulations is around 1.5, pointing to an additional source which is not accounted for in the microscopic transport simulations.

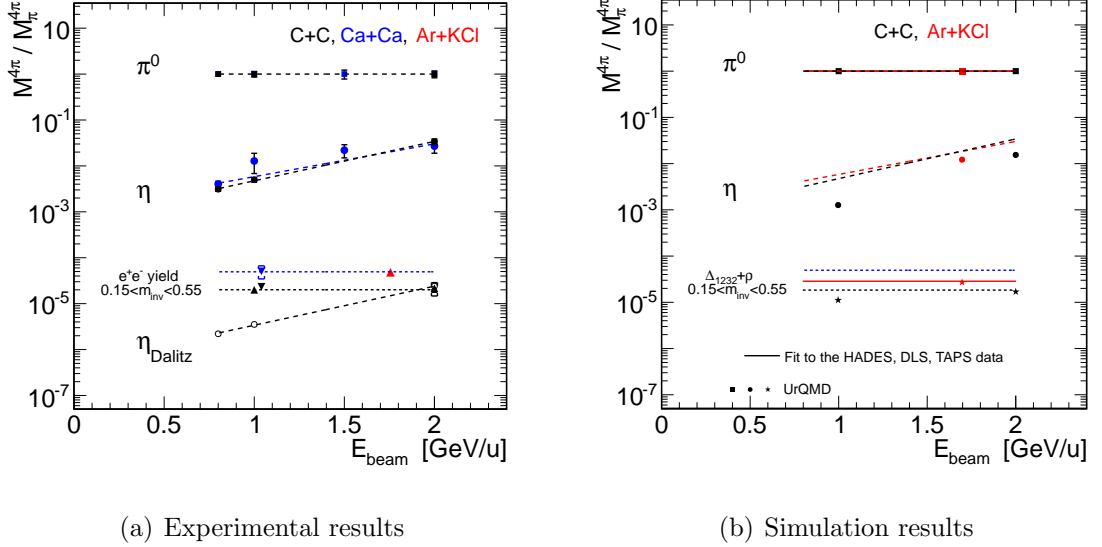


Figure 2.7: Same as Fig. 2.6 but here each point is normalized to the corresponding π^0 multiplicity.

5.2 Behavior of the excess pair yield as function of beam energy and system size

The non-linear scaling of the excess pair yield with the system size needs further, more systematic investigations, in particular by studying larger collision systems. The $^{197}\text{Au}+^{197}\text{Au}$ reaction at $1.25\text{ GeV}/u$ offers the best choice for such studies. In this section the excess pair yield scaling with the beam energy and the system size will be shown.

5.2.1 Nuclear overlap calculation

Before discussing the behavior of the e^+e^- pair yield with the system size I would like to show how the number of participating nuclei have been defined. To do that I have used a nuclear overlap calculation model [CKV82, BBC76, hlm].

The impact parameter is defined as the perpendicular distance from the target nucleus to the initial line of motion of the incident particle. In a central collision the impact parameter is equal to zero. Collisions with an impact parameter larger than 2 times the radius of the nucleus (b_{max}), are called empty events. Here the nuclei pass each other without interaction. In peripheral events the impact parameter is significantly larger than zero, but not larger than b_{max} . Minimum bias events mean that the impact parameter of the collision changes from $b = 0$ to $b = b_{max}$. Table 2.3 summarizes the maximum impact parameters and the corresponding A_{part} for the systems simulated in minimum bias.

II Comparison of the HADES data with the UrQMD transport model calculations

System	A_{part} max	b_{max}
$^{12}C+^{12}C$	$12+12=24$	5.7
$^{40}Ar+KCl$	$40+40=80$	8.6
$^{107}Ag+^{107}Ag$	$107+107=214$	11.85
$^{197}Au+^{197}Au$	$197+197=394$	14.28

Table 2.3: The maximum impact parameters and the corresponding number of participants in different simulated collision systems.

The number of participants (A_{part}) of a collision describes how many nucleons collide. In a central collision all nucleons of the colliding nuclei participate in the reaction.

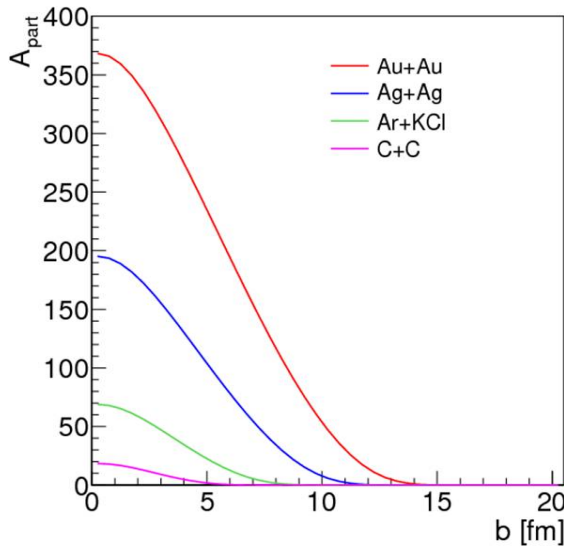


Figure 2.8: Number of participants A_{part} versus the impact parameter b for different systems.

Going to more peripheral collisions some nucleons do not collide with other nucleons. They are called spectators. Obviously the effective number of participants depends on the impact parameter of the collision. This dependence can be calculated with a nuclear overlap model. All calculations are done with an inelastic NN cross section of 30 mb. The nucleus is described with a Wood Saxon density profile. Figure 2.8 shows the distribution of the number of participants as a function of impact parameter for light and heavy systems.

5.2.2 Scaling of the e^+e^- pair yield with the beam energy

To study the dependence the e^+e^- pair yield with the beam energy $^{197}\text{Au}+^{197}\text{Au}$ collisions at 5 different energies, i.e. $1.25\text{ GeV}/u$, $1.5\text{ GeV}/u$, $2.0\text{ GeV}/u$, $4.0\text{ GeV}/u$ and $6.0\text{ GeV}/u$ have been simulated. The total meson multiplicities are summarized in Table 2.4. In Fig. 5.2.2 the e^+e^- multiplicities of the simulated resonances are shown. The π^0 , η and $\Delta(1232)$ multiplicities are normalized to the π^0 multiplicity at a corresponding beam energy. Here the dependence of the η meson multiplicity (red circles) with the beam energy is clearly visible. At a beam energies below $1.5\text{ GeV}/u$ the η meson produced at threshold. At a higher beam energies this dependence decreases.

The excess pair multiplicity scales linearly with the beam energy. The same result has been found already before (see section 5). It is also valid when going even to the higher beam energies.

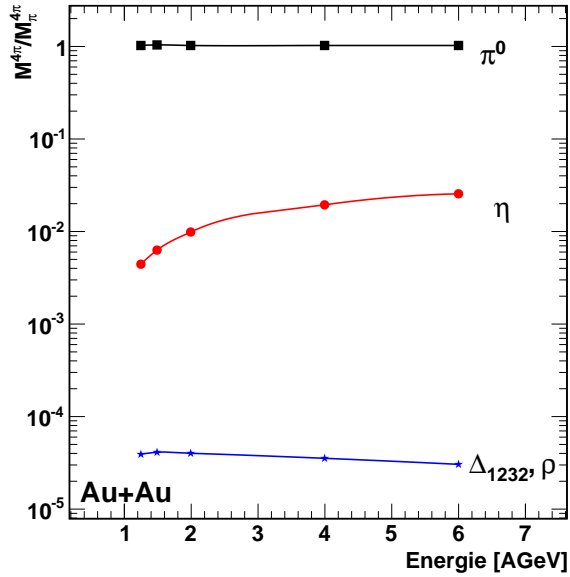


Figure 2.9: e^+e^- multiplicities extracted from $^{197}\text{Au}+^{197}\text{Au}$ collisions at different energies simulated with UrQMD.

II Comparison of the HADES data with the UrQMD transport model calculations

Energy	$M_{e^+e^-}$ [GeV/c^2]	Resonance	Multiplicity
1.25 GeV/u	0 - 1.2	π^0	3.99
	0 - 1.2	η	$1.70 \cdot 10^{-2}$
	0.15 - 0.55	$\Delta(1232)$	$2.45 \cdot 10^{-2}$
	0.15 - 0.55	ρ	$8.42 \cdot 10^{-4}$
	0.15 - 0.55	Excess	$9.88 \cdot 10^{-4}$
1.5 GeV/u	0 - 1.2	π^0	5.81
	0 - 1.2	η	$3.63 \cdot 10^{-2}$
	0.15 - 0.55	$\Delta(1232)$	$3.69 \cdot 10^{-2}$
	0.15 - 0.55	ρ	$1.64 \cdot 10^{-3}$
	0.15 - 0.55	Excess	$1.87 \cdot 10^{-3}$
2.0 GeV/u	0 - 1.2	π^0	7.23
	0 - 1.2	η	$7.06 \cdot 10^{-2}$
	0.15 - 0.55	$\Delta(1232)$	$4.52 \cdot 10^{-2}$
	0.15 - 0.55	ρ	$2.23 \cdot 10^{-3}$
	0.15 - 0.55	Excess	$2.60 \cdot 10^{-3}$
4.0 GeV/u	0 - 1.2	π^0	20.53
	0 - 1.2	η	$3.84 \cdot 10^{-1}$
	0.15 - 0.55	$\Delta(1232)$	$1.12 \cdot 10^{-1}$
	0.15 - 0.55	ρ	$7.84 \cdot 10^{-3}$
	0.15 - 0.55	Excess	$8.51 \cdot 10^{-3}$
6.0 GeV/u	0 - 1.2	π^0	29.58
	0 - 1.2	η	$7.41 \cdot 10^{-1}$
	0.15 - 0.55	$\Delta(1232)$	$1.36 \cdot 10^{-1}$
	0.15 - 0.55	ρ	$1.24 \cdot 10^{-2}$
	0.15 - 0.55	Excess	$1.32 \cdot 10^{-2}$

Table 2.4: Multiplicities of resonances from $^{197}Au+^{197}Au$ collisions at different beam energies.

5.2.3 Scaling of the e^+e^- pair yield with the system size

To study the scaling of the e^+e^- pair yield with the system size $^{12}C+^{12}C$, $^{40}Ar+KCl$, $^{107}Ag+^{107}Ag$ and $^{197}Au+^{197}Au$ collisions at the same beam energy, i.e. 1.25 GeV/u which will be studied by HADES has been simulated. The total multiplicities for the different systems are summarized in Table 2.5. Figure 5.2.3 shows the dependence of meson and baryon multiplicities as a function of the system size. The multiplicities of e^+e^- from the π^0 , η , $\Delta(1232)$ and ρ were extracted for all simulated systems. Further I have normalized π^0 , η , $\Delta(1232)$ and ρ multiplicities to the corresponding one extracted from $^{12}C+^{12}C$ collisions.

I find the behavior of e^+e^- production with the system size very interesting. The multiplicities of the π^0 and η are found to be reduced when A_{part} increases. This might be explained by the time-integrated cross section for the $\Delta(1232)$ reabsorption process ($N\Delta \rightarrow NN$) which in the $^{197}\text{Au}+^{197}\text{Au}$ collisions is larger compared to $^{12}\text{C}+^{12}\text{C}$ collisions. Consequently, the total number of π^0 observed in the final state is up to 50% less in $^{197}\text{Au}+^{197}\text{Au}$ collisions.

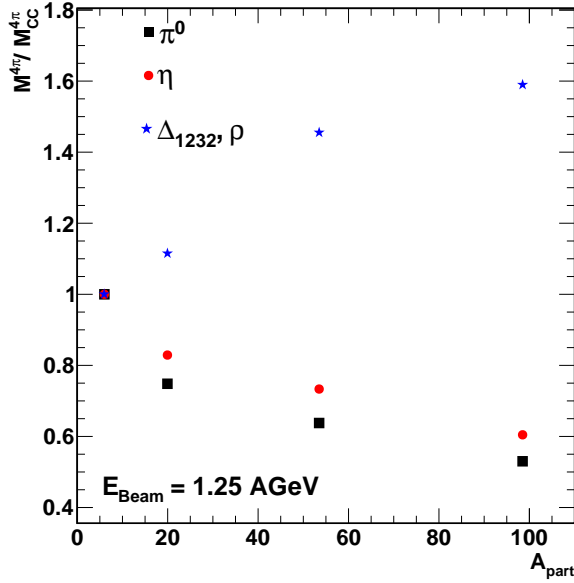


Figure 2.10: e^+e^- multiplicities extracted from $^{12}\text{C}+^{12}\text{C}$, $^{40}\text{Ar}+KCl$, $^{107}\text{Ag}+^{107}\text{Ag}$ and $^{197}\text{Au}+^{197}\text{Au}$ collisions at the same beam energy simulated with UrQMD

The η mesons multiplicities (red dots) are decreasing with the system size by nearly 40%. In contrast, the excess pair yield which is represented by the $\Delta(1232)$ and the ρ in the mass region from 0.15 to 0.55 GeV/c^2 is rising with the system size. From $^{12}\text{C}+^{12}\text{C}$ to $^{197}\text{Au}+^{197}\text{Au}$ the excess is enhanced by around 60%. The ρ and $\Delta(1232)$ multiplicities extracted from the UrQMD simulations in the M_{ee} region from 0.15 - 0.55 GeV/c^2 shows a weak dependence on the beam energy but a stronger scaling with the system size. The HADES collaboration is going to measure $^{197}\text{Au}+^{197}\text{Au}$ collisions at 1.25 GeV/u in the year 2012. In the next chapter further investigations for this system will be discussed.

II Comparison of the HADES data with the UrQMD transport model calculations

System	$M_{ee} [GeV/c^2]$	Resonance	Multiplicity
$^{12}C+^{12}C$ 1.25 GeV/u	0 - 1.2	π^0	0.31
	0 - 1.2	η	$1.16 \cdot 10^{-2}$
	0.15 - 0.55	$\Delta(1232)$	$6.38 \cdot 10^{-4}$
	0.15 - 0.55	ρ	$2.01 \cdot 10^{-5}$
	0.15 - 0.55	Excess	$2.38 \cdot 10^{-5}$
$^{40}Ar+KCl$ 1.25 GeV/u	0 - 1.2	π^0	1.01
	0 - 1.2	η	$4.15 \cdot 10^{-3}$
	0.15 - 0.55	$\Delta(1232)$	$3.06 \cdot 10^{-3}$
	0.15 - 0.55	ρ	$1.08 \cdot 10^{-4}$
	0.15 - 0.55	Excess	$1.26 \cdot 10^{-4}$
$^{107}Ag+^{107}Ag$ 1.25 GeV/u	0 - 1.2	π^0	2.60
	0 - 1.2	η	$1.12 \cdot 10^{-2}$
	0.15 - 0.55	$\Delta(1232)$	$1.21 \cdot 10^{-2}$
	0.15 - 0.55	ρ	$4.24 \cdot 10^{-4}$
	0.15 - 0.55	Excess	$4.97 \cdot 10^{-4}$
$^{197}Au+^{197}Au$ 1.25 GeV/u	0 - 1.2	π^0	3.99
	0 - 1.2	η	$1.70 \cdot 10^{-2}$
	0.15 - 0.55	$\Delta(1232)$	$2.45 \cdot 10^{-2}$
	0.15 - 0.55	ρ	$8.42 \cdot 10^{-4}$
	0.15 - 0.55	Excess	$9.88 \cdot 10^{-4}$

Table 2.5: Meson multiplicities extracted from $^{12}C+^{12}C$, $^{40}Ar+KCl$, $^{107}Ag+^{107}Ag$ and $^{197}Au+^{197}Au$ collisions at $E_{beam} = 1.25$ GeV/u

5.3 Trigger considerations

In experiment there are two 1st level trigger settings under the consideration, i.e. minimum bias and a 30% of the most central collisions which will be selected based on a multiplicity measurement in the Time-of-Flight walls. The minimum bias trigger will be used to select peripheral collisions. It would be nice if we can use a minimum bias trigger and try to compare with the superposition of the pp and pn reactions already measured at the same beam energy by HADES. It is not trivial task, since there might be a lot of background reactions on the beam detector materials. Another possibility might be a measurement of $^{12}C+^{12}C$ collisions at 1.25 GeV/u. On the other hand, comparison of $^{40}Ar+KCl$ collisions with $^{197}Au+^{197}Au$ collision is possible. This is an important task. Therefore it is necessary to understand which centrality region should be chosen for the $^{197}Au+^{197}Au$ collisions. The simulated lepton pairs were calculated for different impact parameter steps. The size of one step is 3 fm. As it has been mentioned before, the $^{40}Ar+KCl$ data were taken for the $b < 3.44$ fm. From the nuclear overlap model the average number of participants to be equal to 50 has been extracted.

Impact Parameter	Number of
0-3 fm	340.8
3-6 fm	252.8
6-9 fm	136.7
9-12 fm	47.7
12-15 fm	6.2

Table 2.6: Mean number of participants in $^{197}\text{Au}+^{197}\text{Au}$ collisions in different impact parameter regions.

Table 5.3 shows the results from nuclear overlap calculations for different impact parameters of $^{197}\text{Au}+^{197}\text{Au}$ collisions. Fig. 2.11 shows the comparison of various e^+e^- sources extracted from $^{40}\text{Ar}+KCl$ collisions ($b < 3.44$ fm) and from $^{197}\text{Au}+^{197}\text{Au}$ collisions for 5 impact parameter steps. One can see that spectra of e^+e^- pairs from π^0 Dalitz decays are comparable, when impact parameter of 9 - 12 fm for $^{197}\text{Au}+^{197}\text{Au}$ collisions is selected. This corresponds to the average number of participants of about 48. The η shows a similar behavior like those from the π^0 . The short lived resonances like $\Delta(1232)$ (see Fig. 2.11, upper left panel) and ρ (see Fig. 2.11, lower left panel) show a completely different behavior. They can be described with more central $^{197}\text{Au}+^{197}\text{Au}$ collisions, i.e. $3 < b < 6$ fm. This gives a hint that phases with higher density has been realized in course of central $^{40}\text{Ar}+KCl$ collision compared to the peripheral $^{197}\text{Au}+^{197}\text{Au}$ collisions. It would be interesting to access and check this scenario with experimental data.

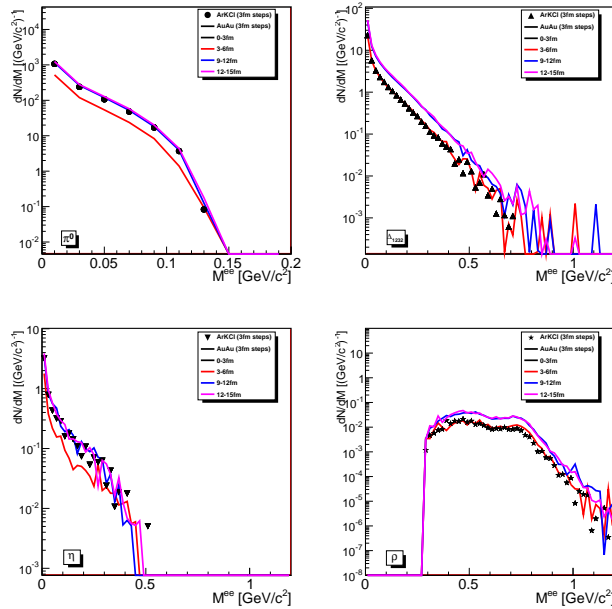


Figure 2.11: e^+e^- invariant mass spectra of different particles. Different impact parameter regions from $^{197}\text{Au}+^{197}\text{Au}$ (lines) in comparison to central $^{40}\text{Ar}+KCl$ with $b \leq 3.44$ fm (points) Upper Left: π^0 Dalitz, upper right: $\Delta(1232)$ Dalitz decays, lower left: η Dalitz decays, lower right: $\rho \rightarrow e^+e^-$ decay.

II Comparison of the HADES data with the UrQMD transport model calculations

Part III

Modeling of the dense phase in $^{197}\text{Au}+^{197}\text{Au}$ collisions

*There is only one difference
between a madman and me.
I am not mad.*

Salvador Dali

As we have learned from Part II in $^{197}\text{Au}+^{197}\text{Au}$ collisions at $1.25\text{ GeV}/u$ a large e^+e^- pair yield comes from the emission density region which is factor of 2 larger compared to the normal nuclear matter density. Since UrQMD uses only vacuum spectral functions the predictions for e^+e^- radiation from high density stages of the heavy ion collision can be refined.

In the SPS energy regime thermal model like from [RWvH09] is able to describe the measured NA60 data [D⁺07], which also show clear medium effects. A description of heavy ion collisions with a thermal model seems to be a good method to model e^+e^- production from the dense stage of the heavy ion collision.

6 Invariant mass spectra

The invariant mass spectra reconstructed from the minimum bias $^{197}\text{Au}+^{197}\text{Au}$ collisions at a beam energy of $1.25\text{ GeV}/u$ is shown in Fig. 3.1. The integrated multiplicities are shown in Table 2.4.

To determine dense and diluted phases of the heavy ion collision the invariant mass spectra is studied. The dileptons are divided into two categories, i.e. these which are emitted at a low density ($\rho/\rho_0 < 1$) and a high density region ($\rho/\rho_0 > 1$) and filled in two different invariant mass spectra. Both invariant mass spectra are shown in Fig. 3.2. The total multiplicities from both density regions are summarized in Table 3.1

Only 20% of the e^+e^- from π^0 came from the dense stages of the collisions, which makes π^0 unprofitable as observable for dense stages. For η decay no significant dependence on the density is visible.

III Modeling of the dense phase in $^{197}\text{Au}+^{197}\text{Au}$ collisions

The ω Dalitz and the ω direct decays are effected by the medium. 75% of the pairs are emitted in the dense phases of the collision, but since the lifetime of the ω is long (23 fm/c) less dileptons decay inside the fireball which has a livetime of about 10 fm/c. Short lived resonances $\Delta(1232)$ and ρ mainly decay inside dense phase. They seem to be good candidates for probing dense matter.

Resonance	$\rho/\rho_0 > 1$	$\rho/\rho_0 < 1$	from the dense phase (%)
$\Delta(1232)$	$8.3 \cdot 10^{-2}$	$2.0 \cdot 10^{-2}$	80 %
π^0	0.44	1.5	20 %
η	$3.8 \cdot 10^{-3}$	$4.2 \cdot 10^{-3}$	46%
ω	$2.6 \cdot 10^{-4}$	$8.2 \cdot 10^{-5}$	75%
ρ	$6.1 \cdot 10^{-4}$	$1.3 \cdot 10^{-4}$	85%
ϕ	$9.9 \cdot 10^{-7}$	$1.1 \cdot 10^{-7}$	90%
Excess	$6.4 \cdot 10^{-5}$	$1.3 \cdot 10^{-5}$	83%

Table 3.1: Decay multiplicities of resonances in $^{197}\text{Au}+^{197}\text{Au}$ collisions in dense ($\rho/\rho_0 > 1$) and diluted ($\rho/\rho_0 < 1$) phases. The last column shows the fraction of the total emitted dileptons stemming from the dense phase.

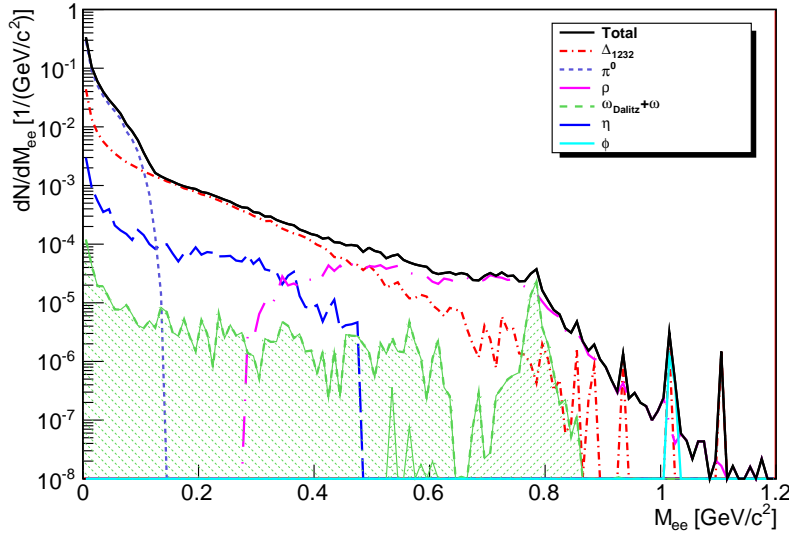


Figure 3.1: e^+e^- invariant mass spectrum from the $^{197}\text{Au}+^{197}\text{Au}$ collisions at 1.25 GeV/u simulated UrQMD cocktail.

6 Invariant mass spectra

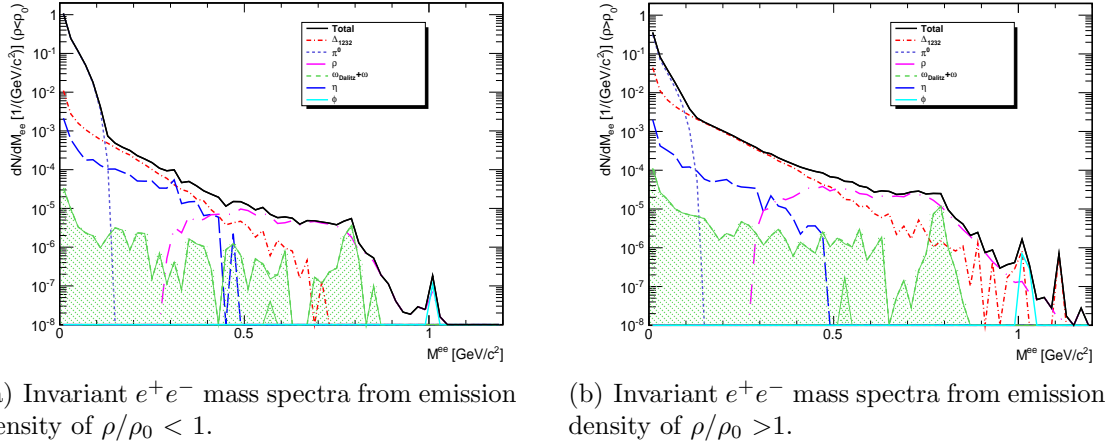


Figure 3.2: Invariant e^+e^- mass spectra from the $^{197}Au+^{197}Au$ collisions at 1.25 GeV/u at various regions of the emission density

A closer look to that behavior of the ρ meson spectral shape for at different values of the density at which e^+e^- were radiated (later called "emission density") for different systems at 1.25 GeV/u will be discussed now. Figure 3.3 illustrates the normalized emission density (ρ_0 is a normal nuclear matter density and equals to $1.7 fm^{-3}$) versus the e^+e^- emission time for different systems ranging from the light $^{12}C+^{12}C$ to heavy $^{197}Au+^{197}Au$. While in $^{12}C+^{12}C$ collisions most of the dileptons come from a density which is equal to the normal nuclear matter density, in $^{40}Ar+KCl$ and $^{197}Au+^{197}Au$ collisions most of the lepton pairs coming from the stages of the heavy ion collision where the density is more than 1.5 times larger than the normal nuclear matter density.

I have divide my events into 3 samples characterized by in the different emission density and plotted the invariant e^+e^- mass distribution of the ρ meson for each of the selected samples. In Fig. 3.4 the invariant mass spectra from the ρ meson for different emission densities in the respective system are shown. The invariant e^+e^- mass spectra distinguish between dileptons from emission densities smaller than a normal nuclear matter (black circles), those from 1 to 1.5 times nuclear matter density (red circles) and those with higher than 1.5 normal nuclear matter density (green circles).

In $^{197}Au+^{197}Au$ collisions the dominant part of e^+e^- from ρ meson comes from the density region. However, the UrQMD transport model do not include correct description of the electron pair radiation from the dense phase of the collision. To do that one could apply a thermal model.

III Modeling of the dense phase in $^{197}\text{Au}+^{197}\text{Au}$ collisions

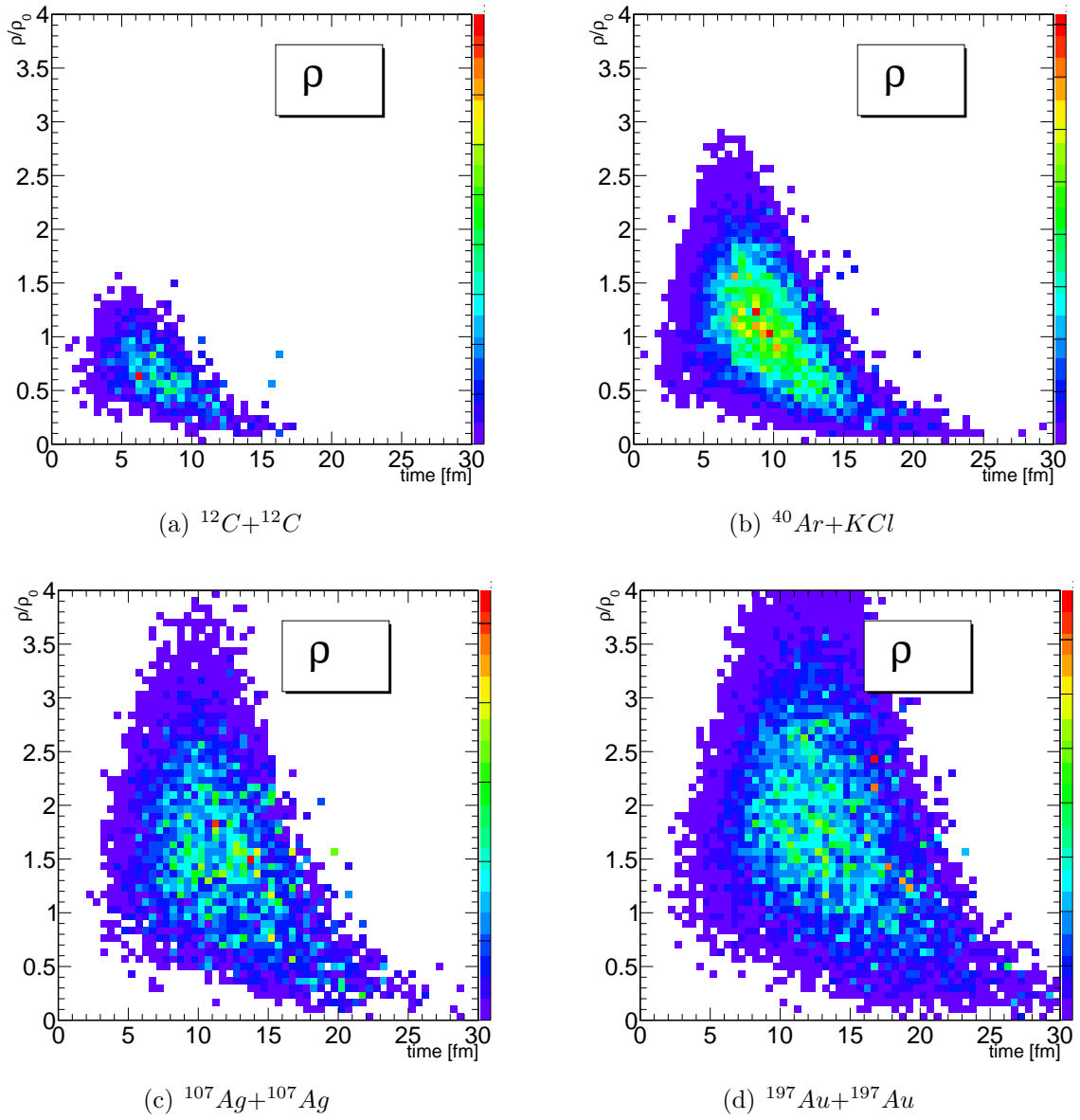
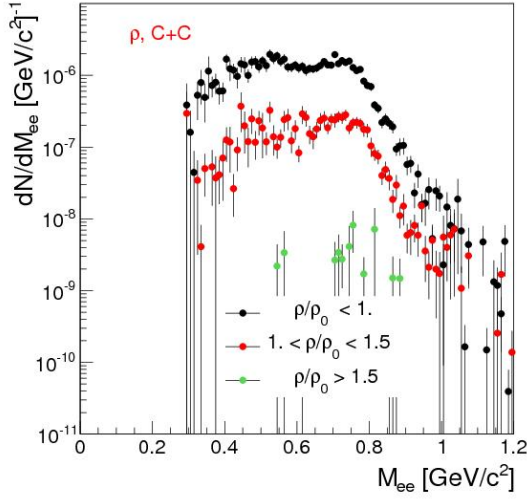
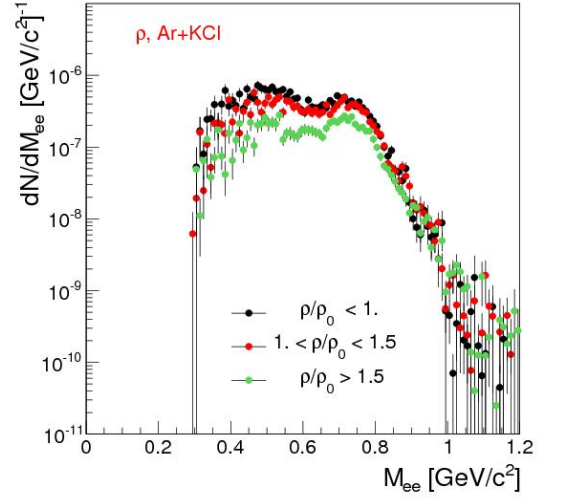


Figure 3.3: Emission time of dileptons versus emission density for different systems at $1.25 \text{ GeV}/u$

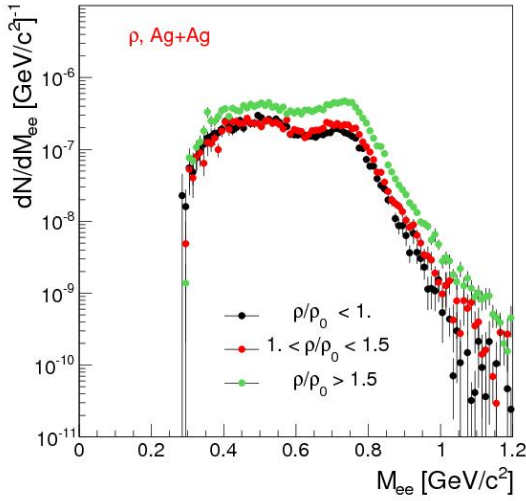
6 Invariant mass spectra



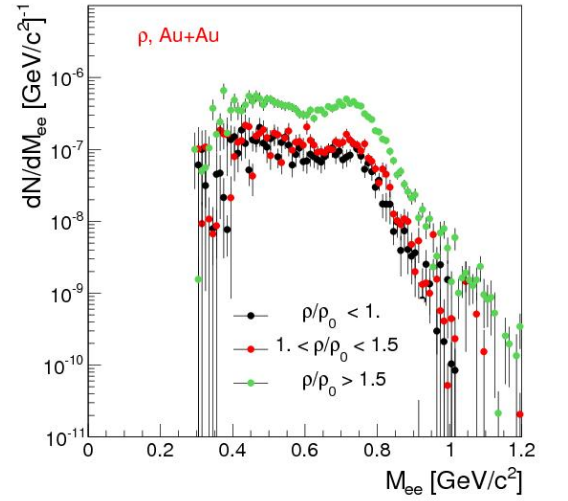
(a) $^{12}\text{C}+^{12}\text{C}$



(b) $^{40}\text{Ar}+^{39}\text{KCl}$



(c) $^{107}\text{Ag}+^{107}\text{Ag}$



(d) $^{197}\text{Au}+^{197}\text{Au}$

Figure 3.4: Invariant mass spectra of the ρ meson extracted from various collision systems and for the different values of the emission density.

7 Determination of the inverse-slope parameter (T_{eff})

The momentum distribution of particles emitted from thermalized system can be approximated with a Boltzmann function:

$$\frac{1}{m_t^2} \frac{d^2 N}{d(m_t - m_0) dy_{cm}} = A \cdot \exp\left(\frac{-(m_t - m_0)}{T_{eff}}\right), \quad (7)$$

in a certain rapidity range dy_{cm} . The integration constant A and the inverse-slope parameter T_{eff} depends on the rapidity.

Theoretical models like [Hag84] assume a local thermal equilibrium as explanation for that behavior. Changes of m_t slope linked to changes of the temperature of the dilepton source.

Using a fit with two temperature components one could describe for example a pion m_t spectra [A⁺11]. It is possible to interpret particles at low m_t as products from resonances and those with higher m_t as direct produced particles.

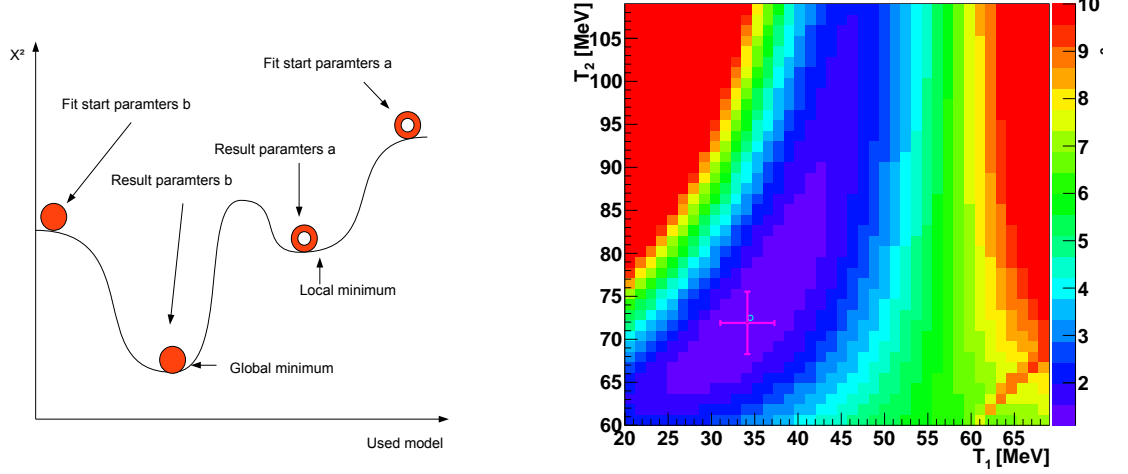
The m_t spectra are fitted with the following function:

$$y = A_1 \cdot \left(\exp\left(\frac{-m_T}{T_1}\right) + A_2 \cdot \exp\left(\frac{-m_T}{T_2}\right) \right) \quad (8)$$

The realization of Boltzmann fits is done with a gradient descent, which is a first-order optimization algorithm. To find a local minimum the minimization procedure takes steps proportional to the negative of the gradient (or of the approximate gradient) of the function at the current point [Sny05].

The gradient descent method is fast, but can fail to produce the optimal solution. Since this method just find local minima it is important to choose the correct start parameters. Fig. 3.5 (a) illustrates this problem schematically. Choosing the first parameters a the solution of the fit will be a local but not a global minimum.

7 Determination of the inverse-slope parameter (T_{eff})



(a) schematic view of a non optimal solution of a minimization problem with a greedy algorithm.

(b) T_1 versus T_2 versus χ^2/NDF . The absolute minimum with T_1^* and T_2^* is marked with a cyan circle. The fit with T_1^* and T_2^* as start parameters is shown with the magenta marker

Figure 3.5: Problem and solution of a fit with gradient descent.

To avoid that the fits end up in a local minimum, the analysis of the m_t spectra is done in the following steps:

- Fix T_1 and combine it with all possible T_2
- Chose next T_1 repeat the first step
- Extract χ^2/NDF from each combination of T_1 and T_2
- Find the absolute minimum χ^2/NDF^2 , and the associated temperatures T_1^* and T_2^*
- Set the start parameters to T_1^* and T_2^* and fit again
- Crosscheck and extraction of the error bars from the final "best" fit

In this thesis this fit method will be called " χ^2 minimization method". Per definition T_1 is set to the lower temperature, therefore the condition $T_1 < T_2$ must be valid each time. A possible result is shown in Fig. 3.5 (b).

²NDF are the degrees of Freedom for the fit

8 Inverse-slope parameters at different rapidity bins

In this section the inverse-slope parameters determination will be discussed. The method described in section 7 is validated with the $^{40}\text{Ar}+KCl$ measurements of HADES, and applied to extract the T_{eff} for the $^{197}\text{Au}+^{197}\text{Au}$ collisions.

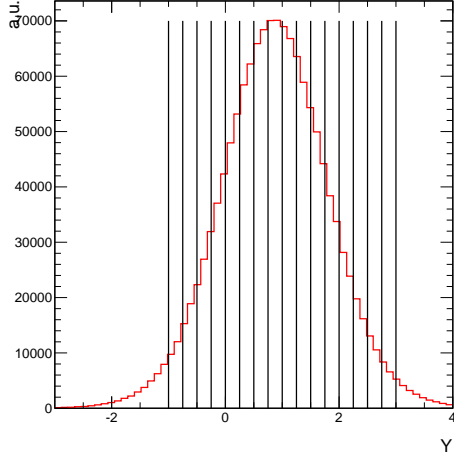
8.1 Inverse-slope parameters from $^{40}\text{Ar}+KCl$ at $1.756\text{ GeV}/u$

In Fig. 3.6 (a) the rapidity distribution of the e^+e^- pairs from π^0 Dalitz decay produced in $^{40}\text{Ar}+KCl$ collisions at a beam energy of $1.756\text{ GeV}/u$ is shown. A Gaussian fit of this distribution gives a mid rapidity of 0.87 with a σ of 0.94. This is identical with the measured distribution. Here the m_t distribution was analyzed for 16 different rapidity bins from $Y=-1$ to $Y=3$.

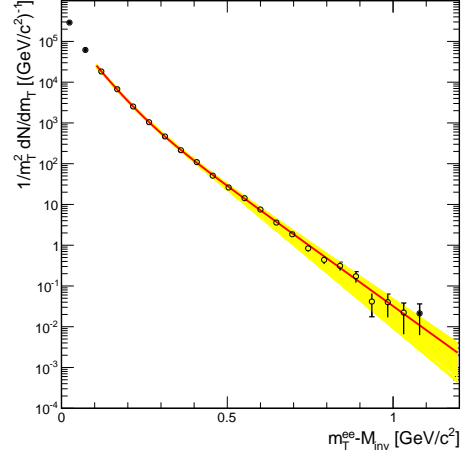
Using the χ^2 minimization method the slope of each rapidity bin is extracted. Here 30 times 30 fits for each bin with a slope step T of 2 MeV are realized. The minimum value of the slope is set to 1 for T_1 and 20 for T_2 . The χ^2 minimization method scans from 1 to 61 MeV (T_1) respectively 20 to 60 MeV (T_2)

In Fig. 3.6 (a) the m_t spectrum at mid-rapidity is shown (the m_t spectra of each rapidity bin, ordered by increasing rapidity can be find in Appendix B, Fig. A 5) It is fitted in the m_t range from $0.1\text{ GeV}/c^2$ to $1.2\text{ GeV}/c^2$. As it has been mentioned before, the fit procedure is iterative. Fits with a χ^2 value lower then 10 are shown with yellow lines (see Fig. 3.6, b). In Fig. 3.6 (d) the 2 dimensional histogram of the χ^2/NDF for each combination of T_1 and T_2 is shown. The absolute minimum (Final values of T_1 and T_2) and the fit with T_1^* and T_2^* as free start parameters are indicated with green open circles and magenta open squared respectively (the T_1 versus T_2 versus χ^2/NDF spectra of each rapidity bin, ordered by increasing rapidity can be find in Appendix B, Fig. A 6) The extracted temperatures are summarized in Appendix B, Table A 2 and shown in Fig. 3.7 (c). Like it's expected from measurements the highest temperatures are reached at mid rapidity. The lower temperature T_1 ranges from 20 ± 2 to 40 ± 1 MeV. T_2 ranges from 40 ± 2 to 78 ± 1 MeV. Comparing to the results of HADES the higher temperature shows a difference on the level of 10 - 15 MeV.

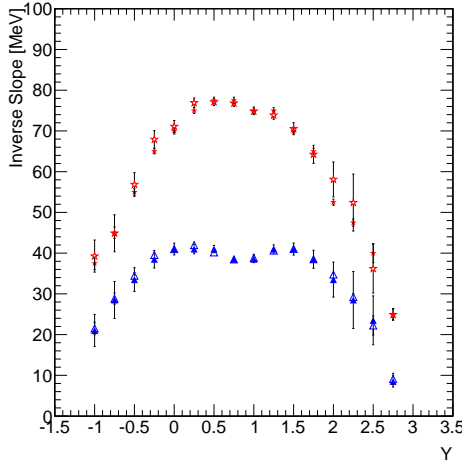
8 Inverse-slope parameters at different rapidity bins



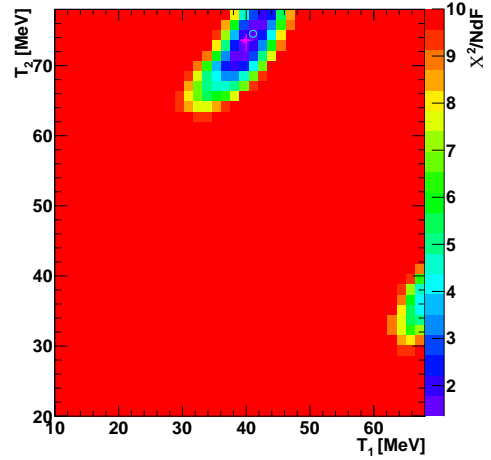
(a) Rapidity distribution. Shown are the chosen rapidity slices from the projection of the $m_t - m_{inv}$ spectra.



(b) $m_t - m_{inv}$ at midrapidity



(c) Extracted temperatures versus rapidity

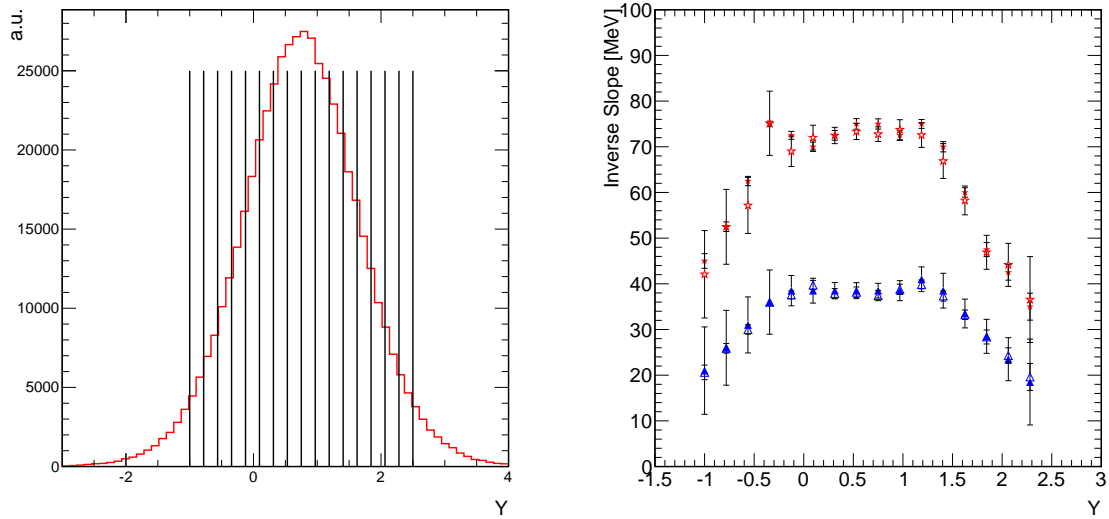


(d) Results of the χ^2 minimization method at midrapidity

Figure 3.6: Example of an effective slope parameters extraction with the χ^2 minimization method. The rapidity distribution (red curve) is shown in (a). The $m_t - m_{inv}$ spectrum (b) is depicted together with all fits of with a $\chi^2 < 10$ (yellow band) and the fits with the final parameters (red curve). Panel (d) shows the T_1 versus T_2 versus χ^2 distribution, and in (c) the extracted temperatures

8.2 Inverse-slope parameters from $^{197}\text{Au}+^{197}\text{Au}$ at 1.25 GeV/u

Like in section 8.1 the m_t slopes of the dileptons from π^0 Dalitz decay are extracted with the χ^2 minimization method. In Fig. 3.7 (a) the rapidity distribution is shown. A Gaussian fit gives a mid rapidity of 0.75 with a σ of 0.92. The rapidity distribution is, in the range from -1 to 2.5, divided into 16 bins. Fit parameters are identical with the ones from section 8.1. The extracted temperatures are sum-



(a) Rapidity distribution. Shown are the chosen rapidity slices from the projection of the $m_t - m_{inv}$ spectra.

(b) Extracted T_1 (blue triangles) and T_2 (red stars) from $m_t - m_{inv}$ distribution versus rapidity.

Figure 3.7: Rapidity distribution and extracted temperatures of an UrQMD simulation of $^{197}\text{Au}+^{197}\text{Au}$ collisions at 1.25 GeV/u.

marized in Appendix B, Table A 3 and shown in Fig. 3.7 (b). Again the highest temperatures are reached at mid rapidity. The lower temperature T_1 ranges from 20 to 38 MeV. T_2 ranges from 36 to 72 MeV. The fitted m_t spectra and the T_1 versus T_2 versus χ^2 distribution are depicted in Appendix B, Fig. A 8 and Fig. A 7. It should be noted that the temperatures vary by about 40 MeV over the full range. The following analysis was carried out for integrated rapidity. In the future it might be important to include the rapidity dependence to the analysis.

9 Inverse-slope parameters for different time steps of the heavy ion collision

The time and the emission density evolution of the different particles is shown in Fig. 3.8. The figure depicts at which time and from which density of the collision the dileptons are emitted.

The π^0 meson decays (Fig. 3.8, a) emitted at low densities and mainly at late stages of the collision. The η (Fig. 3.8, b) decays nearly homogeneously throughout the full evolution of the collision. The shape of the distribution is similar to the one of the π^0 decay, but has no significant peak at late time.

The $\Delta(1232)$ decay (Fig. 3.8, c) is distributed over the whole time evolution and prominent at all density regions. But dileptons from this decay originate from the dense phase ($\rho/\rho_0 > 1.5$) and a certain time region from 7-14 fm. The time evolution of the ρ meson (Fig. 3.8 (d)) is similar to that of the $\Delta(1232)$.

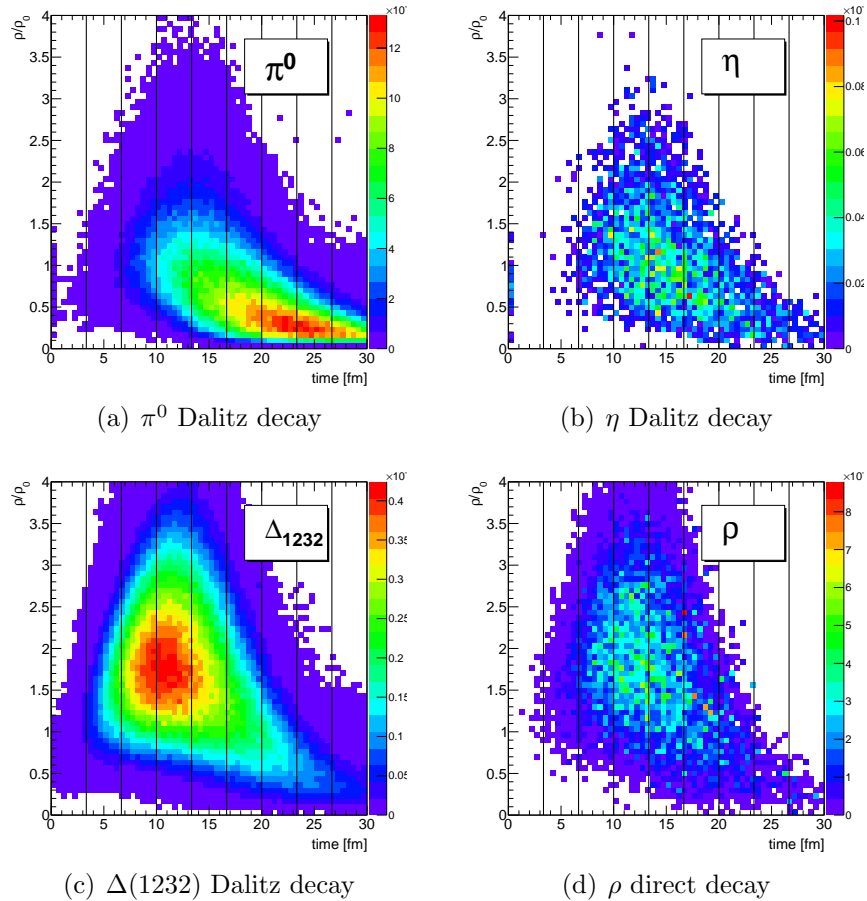


Figure 3.8: Time and density where dileptons from different sources of $^{197}\text{Au}+^{197}\text{Au}$ collisions at $1.25\text{ GeV}/u$ are produced.

III Modeling of the dense phase in $^{197}\text{Au}+^{197}\text{Au}$ collisions

The evolution for a given meson is divided into 9 time steps. Each time step is analyzed with the χ^2 minimization method, and for each time step a density profile is extracted. An example of an emission density distributions is depicted in Fig. 3.9 (a). The maximum bin is used as extracted density and the root mean squared of the distribution is used as width.

The density distributions for the all time steps of dilepton sources are given in the Appendix C (see Figure A 9 for π^0 , Fig. A 12 for η , Fig. A 15 for $\Delta(1232)$ and Fig. A 18 for ρ).

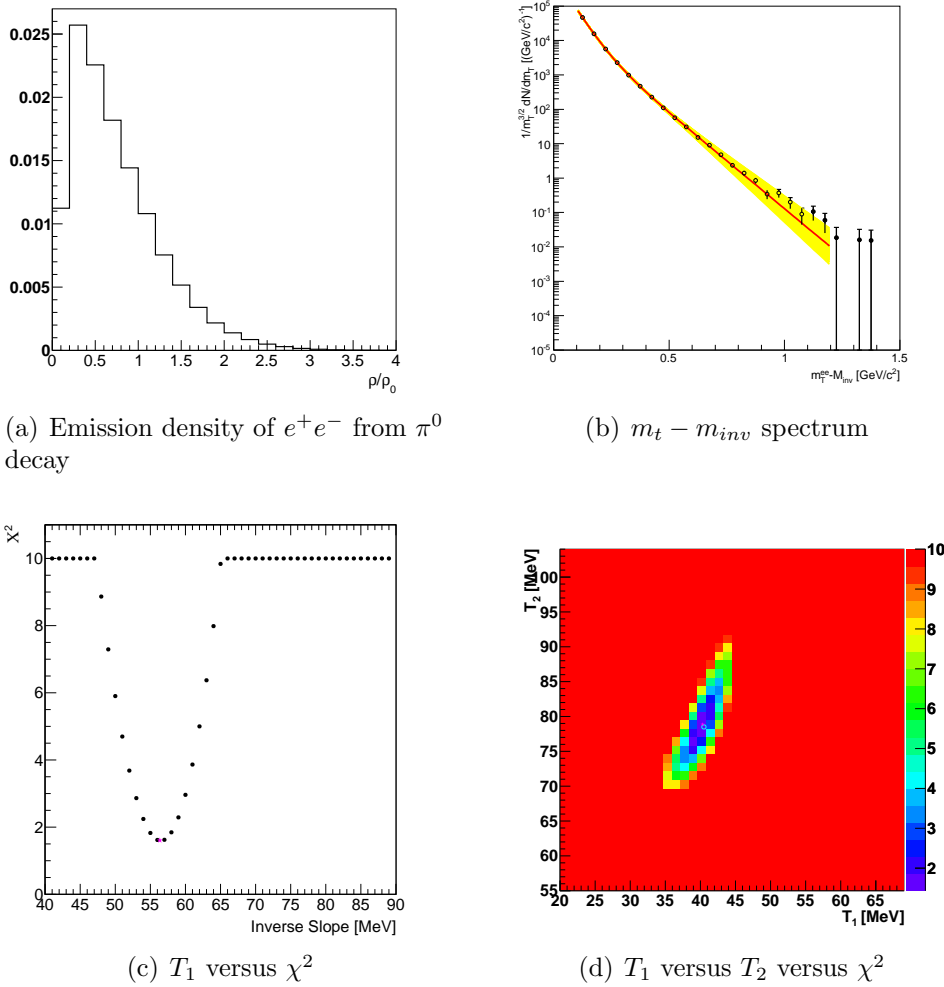


Figure 3.9: Example of the effective slope parameter extraction with the χ^2 minimization method. The emission density (a) is given by the maximum bin and the RMS of the distribution. The $m_t - m_{inv}$ spectrum is depicted together with all fits with a $\chi^2 < 10$ (yellow bend) and the fit with the final parameters (red curve). The other figures show the χ^2 minimization for two (c) and for one (d) temperature.

9 Inverse-slope parameters for different time steps of the heavy ion collision

The $m_t - m_{inv}$ spectrum (like in Fig. 3.9, b) of π^0 is analyzed, analog to the analysis of different rapidity bins, with a two temperature fit function (see Fig. 3.9, c).

The $m_t - m_{inv}$ spectra from all time steps of the different dileptons are shown in the Appendix C (see Fig. A 10 for π^0 , Fig. A 13 for η , Fig. A 16 for $\Delta(1232)$ and Fig. A 19 for ρ)

The distributions of η , $\Delta(1232)$ and ρ decays are not fitted with a two temperature fit, since the extracted χ^2 for the fits are significant larger than those of the fit for π^0 when using fit function (8). The slopes are extracted with a single temperature fit. The fit function is given by:

$$y = A_1 \cdot \exp\left(\frac{-m_T}{T_1}\right) \quad (9)$$

Again the best (minimum) χ^2 value is used as start parameter for a refit. The refit results are marked with a magenta star in the distributions. A typical result is given in Fig 3.9, d.

Dileptons from	Fit	Fit region [GeV/c ²]	T _{min} [MeV]
π^0	T1,T2	0.1-1.2	20
			55
η	T1	0.2-1.2	50
$\Delta(1232)$	T1	0.3-1.2	40
ρ	T1	0.0-1.2	40

Table 3.2: The selected fit regions and start values of T_1 and T_2

The step size of each χ^2 minimization is 1 MeV and for each particle 50 fits are carried out. The minimum temperature value is chosen by hand for computing time reasons. With the T_{min} values from Table 9 the χ^2 minimization method is able to find a minimum with 50 steps. The resulting χ^2 versus temperature distributions for all time bins of the dilepton sources are depicted in the Appendix C (see, Fig. A 11 for π^0 , Fig. A 14 for η , Fig. A 17 for $\Delta(1232)$ and Fig. A 20 for ρ).

III Modeling of the dense phase in $^{197}\text{Au}+^{197}\text{Au}$ collisions

A time dependence of effective slope parameters and emission density is shown in Fig. 3.10. For each hadron the temperature (black stars) and the density of the maximum decay probability of the dilepton sources (red squares) for the given time step is shown. Tables A 4 (π^0), A 5 (η), A 6 ($\Delta(1232)$) and A 7 (ρ) summarize the extracted temperatures, densities and the related errors. Here always the results of the refit and the error are given.

Dileptons from π^0 decay (Fig. 3.10 (a)) are emitted at temperatures from 35 to 45 MeV for T_1 and 70 to 80 MeV for T_2 . Both temperatures show a slight rise to later stages of the collision. However, the late stages suffer from statistics especially for the higher temperature (T_2) (see Fig. A 10). This is also visible in the χ^2 minimization plot (Fig. A 11) where a large area for possible χ^2 occurs. The decreasing of temperature T_2 could be a hint to freeze out effects. The dileptons from π^0 decays are emitted from dilute stages. The maximum decay rate is reached at max 1.2 times normal nuclear matter density early stages of the collision.

From the $m_t - m_{inv}$ spectrum (Fig. A 13) of the $\eta \rightarrow \gamma e^+e^-$ decay temperatures from 50-90 MeV are extracted. Due to little statistics the χ^2 minimization method gives a large amount of results, with similar χ^2 values. In Fig. A 14 broad minimum regions shows that the best fit is reached but still other solutions with small χ^2 are possible. The large errors in Fig. 3.10 (b) indicated that, too. The maximum density where η mesons decay is 1.4 time normal nuclear matter density.

$\Delta(1232)$ Dalitz decays inside the dense phases, with ρ/ρ_0 up to 1.9 times normal nuclear matter density (Fig. 3.10 (c)). From the $m_t - m_{inv}$ spectra (Fig. A 16) temperatures from 48 to 78 MeV with small errors are extracted. The χ^2 minimization (Fig. A 17) shows clear minima.

Like dileptons from $\Delta(1232)$ Dalitz decay the e^+e^- pairs from ρ decay (Fig. 3.10 (d)) originate from phases of high densities of the heavy ion collision. Here the density of 1.9 times normal nuclear matter density where ρ mesons decay to e^+e^- pairs is reached. Due to less statistics the errors of the extracted temperatures are larger than for $\Delta(1232)$. They show a significant rise from 40 to 80 MeV at an early stage of the collision.

Please note, large contributions of e^+e^- from $\Delta(1232)$ and ρ decays occur at ρ/ρ_0 higher than 3. Also the extracted slope parameters at the late stage of the heavy ion collision is the same for all sources i.e. $T_{eff} \approx 60$ MeV.

9 Inverse-slope parameters for different time steps of the heavy ion collision

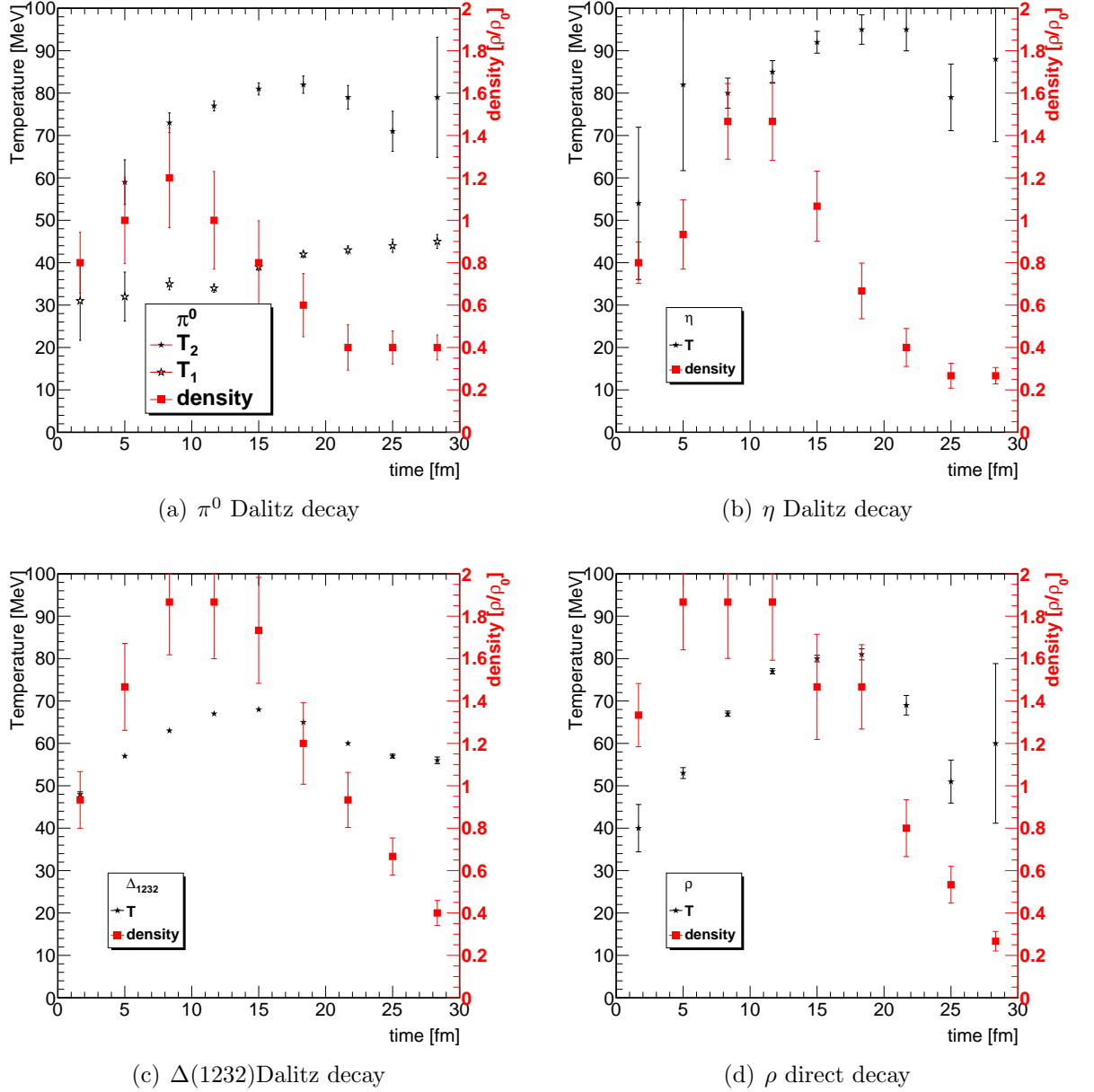


Figure 3.10: Emission temperature and emission density versus time from dilepton sources from $^{197}\text{Au}+^{197}\text{Au}$ 1.25 GeV/u.

III Modeling of the dense phase in $^{197}\text{Au}+^{197}\text{Au}$ collisions

The e^+e^- pairs from decays of $\Delta(1232)$ and ρ populate at highest densities, and nearly the equal temperatures. The differences between the maximum of the extracted temperatures is less than 10 MeV.

Fig. 3.11 shows the temperature of dilepton sources as a function of the density at the given emission time. Here the results of the χ^2 minimization and those from the refit are shown. In general the success of the method is visible. Only one (Fig. 3.11 (d), last point) of 45 fits is not equal within the uncertainties of the method. In this figure one can see the trajectories of the dilepton sources in the $T_{eff} - \rho/\rho_0$ plane.

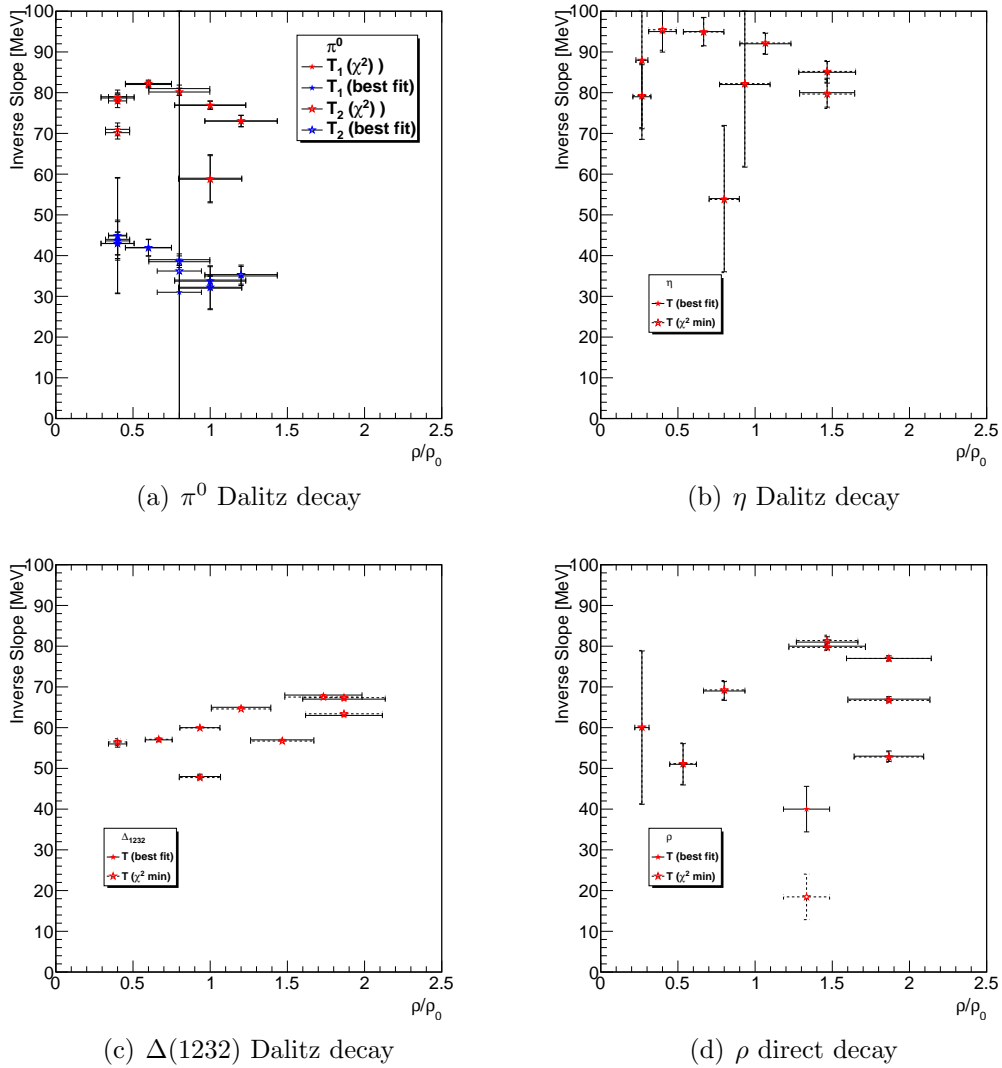


Figure 3.11: Emission temperature of dileptons versus emission density of hadrons from $^{197}\text{Au}+^{197}\text{Au}$ 1.25 GeV/u.

Part IV

Summary and Outlook

*If there is effort,
there is always accomplishment*

Jigoro Kano

Calculations of the dilepton rates in heavy ion reactions require the knowledge of the full space-time history of the colliding and expanding nuclear system. The emission of lepton pairs can either be calculated from thermal fireball expansion models or from microscopic transport calculations. To combine those two models is a final goal of this project. In this work the main goal was the study of lepton pair production simulated with the UrQMD transport model.

First, the heavy ion collisions measured with HADES ($^{12}\text{C}+^{12}\text{C}$ collisions at 1.0 and 2.0 GeV/u and $^{40}\text{Ar}+^{36}\text{Kr}$ at 1.756 GeV/u) were compared to the simulation results. In order to make the comparison with the experimental data, an acceptance filter function provided by the HADES collaboration has been implemented to the simulation chain. Simulated data were treated in the same way as an experimental one, i.e. dilepton events with opening angle smaller than 9 degree have been rejected and the spectra have been normalized to the mean π^0 multiplicity. All measured spectra are dominated by the π^0 Dalitz decay for invariant masses smaller than 0.15 GeV/c^2 and agree very well with the simulated data. However, an overestimation of the data is observed at masses larger than 0.5 GeV/c^2 . The difference is found in the contribution originating from direct ω and ρ meson decays, suggesting a different value of vector meson multiplicity.

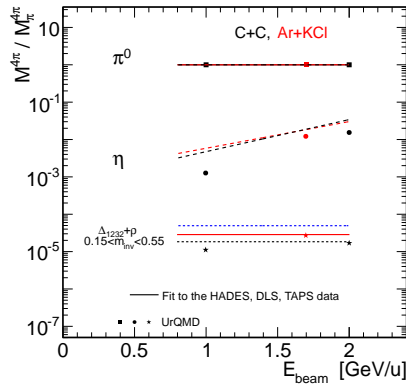


Figure 4.1: Multiplicity of the pair yield above the η Dalitz in the mass range $0.15 < M_{e^+e^-} < 0.55 \text{ GeV}/c^2$ as observed by DLS (open triangles) and HADES (full triangles) as function of beam energy and system size, normalized to the corresponding π^0 multiplicity.

IV Summary and Outlook

The excess pair yield of e^+e^- pairs over the trivial hadronic cocktail was investigated by the HADES and DLS experiments for beam energies from $1.0 \text{ GeV}/u$ up to $2.0 \text{ GeV}/u$. Figure IV shows the, in $^{12}\text{C}+^{12}\text{C}$ and $^{40}\text{Ar}+^{40}\text{KCl}$ collisions measured, integrated e^+e^- pair yield in the invariant mass range $0.15 < M_{e^+e^-} < 0.55 \text{ GeV}/c^2$ depends on the beam energy and the systems size. A systematic study of the e^+e^- pair yield finds a weak scaling with the beam energy and a remarkably similar trend with the increasing beam energy as the mean π^0 multiplicity measured by TAPS. At a given bombarding energy the excess e^+e^- pair yield scales with number of participating nuclei much more strongly than the π^0 production. The non-linear scaling of the excess e^+e^- pair yield with the system size needs more systematic investigation, in particular by studying larger collision systems like $^{197}\text{Au}+^{197}\text{Au}$. Scaling the e^+e^- pair yield with the beam energy (up to $E_{beam} = 8 \text{ GeV}/u$) and system size up to $^{197}\text{Au}+^{197}\text{Au}$ has been extracted as well.

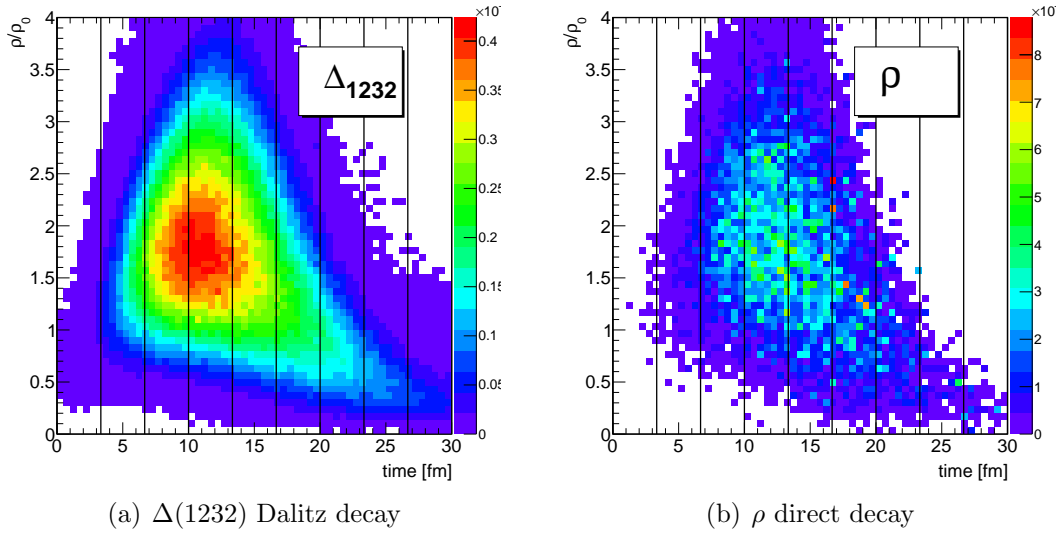
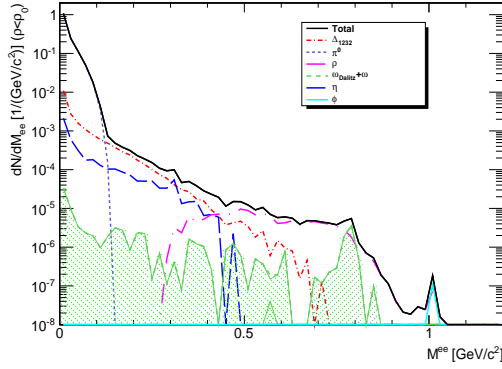
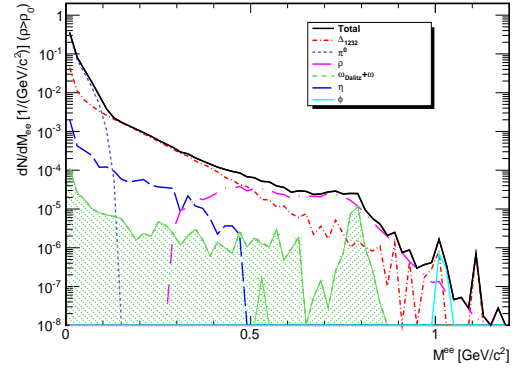


Figure 4.2: Time and density where dileptons from different sources of $^{197}\text{Au}+^{197}\text{Au}$ collisions at $1.25 \text{ GeV}/u$ are produced.

Further I have concentrated on the lepton pair production in $^{197}\text{Au}+^{197}\text{Au}$ collisions at $1.25 \text{ GeV}/u$ that will be measured by HADES in the next year. Figure 4.2 illustrates the density of the systems versus the time of e^+e^- from decays of short-lived ρ meson and a $\Delta(1232)$ baryon. As one can see here the major part of the dileptons come from a density region which is up to 3 times higher than the normal nuclear matter density. This is shown in the Fig. 4.3, where the invariant e^+e^- mass spectra from the $^{197}\text{Au}+^{197}\text{Au}$ collisions at $1.25 \text{ GeV}/u$ are given at two regions of the density, in which the dilepton sources decay. Next I have used the transport model to generate statistical ensembles and extract the temperature and the net-baryon density at a given time of the heavy ion collision.



(a) Invariant e^+e^- mass spectra from emission density of $\rho/\rho_0 < 1$.



(b) Invariant e^+e^- mass spectra from emission density of $\rho/\rho_0 > 1$.

Figure 4.3: Invariant e^+e^- mass spectra from $^{197}\text{Au}+^{197}\text{Au}$ collisions at $1.25 \text{ GeV}/u$ at two regions of the emission density

The inverse-slope parameter of the m_t spectra was extracted using a χ^2 minimization method. This procedure was validated with $^{40}\text{Ar}+^{36}\text{KCl}$ collisions at $1.756 \text{ GeV}/u$ measured by HADES. The extracted temperatures are of the same order as measured slope parameters with the T_{eff} variation on the level of 10 to 15 MeV. The χ^2 minimization method gives sound results and can be used for hadron and dilepton analysis. The main advantage of this algorithm is the secure finding of an absolute minimum, which makes results stable independently of the chosen start values.

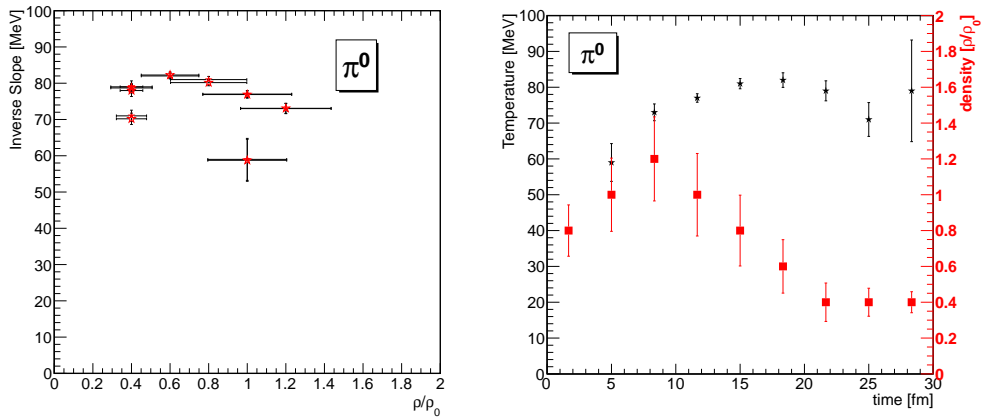


Figure 4.4: Emission temperature and emission density versus time from π^0 Dalitz decay from $^{197}\text{Au}+^{197}\text{Au}$ collisions at $1.25 \text{ GeV}/u$.

The extracted temperatures and densities (see Fig. 4.4) can be used as an input to a thermal model. The combination of UrQMD and a thermal model is expected to give a good approach for describing dilepton radiation from the dense stage of a heavy ion collision at a wide energy range.

Appendix

A Parameters of simulated systems with UrQMD

System	Energy [GeV/u]	b_{max}	Events
$^{12}C+^{12}C$	1	4	400k
$^{12}C+^{12}C$	1 (HACC)	4	400k
$^{12}C+^{12}C$	2	4	400k
$^{12}C+^{12}C$	2 (HACC)	4	400k
$^{40}Ar+KCl$	1.756	7	500k
$^{40}Ar+KCl$	1.756 (HACC)	7	500k
$^{12}C+^{12}C$	1	min bias	100k
$^{12}C+^{12}C$	1.25	min bias	500k
$^{12}C+^{12}C$	2	min bias	100k
$^{40}Ar+KCl$	1.	min bias	100k
$^{40}Ar+KCl$	1.25	min bias	950k
$^{40}Ar+KCl$	2	min bias	100k
$^{107}Ag+^{107}Ag$	1.25	min bias	90k
$^{107}Ag+^{107}Ag$	1.5	min bias	20k
$^{107}Ag+^{107}Ag$	2	min bias	20k
$^{107}Ag+^{107}Ag$	4	min bias	20k
$^{107}Ag+^{107}Ag$	6	min bias	8k
$^{197}Au+^{197}Au$	1.25	min bias	122k
$^{197}Au+^{197}Au$	1.5	min bias	10k
$^{197}Au+^{197}Au$	2	min bias	10k
$^{197}Au+^{197}Au$	4	min bias	18k
$^{197}Au+^{197}Au$	6	min bias	10k

Table A 1: Parameters of simulated systems. HACC means that the simulation passed the related HADES acceptance filter.

Appendix

B Inverse-slope parameters at different rapidity bins

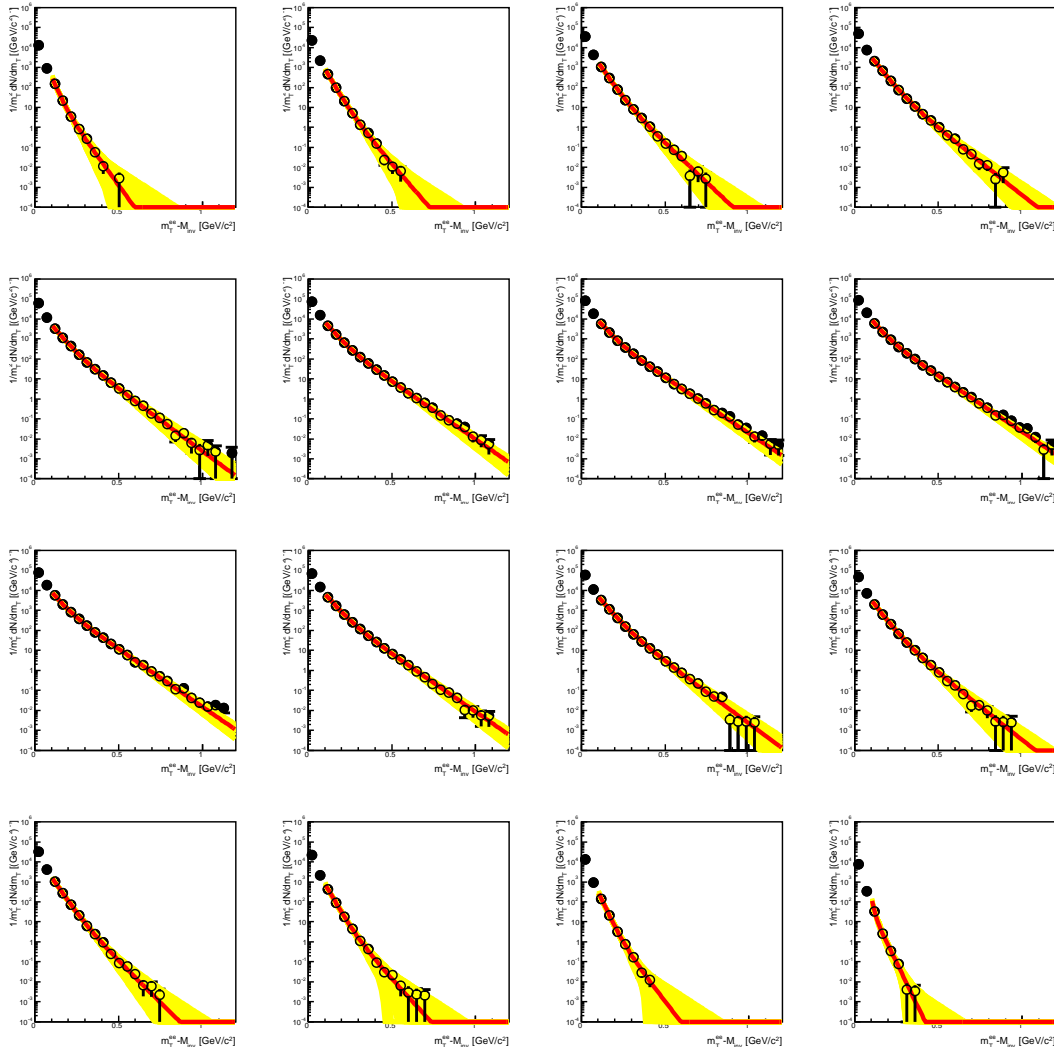


Figure A 5: $m_t - m_{inv}$ distribution for each rapidity bin of the $\pi^0 \rightarrow \gamma e^+ e^-$ decay. The yellow fits have a χ^2 smaller than 10. The red fit is the result of the fit with T_1^* and T_2^* .

B Inverse-slope parameters at different rapidity bins

Y step	Y	T1 [MeV]	T1 error [MeV]	T2 [MeV]	T2 error [MeV]
1	-1.00 - -0.75	21.51	1.55	39.27	3.94
2	-0.75 - -0.50	28.83	1.39	44.88	4.54
3	-0.50 - -0.25	34.46	0.80	56.85	2.91
4	-0.25 - 0.00	39.54	0.63	67.93	2.15
5	0.00 - 0.25	40.99	0.76	71.11	1.44
6	0.25 - 0.50	41.96	0.71	76.93	1.16
7	0.50 - 0.75	40.18	0.78	77.11	0.89
8	0.75 - 1.00	38.46	0.79	76.82	0.78
9	1.00 - 1.25	38.83	0.86	74.83	0.83
10	1.25 - 1.50	40.62	0.71	73.87	1.02
11	1.50 - 1.75	41.05	0.72	70.55	1.48
12	1.75 - 2.00	38.50	0.72	64.25	2.21
13	2.00 - 2.25	34.74	0.76	58.11	4.29
14	2.25 - 2.50	29.23	0.89	52.42	7.00
15	2.50 - 2.75	22.23	2.35	36.21	6.00
16	2.75 - 3.00	9.10	1.39	24.90	1.38

Table A 2: Temperatures and densities of the $\pi^0 \rightarrow \gamma e^+ e^-$ decay for different Y bins in $^{40}\text{Ar} + \text{KCl}$ collisions

Y step	Y	T1 [MeV]	T1 error [MeV]	T2 [MeV]	T2 error [MeV]
1	-1.00 - -0.78	20.61	1.60	42.09	9.57
2	-0.78 - -0.56	25.88	1.05	52.47	8.19
3	-0.56 - -0.34	29.99	1.02	57.17	6.13
4	-0.34 - -0.13	35.96	0.60	75.14	7.03
5	-0.13 - 0.09	37.58	0.87	69.02	3.32
6	0.09 - 0.31	39.73	1.02	72.00	2.72
7	0.31 - 0.53	37.89	1.06	72.47	1.78
8	0.53 - 0.75	38.15	1.15	73.33	1.75
9	0.75 - 0.96	37.44	1.12	72.76	1.61
10	0.96 - 1.19	38.81	1.11	73.73	2.19
11	1.19 - 1.41	39.85	0.97	72.57	2.71
12	1.41 - 1.63	37.34	1.12	66.88	3.81
13	1.63 - 1.84	33.22	1.03	58.26	4.15
14	1.84 - 2.06	28.36	1.53	46.90	3.72
15	2.06 - 2.28	24.29	1.71	44.15	4.71
16	2.28 - 2.50	19.62	2.95	36.56	9.70

Table A 3: Temperatures and densities of the $\pi^0 \rightarrow \gamma e^+ e^-$ decay for different Y bins in $^{197}\text{Au} + ^{197}\text{Au}$ collisions

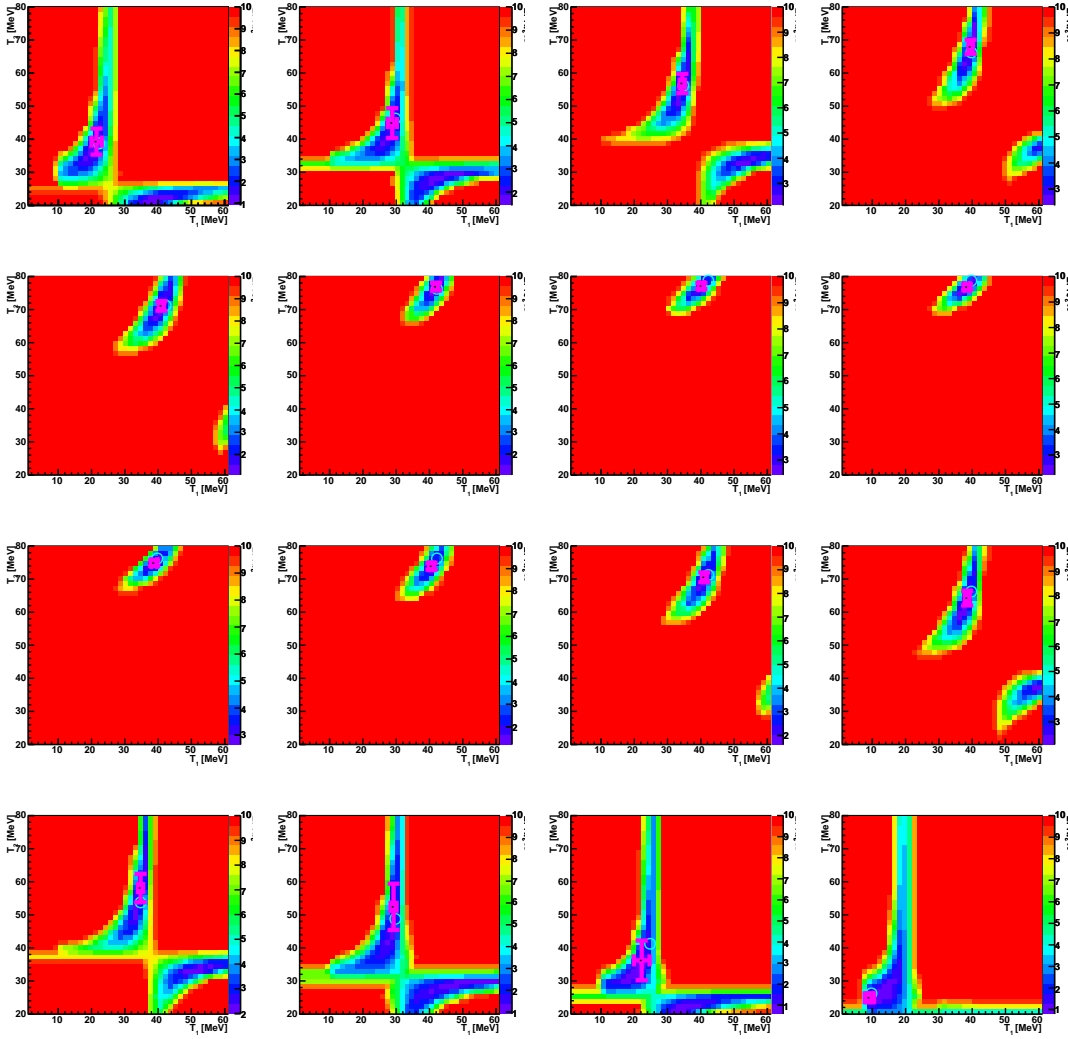


Figure A 6: T_1 versus T_2 versus χ^2 of the $\pi^0 \rightarrow \gamma e^+ e^-$ decay for each rapidity bin. The cyan circle in the minimum area shows the absolute minimum χ^2 . The magenta graph is the result of the fit with T_1^* and T_2^* .

B Inverse-slope parameters at different rapidity bins

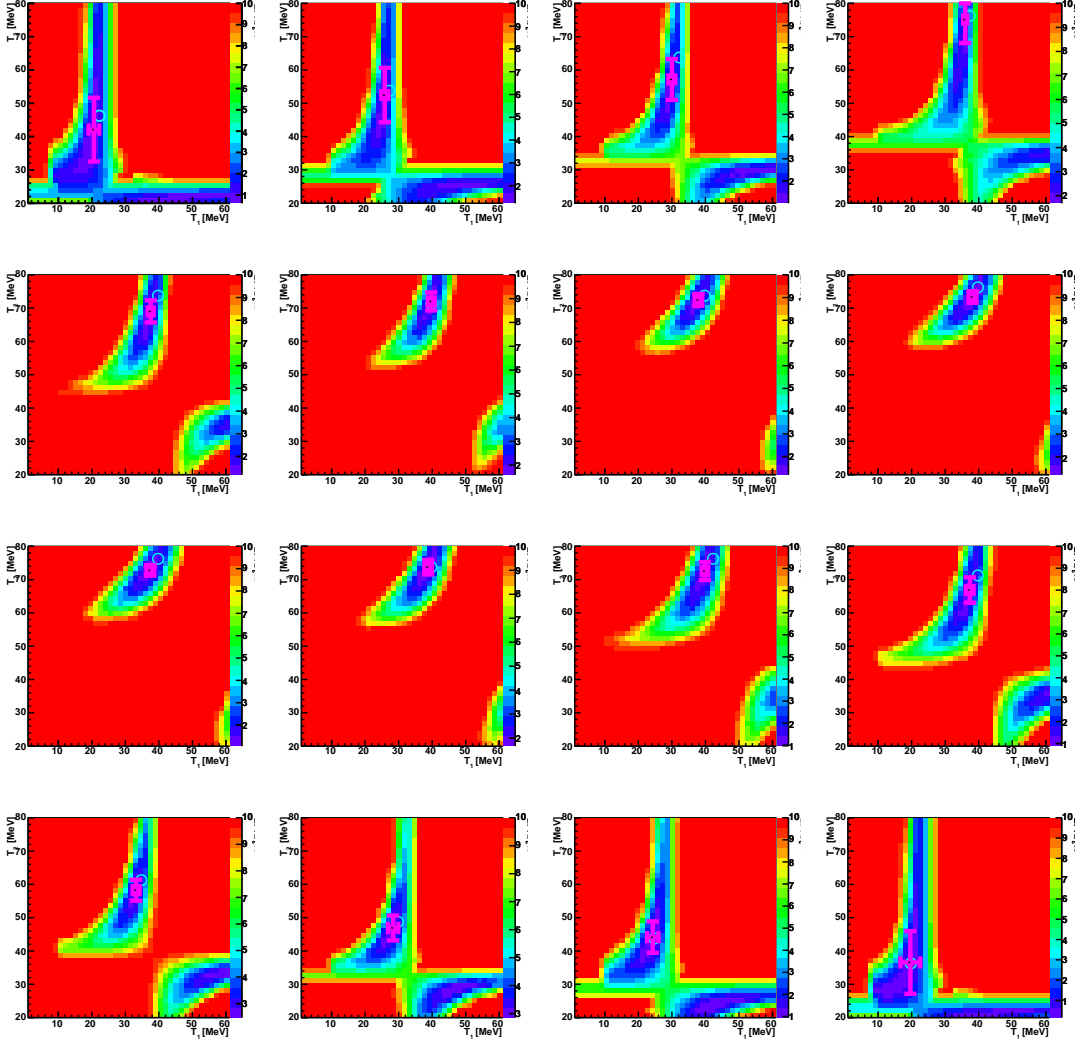


Figure A 7: T_1 versus T_2 versus χ^2 of the $\pi^0 \rightarrow \gamma e^+ e^-$ decay for each rapidity bin. The cyan circle in the minimum area shows the absolute minimum χ^2 . The magenta graph is the result of the fit with T_1^* and T_2^* .

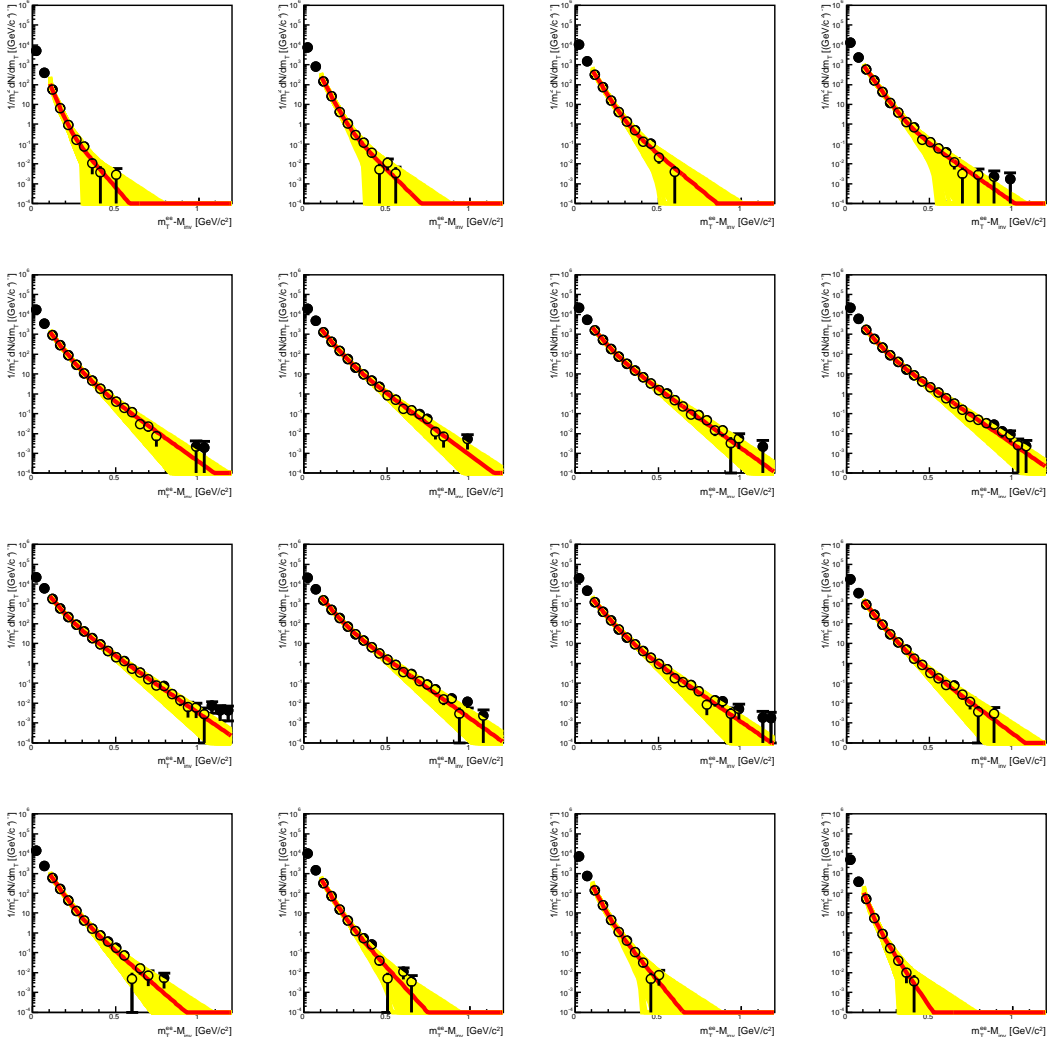


Figure A 8: m_t distribution for each rapidity bin. The yellow fits have a χ^2 smaller than 10. The red fit is the result of the fit with T_1^* and T_2^* .

C Inverse-slope parameters for different time steps bins of the heavy ion collision

Appendix

C Inverse-slope parameters for different time steps bins of the heavy ion collision

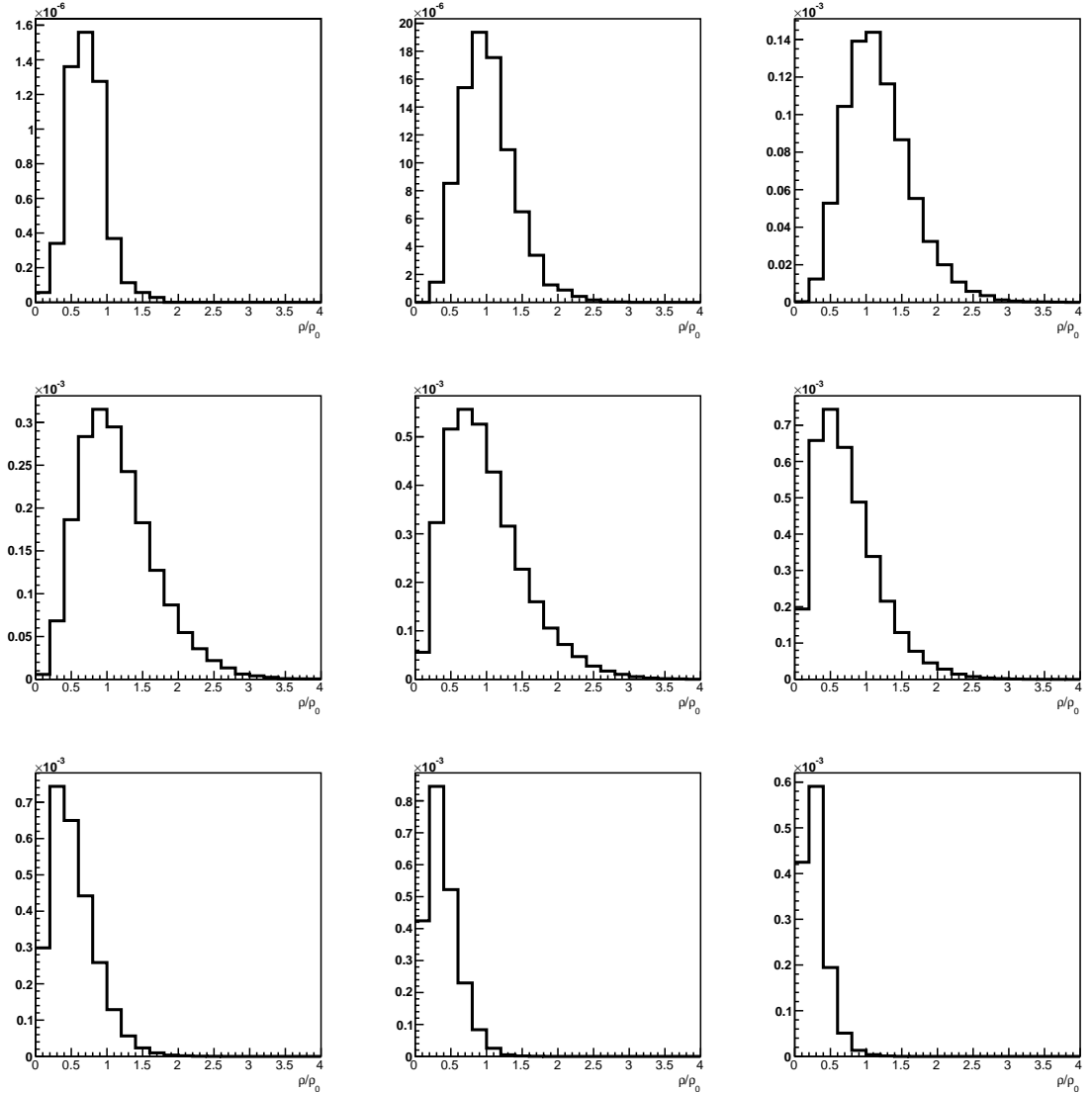


Figure A 9: Density profile of $\pi^0 \rightarrow \gamma e^+ e^-$ decay for time bins of $^{197}\text{Au} + ^{197}\text{Au}$ at $1.25 \text{ GeV}/u$.

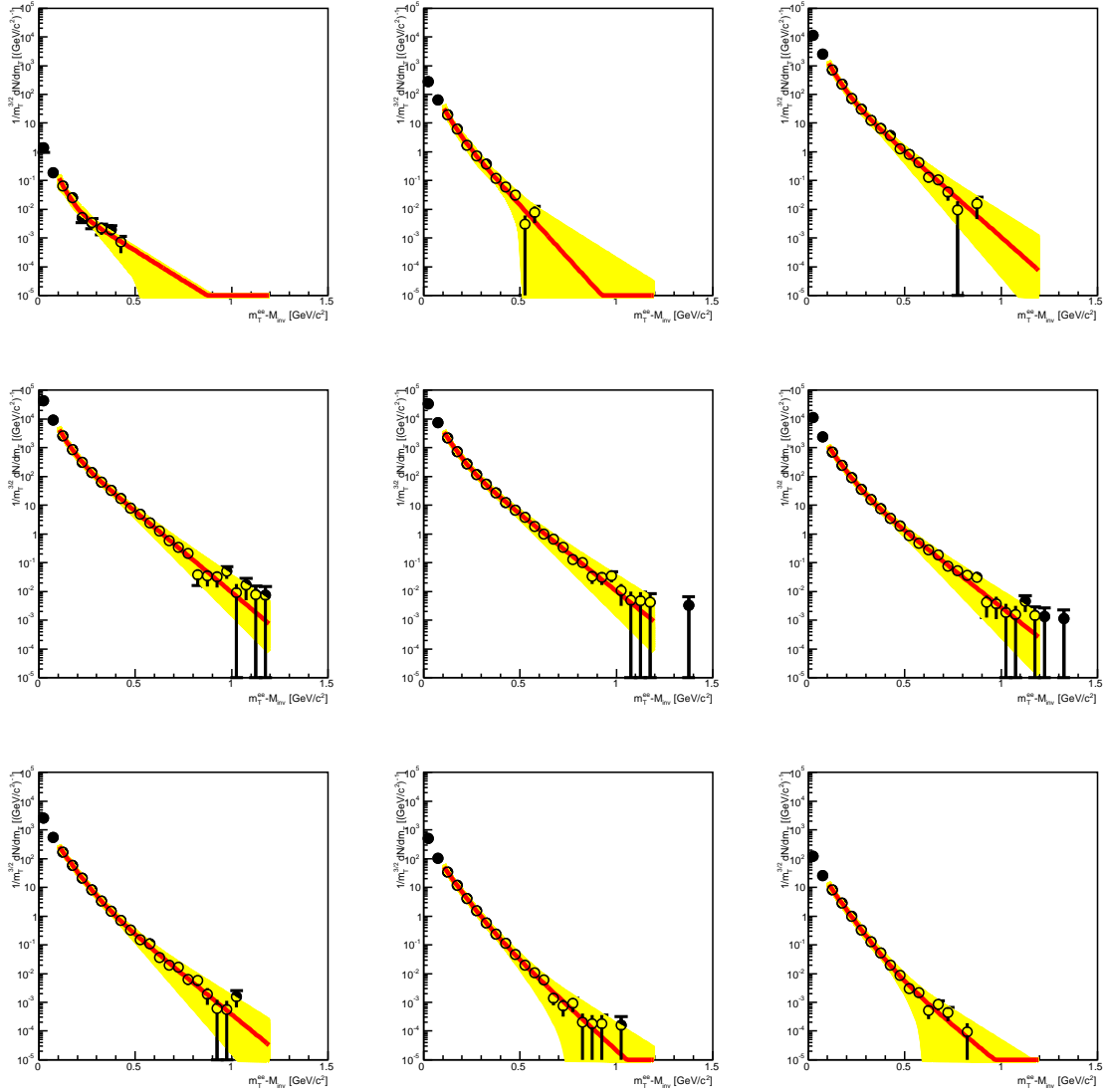


Figure A 10: $m_t - m_{inv}$ spectra of $\pi^0 \rightarrow e^+e^-$ decay with the best fits (yellow, $\chi^2 < 10$) and the fit with T_1^* and T_2^* as start parameter (red) for time bins of $^{197}\text{Au} + ^{197}\text{Au}$ at $1.25 \text{ GeV}/u$.

C Inverse-slope parameters for different time steps bins of the heavy ion collision

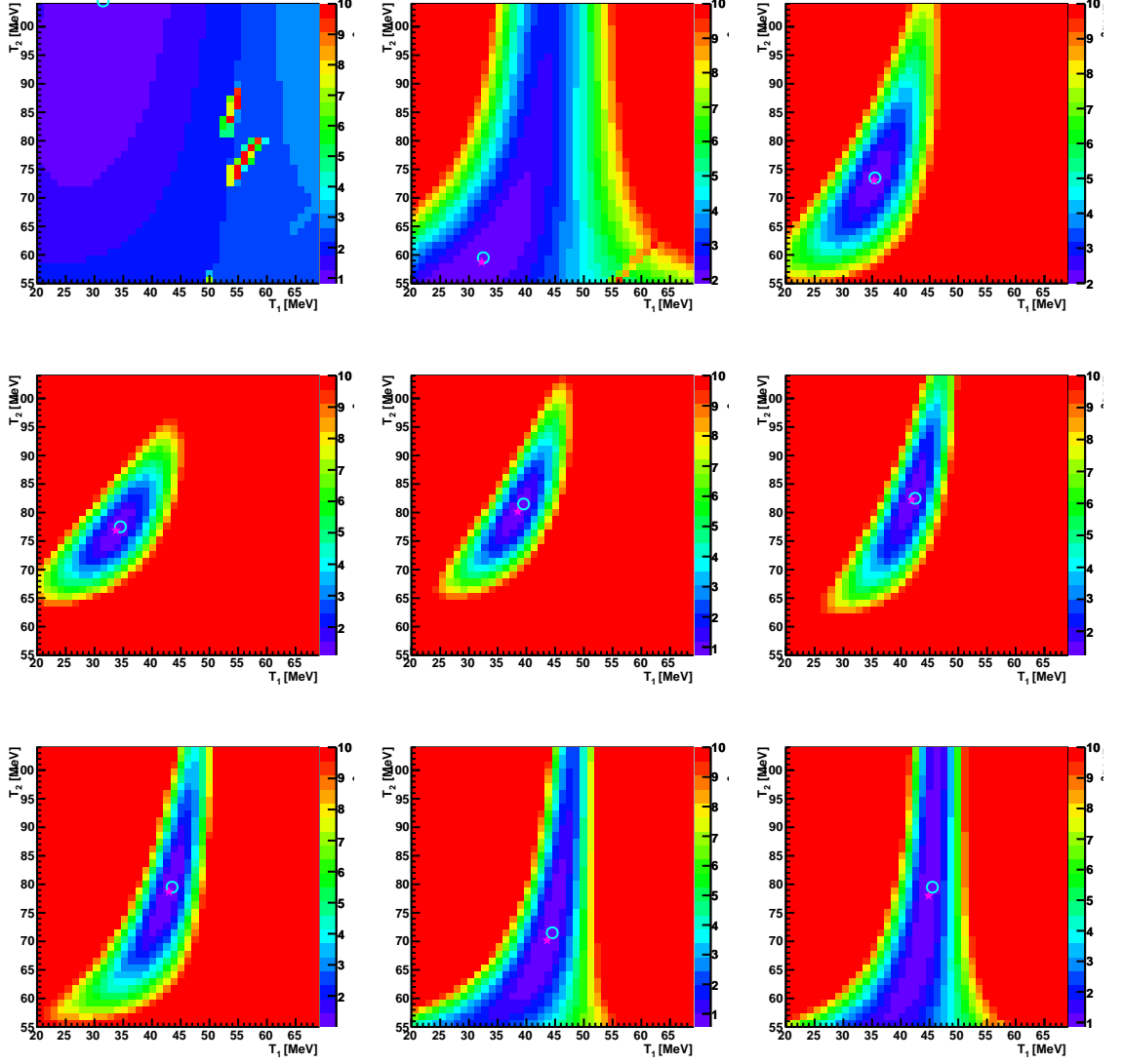


Figure A 11: T_1 versus T_2 versus χ^2 for each time bin of $^{197}\text{Au}+^{197}\text{Au}$ at 1.25 GeV/u . The cyan circle in the minimum area shows the absolute minimum χ^2 . The magenta graph is the result of the fit with T_1^* and T_2^* .

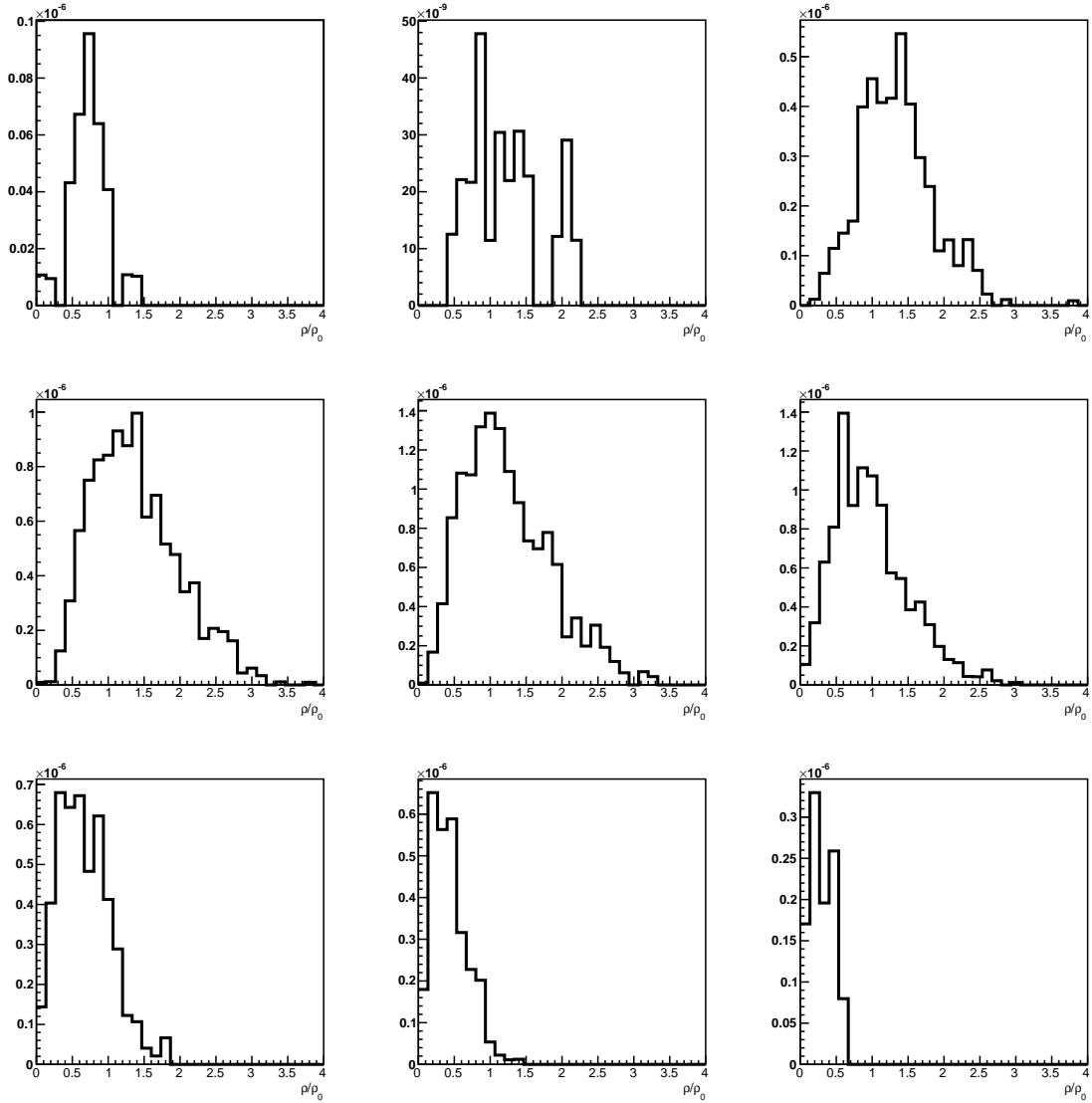


Figure A 12: Density profile of $\eta \rightarrow e^+e^-$ decay for each time bin of $^{197}\text{Au}+^{197}\text{Au}$ at $1.25 \text{ GeV}/u$

C Inverse-slope parameters for different time steps bins of the heavy ion collision

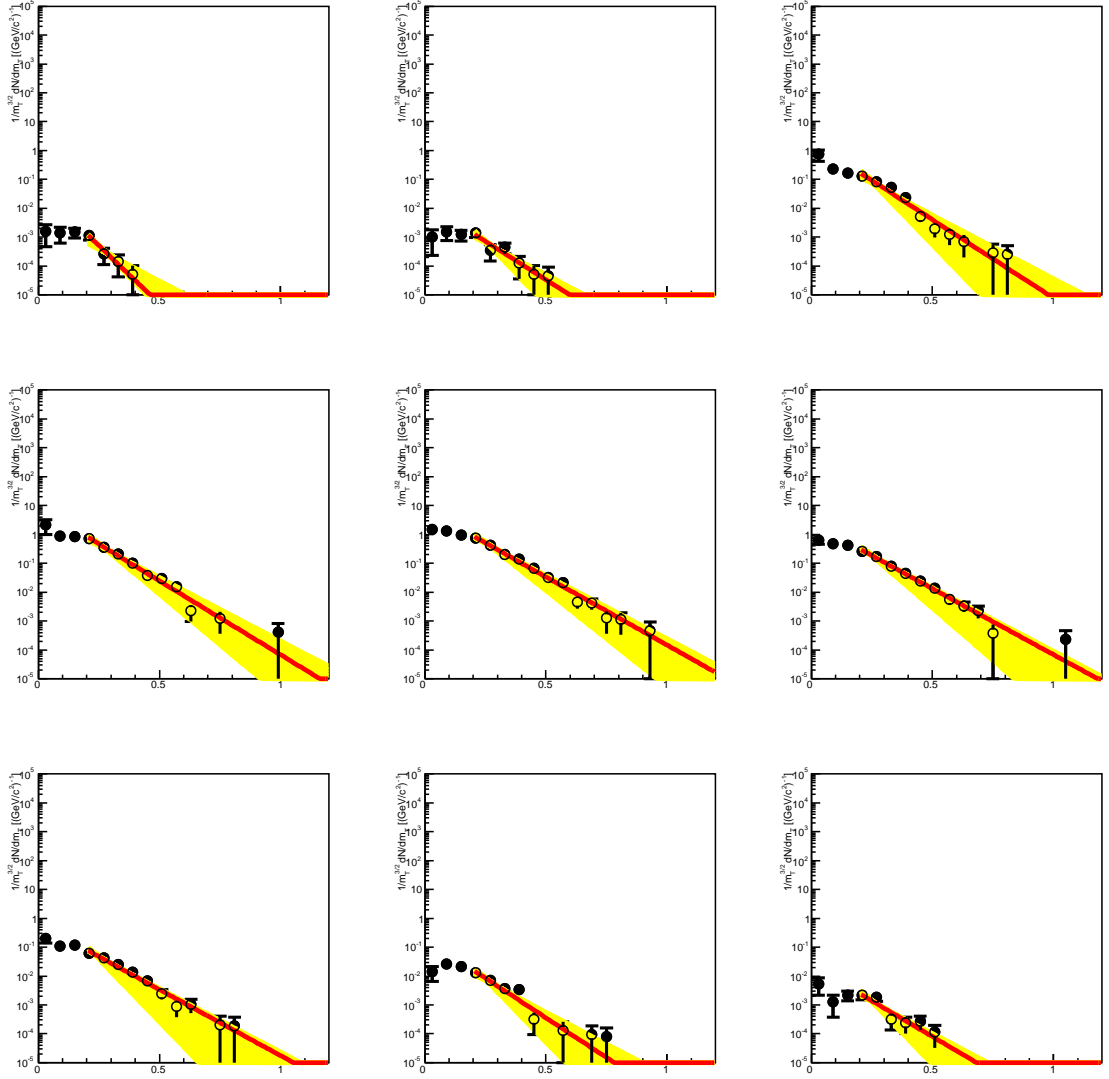


Figure A 13: $m_t - m_{inv}$ spectra of $\eta \rightarrow e^+e^-$ decay with the best fits (yellow, $\chi^2 < 10$) and the fit with T_1^* and as start parameter (red) for each time bin of $^{197}\text{Au}+^{197}\text{Au}$ at $1.25 \text{ GeV}/u$

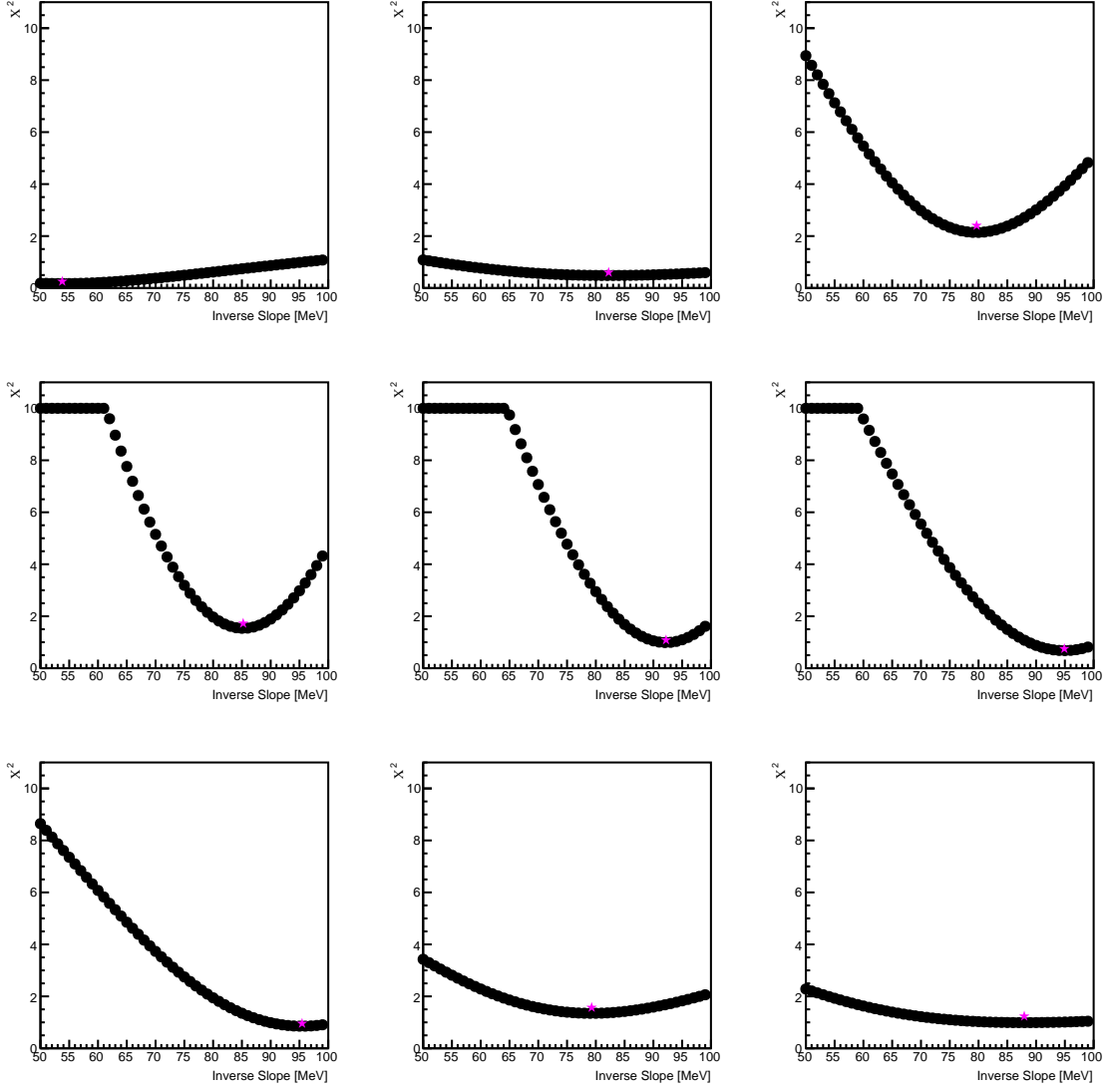


Figure A 14: T versus χ^2 of $\eta \rightarrow e^+e^-$ decay for each time bin of $^{197}\text{Au}+^{197}\text{Au}$ at $1.25 \text{ GeV}/u$. The magenta star is the result of the fit with T_1^* .

C Inverse-slope parameters for different time steps bins of the heavy ion collision

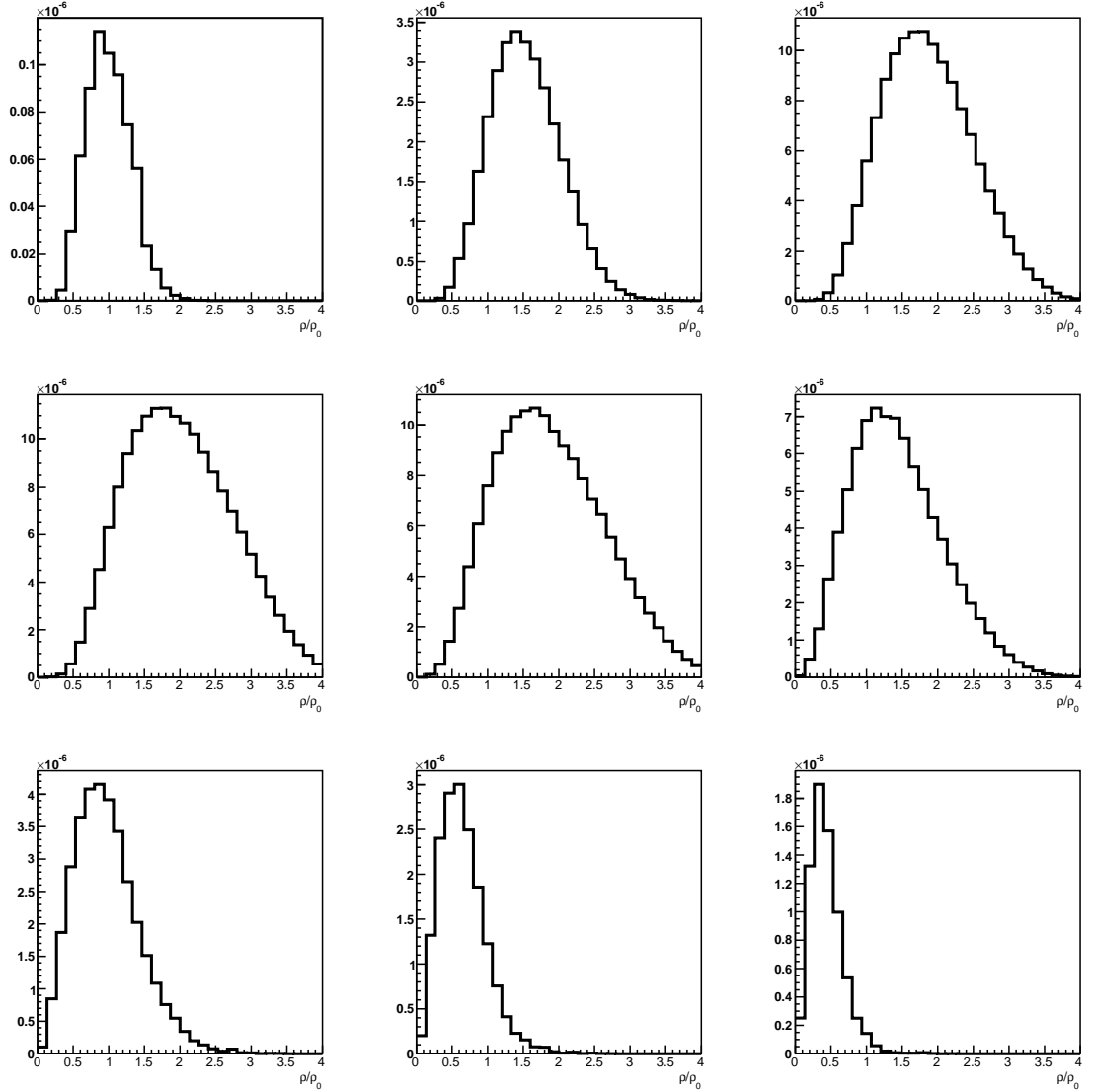


Figure A 15: Density profile of $\Delta_{1232} \rightarrow e^+e^-$ decay for each time bin of $^{197}\text{Au}+^{197}\text{Au}$ at 1.25 GeV/u.

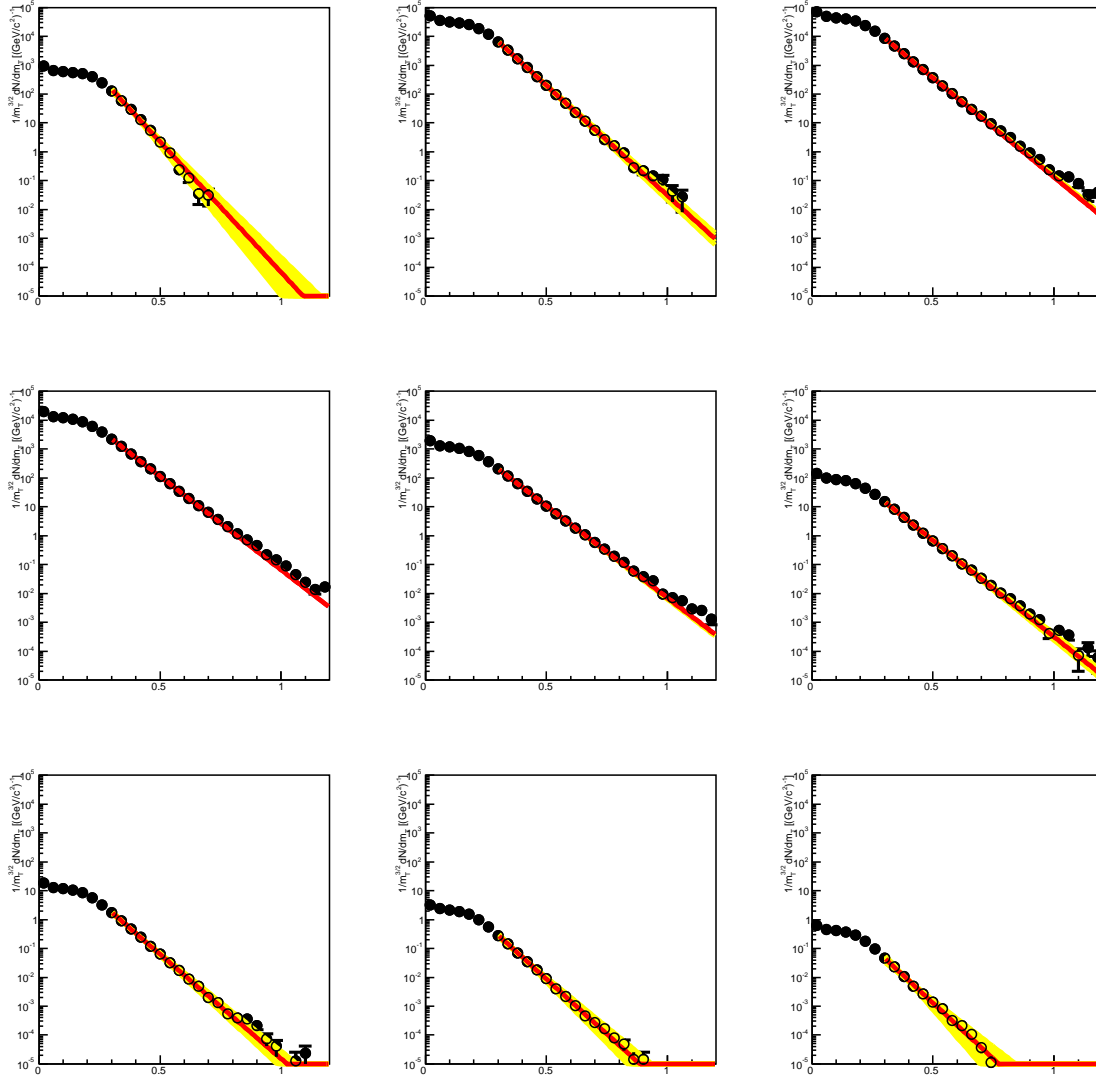


Figure A 16: $m_t - m_{inv}$ spectra of $\Delta_{1232} \rightarrow \gamma e^+ e^-$ decay with the best fits (yellow, $\chi^2 < 10$) and the fit with T_1^* as start parameter (red)

C Inverse-slope parameters for different time steps bins of the heavy ion collision

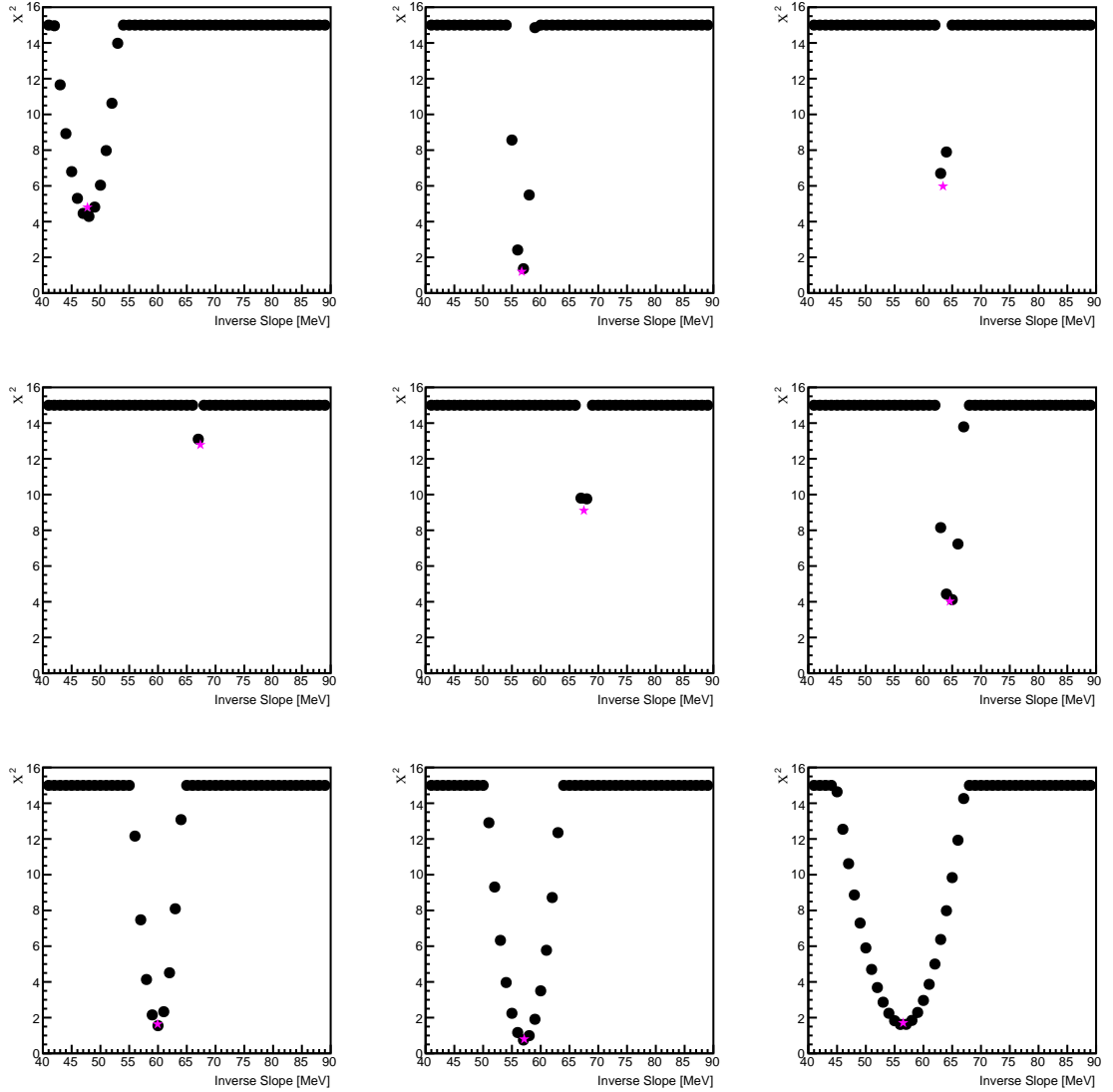


Figure A 17: T_1 versus χ^2 for each time bin of $^{197}\text{Au}+^{197}\text{Au}$ at $1.25\text{ GeV}/u$. The magenta star is the result of the fit with T_1^* .

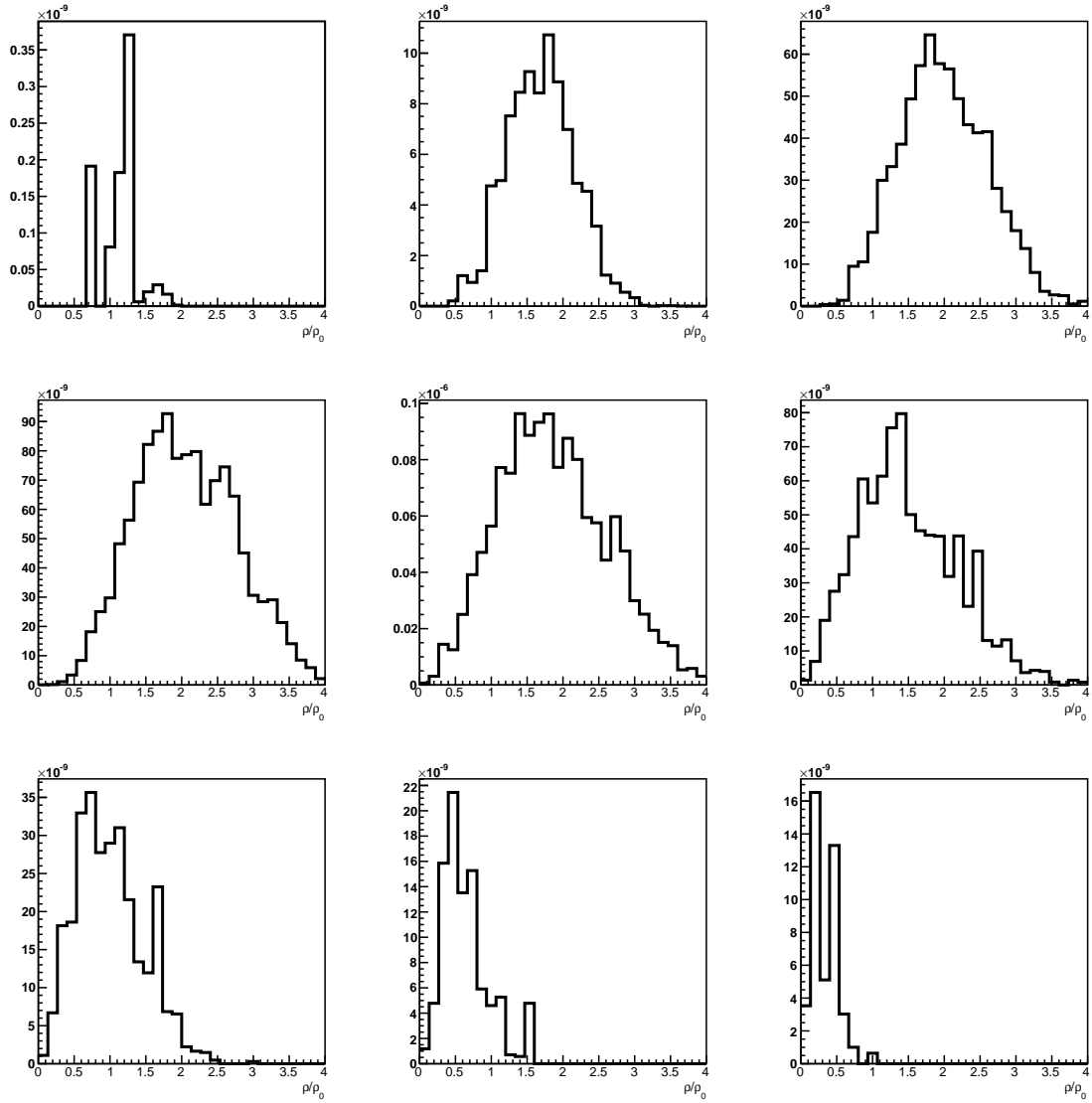


Figure A 18: Density profile of $\rho \rightarrow e^+e^-$ decay of $^{197}\text{Au}+^{197}\text{Au}$ at $1.25\text{ GeV}/u$

C Inverse-slope parameters for different time steps bins of the heavy ion collision

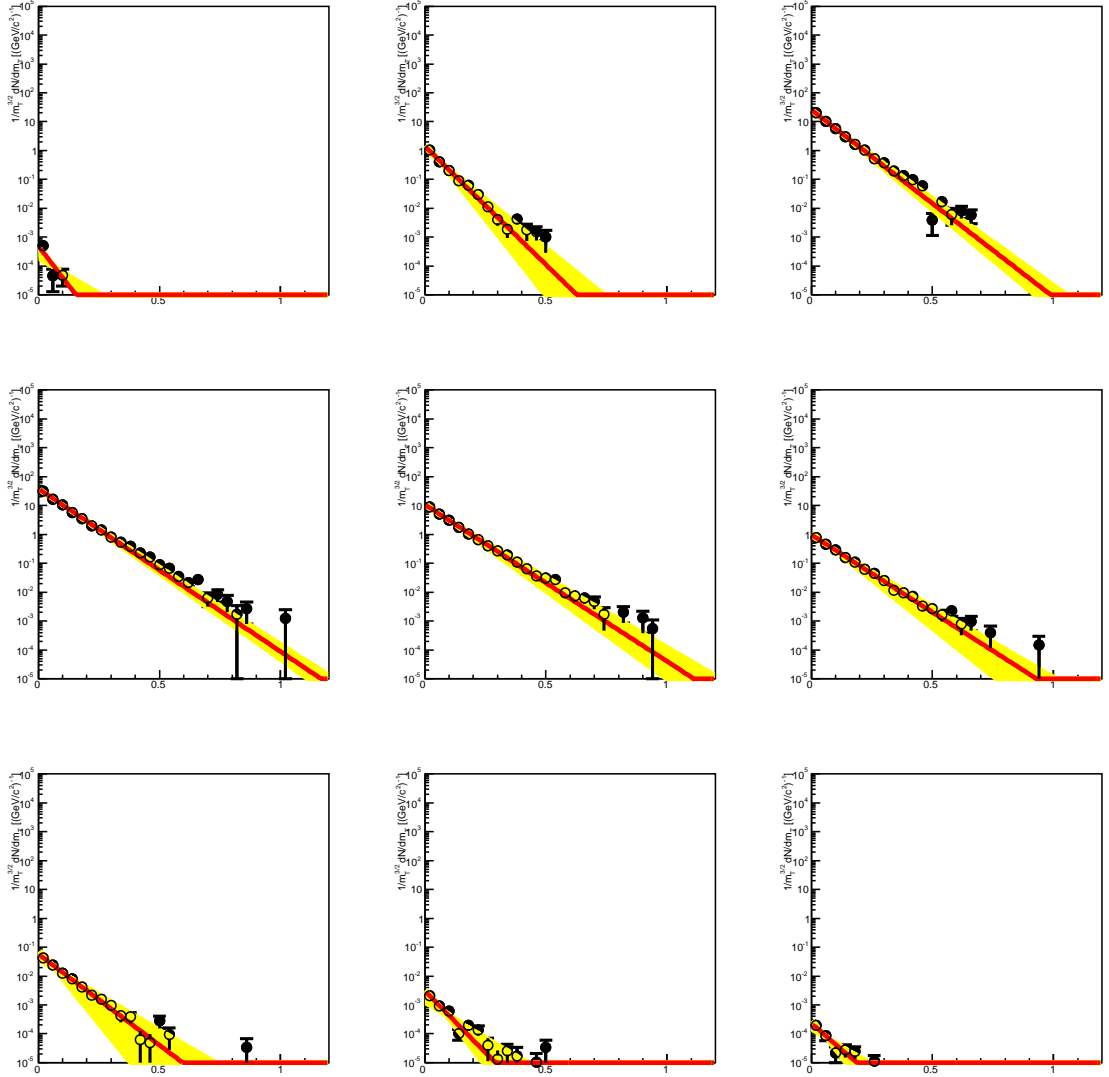


Figure A 19: $m_t - m_{inv}$ spectra of $\rho \rightarrow e^+e^-$ decay with the best fits (yellow, $\chi^2 < 10$) and the fit with T_1^* and as start parameter (red) of $^{197}\text{Au}+^{197}\text{Au}$ at 1.25 GeV/u

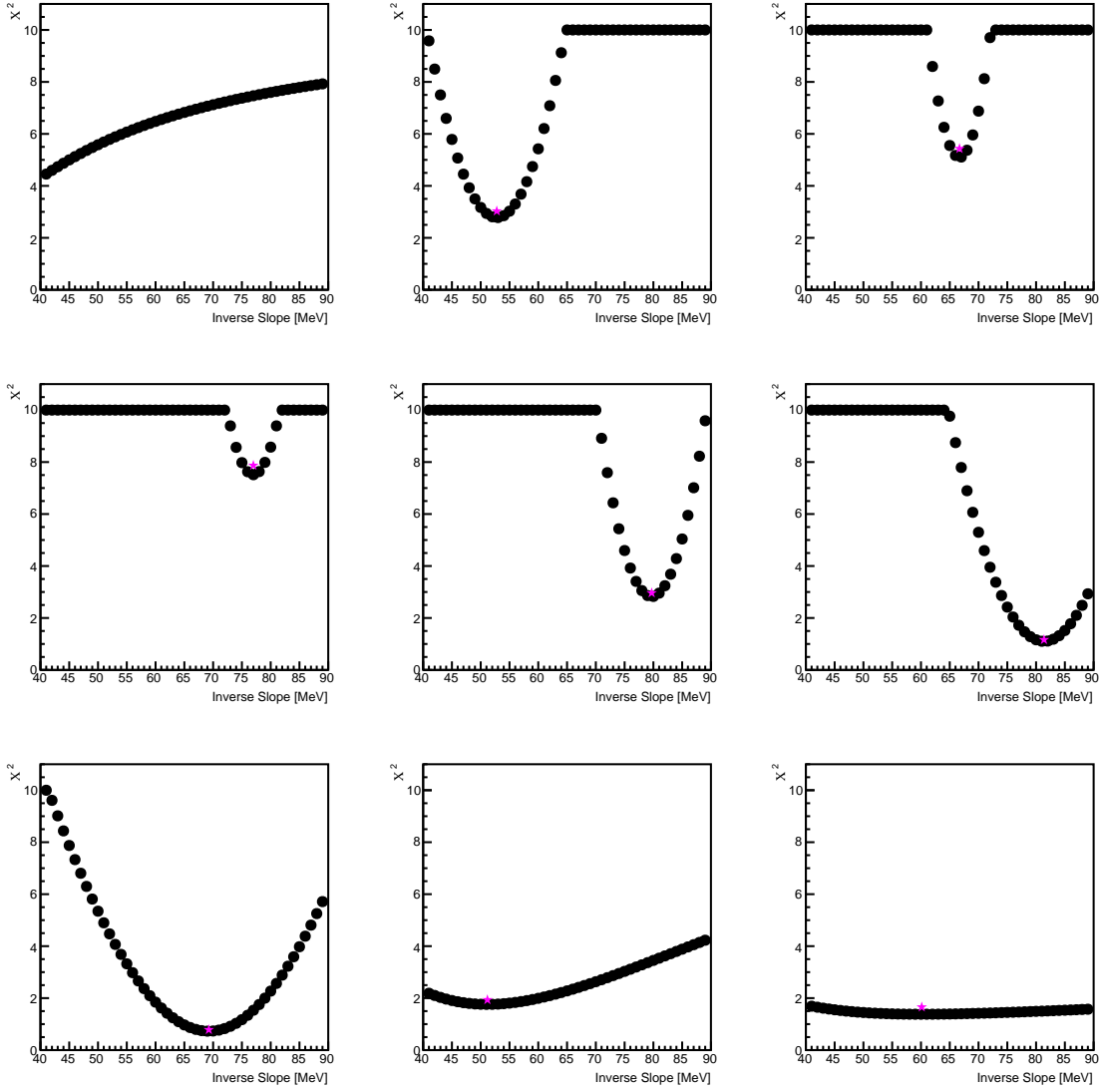


Figure A 20: T_1 versus χ^2 for $\rho \rightarrow e^+e^-$ decay at each time bin of $^{197}\text{Au}+^{197}\text{Au}$ at $1.25 \text{ GeV}/u$. The cyan circle in the minimum area shows the absolute minimum χ^2 . The magenta star is the result of the fit with T_1^* .

C Inverse-slope parameters for different time steps bins of the heavy ion collision

Time step	time [fm]	density [ρ/ρ_0]	mean of density [ρ/ρ_0]	temperature [MeV]	temperature error [MeV]
1	0-3.33	0.80	0.10	36.21 165.78	9.30 151.75
2	3.33-6.66	0.93	0.14	32.23 58.75	5.79 5.28
3	6.66-10.00	1.07	0.16	35.34 73.08	1.39 2.34
4	10.00-13.33	1.07	0.15	33.73 76.87	0.99 1.19
5	13.33-16.66	0.67	0.13	38.50 80.17	0.87 1.43
6	16.66-20.00	0.53	0.10	41.90 82.26	0.83 2.04
7	20.00-23.33	0.40	0.07	42.95 78.70	0.95 2.79
8	23.33-26.66	0.27	0.05	43.61 70.19	1.56 4.72
9	26.66-30.00	0.27	0.04	44.83 77.98	1.64 14.18

Table A 4: Temperatures and densities of dileptons from π^0 Dalitz decay for different time bins in $^{197}\text{Au}+^{197}\text{Au}$ collisions at $1.25\text{ GeV}/u$

Time step	time [fm]	density [ρ/ρ_0]	mean of density [ρ/ρ_0]	temperature [MeV]	temperature error [MeV]
1	0-3.33	0.80	0.10	53.78	17.96
2	3.33-6.66	0.93	0.16	82.23	20.28
3	6.66-10.00	1.47	0.17	79.66	3.55
4	10.00-13.33	1.47	0.18	85.22	2.65
5	13.33-16.66	1.07	0.17	92.20	2.59
6	16.66-20.00	0.67	0.13	94.90	3.48
7	20.00-23.33	0.40	0.09	95.45	5.03
8	23.33-26.66	0.27	0.06	79.27	7.86
9	26.66-30.00	0.27	0.39	87.94	19.44

Table A 5: Temperatures and densities of dileptons from $\eta \rightarrow e^+e^-$ for different time bins in $^{197}\text{Au}+^{197}\text{Au}$ collisions at $1.25\text{ GeV}/u$

Time step	time [fm]	density [ρ/ρ_0]	mean of density [ρ/ρ_0]	temperature [MeV]	temperature error [MeV]
1	0-3.33	0.93	0.13	47.75	0.57
2	3.33-6.66	1.47	0.20	56.70	0.15
3	6.66-10.00	1.87	0.25	63.40	0.09
4	10.00-13.33	1.87	0.27	67.36	0.08
5	13.33-16.66	1.73	0.25	67.50	0.10
6	16.66-20.00	1.20	0.19	64.59	0.17
7	20.00-23.33	0.93	0.13	59.94	0.28
8	23.33-26.66	0.67	0.09	57.13	0.46
9	26.66-30.00	0.40	0.05	56.48	0.79

Table A 6: Temperatures and densities of dileptons from $\Delta(1232)$ Dalitz decay for different time bins in $^{197}\text{Au}+^{197}\text{Au}$ collisions at $1.25 \text{ GeV}/u$

Time step	time [fm]	density [ρ/ρ_0]	mean of density [ρ/ρ_0]	temperature [MeV]	temperature error [MeV]
1	0-3.33	1.33	0.15	18.45	5.58
2	3.33-6.66	1.87	0.22	52.79	1.28
3	6.66-10.00	1.87	0.26	66.69	0.62
4	10.00-13.33	1.87	0.27	76.99	0.62
5	13.33-16.66	1.47	0.25	79.70	0.77
6	16.66-20.00	1.47	0.19	81.38	1.31
7	20.00-23.33	0.80	0.13	69.26	2.31
8	23.33-26.66	0.53	0.09	51.16	5.07
9	26.66-30.00	0.26	0.05	60.13	18.82

Table A 7: Temperatures and densities of dileptons from ρ decay for different time bins in $^{197}\text{Au}+^{197}\text{Au}$ collisions at $1.25 \text{ GeV}/u$

Bibliography

- [A⁺09] G. Agakishiev et al. The High-Acceptance Dielectron Spectrometer HADES. *Eur. Phys. J.*, A41:243–277, 2009.
- [A⁺10] G. Agakishiev et al. Origin of the low-mass electron pair excess in light nucleus-nucleus collisions. *Phys. Lett.*, B690:118–122, 2010.
- [A⁺11] G. Agakishiev et al. Dielectron production in Ar+KCl collisions at 1.76A GeV. 2011.
- [ABBM⁺10] A. Andronic, D. Blaschke, P. Braun-Munzinger, J. Cleymans, K. Fukushima, L.D. McLerran, H. Oeschler, R.D. Pisarski, K. Redlich, C. Sasaki, H. Satz, and J. Stachel. Hadron production in ultra-relativistic nuclear collisions: Quarkyonic matter and a triple point in the phase diagram of qcd. *Nuclear Physics A*, 837(1-2):65 – 86, 2010.
- [AHMS03] R. Auerbach, R. Holzmann, V. Metag, and R. S. Simon. Neutral pions and η mesons as probes of the hadronic fireball in nucleus-nucleus collisions around 1a gev. *Phys. Rev. C*, 67:024903, Feb 2003.
- [ASRS08] Mark G. Alford, Andreas Schmitt, Krishna Rajagopal, and Thomas Schafer. Color superconductivity in dense quark matter. *Rev. Mod. Phys.*, 80:1455–1515, 2008.
- [BBC76] A. Biallas, M. Bleszynski, and W. CzyÅ¼. Multiplicity distributions in nucleus-nucleus collisions at high energies. *Nuclear Physics B*, 111(3):461 – 476, 1976.
- [BK99] E. L. Bratkovskaya and C. M. Ko. Low-mass dileptons and dropping rho meson mass. *Phys. Lett.*, B445:265–270, 1999.
- [CKV82] A. Capella, J. Kwiecinski, and J. Tran Thanh Van. High-energy nucleus-nucleus inelastic interactions in the dual parton model. *Physics Letters B*, 108(4-5):347 – 350, 1982.
- [CMS]
- [D⁺07] S. Damjanovic et al. NA60 results on the rho spectral function in In-In collisions. *Nucl.Phys.*, A783:327–334, 2007.
- [FK04] Z. Fodor and S. D. Katz. Critical point of QCD at finite T and mu, lattice results for physical quark masses. *JHEP*, 04:050, 2004.
- [FP97] Bengt Friman and H. J. Pirner. P-wave polarization of the ρ -meson and the dilepton spectrum in dense matter. *NUCL.PHYS.A*, 617:496, 1997.

- [Gal09] T Galatyuk. *Di-electron spectroscopy in HADES and CBM: from $p + p$ and $n + p$ collisions at GSI to $Au + Au$ collisions at FAIR*. PhD thesis, Goethe-Universitaet, Frankfurt am Main, 2009.
- [HAA⁺97a] R. Holzmann, M. Appenheimer, R. Averbeck, Y. Charbonnier, H. Delagrange, J. Diaz, A. Doppenschmidt, V. Hejny, S. Hlavaifm-mode, A. Kugler, F. Lefevre, H. Lohner, A. Marin, G. Martinez, T. Matulewicz, V. Metag, R. Novotny, R. W. Ostendorf, R. Pleskac, Y. Schutz, R. H. Siemssen, R. S. Simon, H. Stroher, P. Tlusty, P. H. Vogt, V. Wagner, J. Weiss, H. W. Wilschut, F. Wissmann, A. R. Wolf, and M Wolf. Production of p and light mesons in carbon-induced relativistic heavy-ion collisions. *Zeitschrift für Physik A Hadrons and Nuclei*, 359:65–73, 1997. 10.1007/s002180050368.
- [HAA⁺97b] R. Holzmann, M. Appenheimer, R. Averbeck, Y. Charbonnier, H. Delagrange, J. Diaz, A. Doppenschmidt, V. Hejny, S. Hlavaifm-mode, A. Kugler, F. Lefevre, H. Lohner, A. Marin, G. Martinez, T. Matulewicz, V. Metag, R. Novotny, R. W. Ostendorf, R. Pleskac, Y. Schutz, R. H. Siemssen, R. S. Simon, H. Stroher, P. Tlusty, P. H. Vogt, V. Wagner, J. Weiss, H. W. Wilschut, F. Wissmann, A. R. Wolf, and M. Wolf. Contribution of π and η dalitz decays to the dilepton invariant-mass spectrum in 1a gev heavy-ion collisions. *Phys. Rev. C*, 56:R2920–R2923, Dec 1997.
- [Hag84] R. Hagedorn. MULTIPLICITIES, P(T) DISTRIBUTIONS AND THE EXPECTED HADRON \rightarrow QUARK - GLUON PHASE TRANSITION. *Riv. Nuovo Cim.*, 6N10:1–50, 1984.
- [HL92] Ulrich Heinz and Kang Seog Lee. Dileptons from $[\varrho]$ -mesons as a fast clock for heavy-ion collisions. *Nuclear Physics A*, 544(1-2):503 – 507, 1992.
- [hlm] <http://www-linux.gsi.de/misko/overlap/>.
- [K⁺04] F. Karsch et al. Where is the chiral critical point in 3-flavor QCD? *Nucl. Phys. Proc. Suppl.*, 129:614–616, 2004.
- [LKH⁺97] I. Levine, D. Koltick, B. Howell, E. Shibata, J. Fujimoto, T. Tauchi, K. Abe, T. Abe, I. Adachi, K. Adachi, M. Aoki, M. Aoki, K. Emi, R. Enomoto, H. Fujii, K. Fujii, T. Fujii, N. Fujiwara, H. Hayashii, H. Hirano, H. Ikeda, H. Ikeda, Y. Inoue, S. Itami, R. Itoh, H. Iwasaki, M. Iwasaki, R. Kajikawa, K. Kaneyuki, S. Kato, S. Kawabata, H. Kichimi, M. Kobayashi, H. Mamada, K. Miyabayashi, A. Miyamoto, K. Nagai, K. Nakabayashi, M. Nakamura, E. Nakano, O. Nitoh, S. Noguchi, A. Ochi, F. Ochiai, N. Ohishi, Y. Ohnishi, Y. Ohshima, H. Okuno, T. Okusawa,

- A. Sugiyama, S. Suzuki, K. Takahashi, T. Takahashi, T. Tanimori, Y. Teramoto, M. Tomoto, T. Tsukamoto, T. Tsumura, S. Uno, K. Watanabe, Y. Watanabe, A. Yamamoto, and M. Yamauchi. Measurement of the electromagnetic coupling at large momentum transfer. *Phys. Rev. Lett.*, 78(3):424–427, Jan 1997.
- [MP07] Larry McLerran and Robert D. Pisarski. Phases of Cold, Dense Quarks at Large N_c . *Nucl. Phys.*, A796:83–100, 2007.
- [N⁺10] K Nakamura et al. Review of particle physics. *J. Phys.*, G37:075021, 2010.
- [P⁺08] Y. C. Pachmayer et al. Dielectron Production in C+C Collisions at 1 GeV/u and the Solution to the DLS Puzzle. *J. Phys.*, G35:104159, 2008.
- [R⁺88] G. Roche et al. FIRST OBSERVATION OF DIELECTRON PRODUCTION AT THE BEVALAC. *Phys. Rev. Lett.*, 61:1069–1072, 1988.
- [RR06] Thorsten Renk and Jorg Ruppert. From In In to Pb Pb collisions: Lessons from high- precision dilepton measurements. 2006.
- [RWvH09] R. Rapp, J. Wambach, and H. van Hees. The Chiral Restoration Transition of QCD and Low Mass Dileptons. 2009.
- [S⁺09] M. Sudol et al. Measurement of low-mass $e^+ e^-$ pair production in 1-A-GeV and 2-A-GeV C-C collision with HADES. *Eur. Phys. J.*, C62:81–84, 2009.
- [Sak60] J. J. Sakurai. Theory of strong interactions. *Annals Phys.*, 11:1–48, 1960.
- [Sny05] J.A. Snyman. *Practical mathematical optimization: an introduction to basic optimization theory and classical and new gradient-based algorithms*. Applied optimization. Springer, 2005.
- [Sta96] J. Stachel. Tests of thermalization in relativistic nucleus nucleus collisions. *Nucl. Phys.*, A610:509c–522c, 1996.
- [WBB⁺98] W. K. Wilson, S. Beedoe, R. Bossingham, M. Bougheb, J. Carroll, W. G. Gong, T. Hallman, L. Heilbronn, H. Z. Huang, G. Igo, P. Kirk, G. Krebs, A. Letessier-Selvon, L. Madansky, F. Manso, D. Magestro, H. S. Matis, J. Miller, C. Naudet, R. J. Porter, M. Prunet, G. Roche, L. S. Schroeder, P. Seidl, M. Toy, Z. F. Wang, R. C. Welsh, and A. Yegneswaran. Inclusive dielectron cross sections in $p + p$ and $p + d$ interactions at beam energies from 1.04 to 4.88 gev. *Phys. Rev. C*, 57(4):1865–1878, Apr 1998.

- [WGJ⁺76] G. D. Westfall, J. Gosset, P. J. Johansen, A. M. Poskanzer, W. G. Meyer, H. H. Gutbrod, A. Sandoval, and R. Stock. Nuclear fireball model for proton inclusive spectra from relativistic heavy-ion collisions. *Phys. Rev. Lett.*, 37(18):1202–1205, Nov 1976.

Acknowledgments

First I like to thank my supervisor Prof. Dr. Joachim Stroth, who gave me the chance to make this thesis in the "HADES group" at Goethe University and supported me during my studies.

A special thank goes to Dr. Christian Müntz for critic and encouragement, for all stories from "old times" he used to tell and for a strong supporting for us students.

Dr. Jochen Markert: `SetMarkertStyle->("Thank you")`; especially for the coffee time, your patience when you try to explain programming to me and of course for reading parts of this work.

I like to thank all the people of the HADES collaboration, especially those from the Frankfurt HADES/CBM and the GSI group, notably, Manuel Lorenz, Jan Michel, Dr. Ingo Fröhlich and Dr. Christian Strum.

Furthermore I like to thank the people from the UrQMD collaboration, here especially Prof. Dr. Marcus Bleicher and Dr. Elvira Santini, that they make this work possible.

I like to thank my friends Timo, Sarah, Fritz, Achim, Christian, Heidi and very much Laura for learning, understanding and celebrating together. Without you the last five years would be totally boring!

A very special thank goes to those, which share the other passion of my life with me, Mandy, Carina, Manuela and Roland.

Спасибо Тетяна, ты мой руководитель, мой пример и мой друг.

Thank you for teaching me the passion of physics and motivating me if I struggle. I will never forget your huge help with this thesis.

Danke Mama, danke Papa, alles was ich bin, bin ich dank euch.